Functionalization of Porous Carbon Materials with Heteroatoms and Application as Supports in Industrial Heterogeneous Catalysis

M. Sc. Sandy M. G. Lama

geboren am 04.05.1989 in Bethlehem, Palästina

University Dissertation

zur Erlangung des akademischen Grades
„doctor rerum naturalium"
(Dr. rer. nat.)
in der Wissenschaftsdisziplin „Kolloidchemie"

eingereicht an der
Mathematisch-Naturwissenschaftlichen Fakultät
Institut für Chemie
der Universität Potsdam
und
Kolloidchemie Abteilung
der Max-Planck-Institut für Kolloid-und Grenzflächenforschung

Potsdam-Golm, im April 2018

CARBON CATALYSIS

Science

"If the result confirms the hypotheses, you've made a discovery. If the result is contrary to the hypotheses, you've made a discovery."

(Enrico Fermi)

Dedication

I dedicate this work to God for keeping me under his protection and strengthening me to keep on achieving.

Also, I dedicate this work to my beloved parents who have always loved me unconditionally and whose good examples have taught me to work hard for the things that I aspire to reach.

Finally, I dedicate this work to my soul that has gone through much on its own but still faced everything and seeked to continue overcoming challenges and accomplishing in science.

"A little science estranges man from God, but much science leads them back to him."
(Lewis Pasteur)

Acknowledgment

"The scientist only imposes two things, namely truth and sincerity, imposes them upon himself and upon other scientists."

(Erwin Schrödinger)

Table of contents

Chapter 1

Motivation

"Be less curious about people and more about ideas."
(Marie Curie)

1. Motivation

Chemicals represent an essential part in our daily life. They are applied in almost every product whether in food such as preservative, in IT products as smart phones and computers, in transportation as fuel source, and many more. The increase in global population means a high demand for energy and chemicals. Fossil fuels- the main feedstock for energy and chemicals- is an unstable resource and contributes to different matters (i.e. environmental, economical, and political); Hence, the search for alternative renewable and environmentally friendly chemical feedstocks. As these alternatives need different processing than petroleum fuels, industry is urged to improve established heterogeneous catalytic systems. Most of the industrial productions depend on heterogeneously catalyzed chemical conversions. The catalyst activity, selectivity, stability, cost of preparation and recyclation, and the conditions required for activation of the catalyst influence the production rate, quantity and quality, and cost of the final product. The more selective, stable, active and easier to recycle the catalyst, the better the production rate of the industry is; thus being capable of satisfying the rapid demands and needs of our life. A heterogeneous catalyst provides the ease of separation and recovery from the reaction component in contrast to a homogeneous one, and as a heterogeneous catalyst mostly consists of metal nanoparticles as active sites deposited on a support, the conventional focus to improve the catalytic system for a given reaction was to utilize different supports, different metals (or a combination of metals), nanoparticle sizes of active metals, and different methods of synthesis and deposition. There have also been approaches to improve the catalyst via constructing hierarchical porosity in the support when possible (as in metal organic frameworks (MOFs), Zeolites, carbons) which increases the surface area and mass transfer; thus improves the activity and stability. Amongst the many supports applied in industrial heterogeneous catalysis such as zeolites, silica (SiO_2), alumina (Al_2O_3), titania (TiO_2) and many others, porous carbons are considered a leading material by virtue of its unique properties such as thermal and chemical stability, large surface areas, functionalizable surface, the possibility to easily recover the active metal, and potentially low cost. Consequently, carbons have been applied in several industries from medicine to catalysis and electrochemistry. In order to achieve higher catalytic efficiency using carbons, several synthesis methods have been applied where in each the focus was to tailor the pore structure within the carbon material for a certain catalytic conversion. Those methods include (but are not limited to) hard- and soft- templating and salt templating, by which hierarchical porosity (micro-, meso-, and macro- pores) can be achieved. Such

hierarchical porosity can be advantageous especially in reactions where complex macro-polymers are present as for example in the degradation of lignocellulosic biomass (LCB) e.g. lignin. However, in catalysis the active metal deposited on the support plays the main role in a reaction. So, a hierarchical porous carbon support can provide more surface area for the metal to be dispersed and thus to be more exposed to the educt which results in better activity. Nevertheless, the dispersion of active metal on porous support can cause clogging of pores (especially micropores), agglomeration of active metal around the pore (due to lowering of surface energy), or further growth of crystallites of active metal to form larger particles and thus the ultimate active metal activity can be outreached. Of this premise, an advanced industrial catalytic system is required to overcome the previously mentioned challenges. A convenient solution is modifying the porous carbon supports with heteroatoms before deposition of active metal. Heteroatoms can influence the hydrophilicity/ hydrophobicity of the support and the catalyst in general, improves the immobilization of active metal, influence the particle size and distribution, and can enhance the properties of the active metal through an electronic junction effect. Therefore, as carbons have a tunable surface and can be modified with heteroatoms- which give them another advantage over the other industrial supports- herein they have been studied for the development of advanced industrial catalytic systems for different conversions (Hydrogenolysis, oxidation, and hydrogenation) in liquid phase and gas phase, in the aim to provide profound knowledge of heteroatoms' effect on the catalyst properties. An illustration of the concepts discussed during this research is given in (Figure 1).
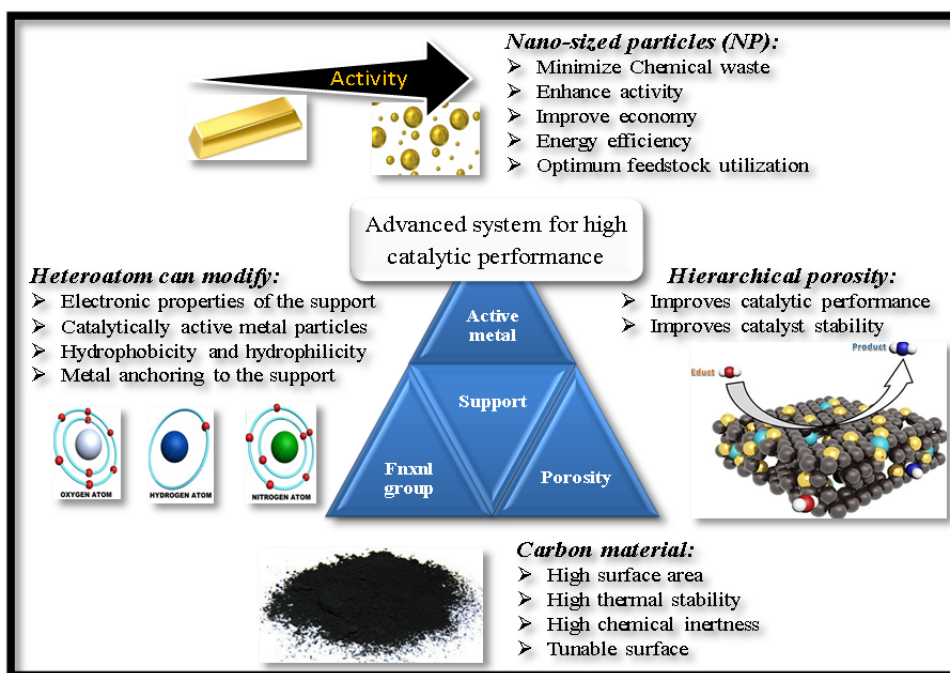
Figure 1: Main concepts discussed in the given research.

Chapter 2

Introduction

"More the knowledge lesser the ego, lesser the knowledge more the ego."
(Albert Einstein)

Preface

In this chapter the following questions are answered: What is the target issue of this research? How can this matter be solved? And what has already been done in research? Moreover, this chapter introduces the main concepts of catalysis and the industrial applications related to this thesis work.

2. State of Art

The world average life expectancy at birth according to the statistics of the world health organization (WHO) for the year 2015 has reached 71.4 years. This is the result of the technological and medical developments reached, as well as to the better life circumstances present. As a result, an increase in the average global population by 75 million person annually or 1.1 % per year is reached according to WHO for the year 2016 [1]. Such an escalation implies higher consumption of goods and energy sources which sets the earths' finite natural resources under strain as shown in (Figure 2). Therefore, it is essential to explore renewable nutritional- and energy- resources that can maintain the needs of the large population and keep the balance of nature at the same time. Catalysis is promising contribute to these goals and provide resolutions for the several matters present these days. Catalysis process already occurs in nature whether as enzymes (active and selective to a specific task) in humans [2], animals or plants [3], or by yeasts used for sugar fermentation [4]. However, depending on these sources alone is insufficient for the rapid growth of population and needs, aside from their processing challenges [5]. Therefore, industrial catalysts [6] – materials produced to mimic the enzymes in its reaction properties – are developed and employed in a variety of applications related to all different sectors of life whether electrocatalysis, photocatalysis, solar energy, pharmaceutical industry, bio- and oil- refineries, or petrochemical industry, and many more.
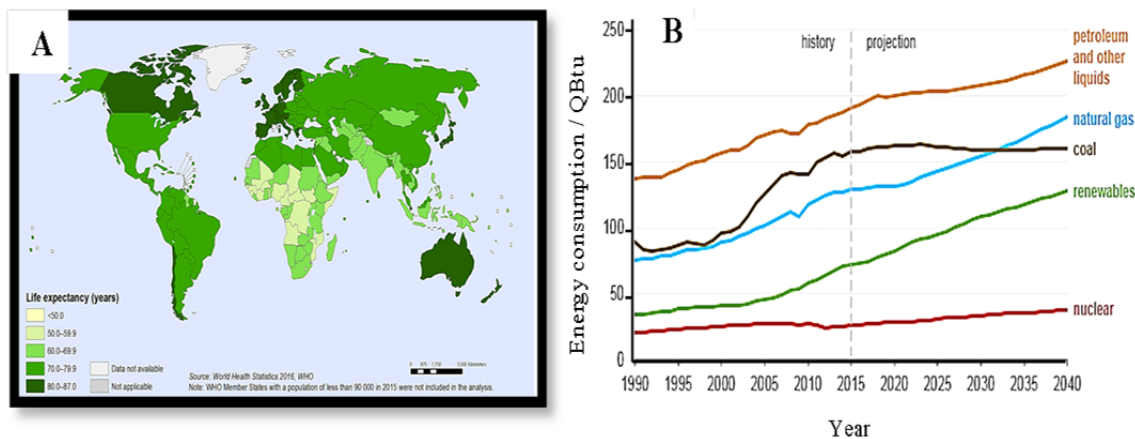
Figure 2: Global life expectancy at birth for the year 2015 for both genders "WHO" [7] (A), and world energy consumption by energy source (1990-2040) in quadrillion British thermal units (QBtu) "EIA" [8] (B).

2.1.   Catalysis

Catalysis has been known since decades especially in fermentation; however, the term catalyst was first noted by Jöns Jakob Berzelius in 1835 [9]. The term is first noted as Kataluein, originates from the Greek language meaning Kata: down and Luein: loosen [10]. Indeed, a catalyst affects the rate of a reaction required to obtain the product, without being consumed during the reaction. It provides an alternative reaction route that requires smaller activation energy (E_a) [11] (Figure 3). This is usually measured by Arrhenius equation [12] (Equation 1).

$$k = Ae^{-E_a/(RT)} \qquad \textit{(Equation 1)}$$

Where the activation energy (E_a) is the energy the reactants in the system need for a reaction to happen at a certain reaction rate (k) in certain reaction conditions (absolute temperature (T) in Kelvin considering the universal gas constant (R)) at a certain temperature *independent* (frequency) factor (A) between k and E_a [11-12].
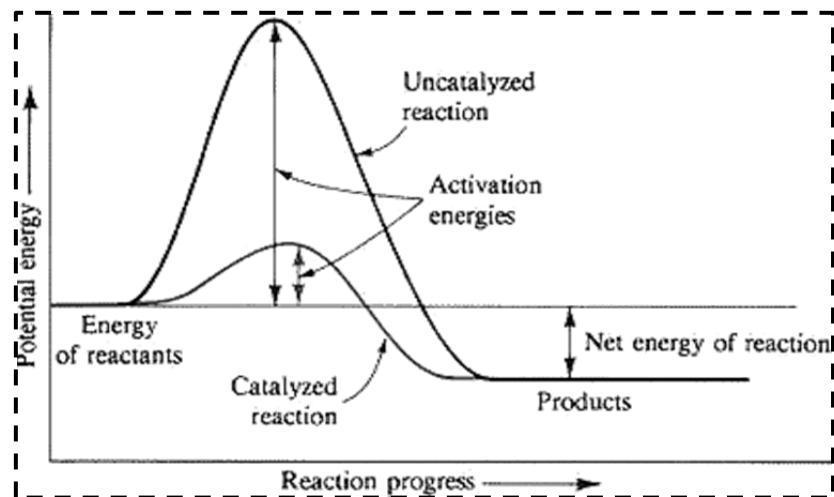
Figure 3: An illustration of the activation energy and rate of reaction in presence and absence of a catalyst [13].

In regards to the concentration of the reactants at the catalyst surface to be temperature *dependent*, other terms have been developed to express the catalytic performance, especially the catalyst activity. One concept is known by the turnover number (TON) or turnover frequency (TOF) or the turnover rate (TOR). These three terms define the number of cycles a catalyst can undergo (n) before deactivation considering the number of active site (S) on the catalyst per unit time (t) [14], as given in (Equation 2) below:

$$TOF = \frac{number\ of\ chemical\ products}{number\ of\ active\ sites\ x\ time} = \frac{1}{S}\frac{dn}{dt} \qquad \textit{(Equation 2)}$$

In some cases (heterogeneous catalysts discussed later in chapter 2.4) the determination of active sites is difficult, therefore this term is replaced with the concept Metal time yield (MTY) also known as space time yield (STY) which considers the quantity of reactant

converted to products (mol or grams) per quantity of active metal used (mol or grams) per unit time (seconds (s), minutes (min) or hours (h)) [14] as given in (Equation 3)

$$MTY = mol_{products} \ mol_{metal}^{-1} \ s^{-1} \qquad \textit{(Equation 3)}$$

In catalysis not only the activity matters but also the selectivity (S) to the desired product and the stability over time. The selectivity can be measured by considering the rate of the desired product (d p) obtained among the rest of the products in the gathered solution (d S_T) after the catalytic reaction [6] as shown in (Equation 4) below:

$$S(p) = \frac{d \ p}{d \ S_T} \qquad \textit{(Equation 4)}$$

A catalyst can be in a gaseous (e.g. Nitroxide), liquid (e.g. Sulfuric acid), or solid state. Industrially, liquids and solids are mostly used and these can be either of organic and bio-materials (e. g. yeast used in fermentation) and referred to as biocatalysis or enzymes, or inorganic material (Sulfuric acid or platinum metal) known as catalysts [6, 11].

2.2. Enzymes vs. Catalysts

Despite the fact that enzymes were the first known catalysts and they can be applied in varied interdisciplinary areas (such as detergents, pharmaceuticals, medicine, Agriculture, Pulp and paper, and food), yet only a small fraction of enzymes is applied industrially (~ 1 % of all known enzymes). They can be made through sustainable development and green chemistry and tend to have unsurpassed selectivity towards specific product, very high chemical conversions (turnover number), and operate under relatively mild conditions. However, biocatalysts suffer from insufficient stability, a long development time, being unstable under elevated temperature and pH conditions, have low specific activity, are only available for selected reactions, and being often expensive [5-6, 11]. Such disadvantages can be overcomed by the catalysts.

2.3. Catalysts

Catalysts can be classified according to the phase in which they operate into homogeneous catalysts and heterogeneous catalysts. Among these, heterogeneous catalysts are industrially more favored. The difference between a heterogeneous and a homogeneous catalyst is the phase boundary where homogeneous catalysts are in the same phase as the substrate and the product (most often dissolved in a liquid phase), but the heterogeneous catalyst is in different phase (most often a solid catalyst in fluid phase). This potentially provides the homogeneous catalysts, which are in most cases organometallic compounds, a

higher degree of dispersion and thus better catalytical performance per active center. However, their difficult separation from the product mixture, and thus limited reusability and extra cost of scaling up or catalyst loss limits its industrial applicability [6, 15]. Therefore, as a heterogeneous catalyst can overcome the issues of an enzyme or a homogeneous catalyst, it is widely applied in variable sections of industry [16]. A short summary is illustrated in (Figure 4)
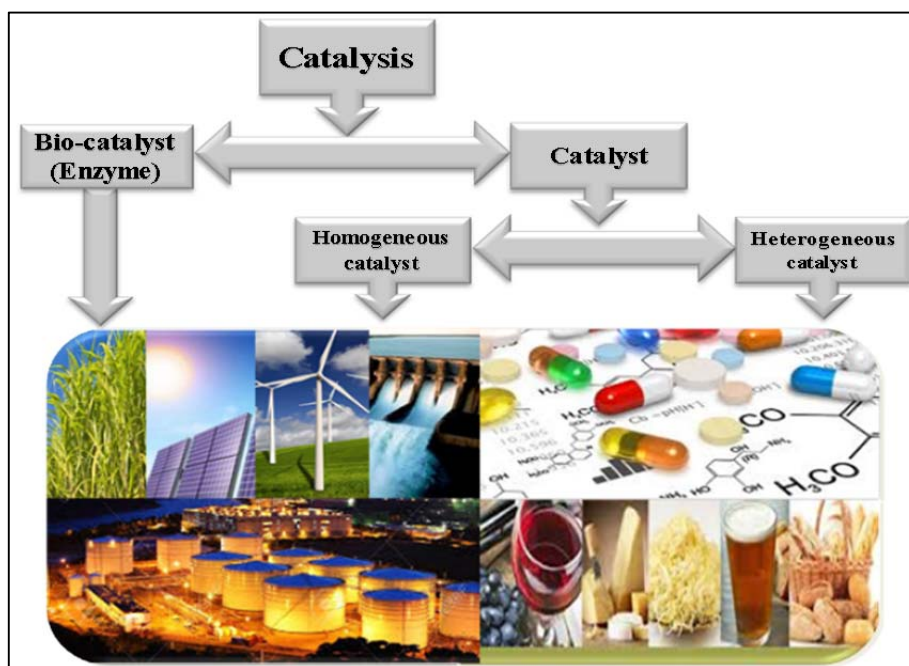
Figure 4: Schematic summary of catalysis in industry.

2.4.   Heterogeneous Catalysts

A heterogeneous catalyst can be having the metal nanoparticles supported (e.g. platinum on carbon) or unsupported (e.g. Raney nickel). The advantages of a supported heterogeneous catalyst allows for a vast range of industrial applications. A support provides a high surface area for effective dispersion of metal particles, induces high activity of metal, maximizes the spatial distance between the metal nanoparticles (MNPs), limits particle growth, facilitates the separation from the reaction medium (e.g. by simple filtration), influences the catalytic performance of the metal, enhances the catalyst stability, and thus can provide economical use of the active metal. Moreover, depending on the structure of the support, the metal can be deposited not only on the surface but in the pores as well. In other words, the textural and chemical properties of the support material impact the catalytic performance of the active metal in a reaction. [11, 15-17].

2.5.   Porous Carbon Supported Heterogeneous Catalysts

2.5.1.   Carbon Materials

Carbon materials have been known since prehistory (e.g. burning woods for warming and cooking) and they are still used to our days for their unique characteristics and widespread important applications. Carbon is the 6th element in the periodic table and ranks the 17th among the rest abundant terrestrial elements. Its ability to bond with other atoms as well with itself in plentiful fashion forming stable substances with less or more electronegative partners, allows the formation of many chemical compounds [18]. Carbon atoms can bind together depending on their electronic configuration to give allotropes of different physical properties. Amongst these allotropes, the sp^3 hybridized diamond for example is a 3-D framework of cubic symmetry with high transparency and the properties of a wide band gap semiconductor. At the same time, it is the hardest natural material (microhardness > 100 GPa). Graphite, on the other hand, is a carbon modification with sp^2 hybridization consisting of stacked planar sheets in hexagonal stacking making it highly electrically conductive, non-transparent, and one of the softest materials (microhardness ~1 GPa). Carbon nanotubes, another interesting allotrope, exhibit high tensile strength, high electric and thermal conductivity, high ductility, and high thermal and chemical stability. Beside these basic elemental modifications, plenty of other carbon materials (such as powders, fibers, and foams) of varied mechanical, electrical, and chemical properties exist, providing in general high surface area, high thermal stability, high chemical inertness, and a tunable surface. Hence, carbons are useful for widespread applications ranging from automobile to medicine industries, and catalysis to energy storage. Another indication of how remarkable carbon materials are and how widespread carbon chemistry is, Elsevier Science has dedicated and published a Journal called (*Carbon)* for this element. In addition there exist a large number of books representing only the carbon element, its structure, properties and applications. [19-22]. An illustration of carbon allotropes and applications is given in (Figure 5).
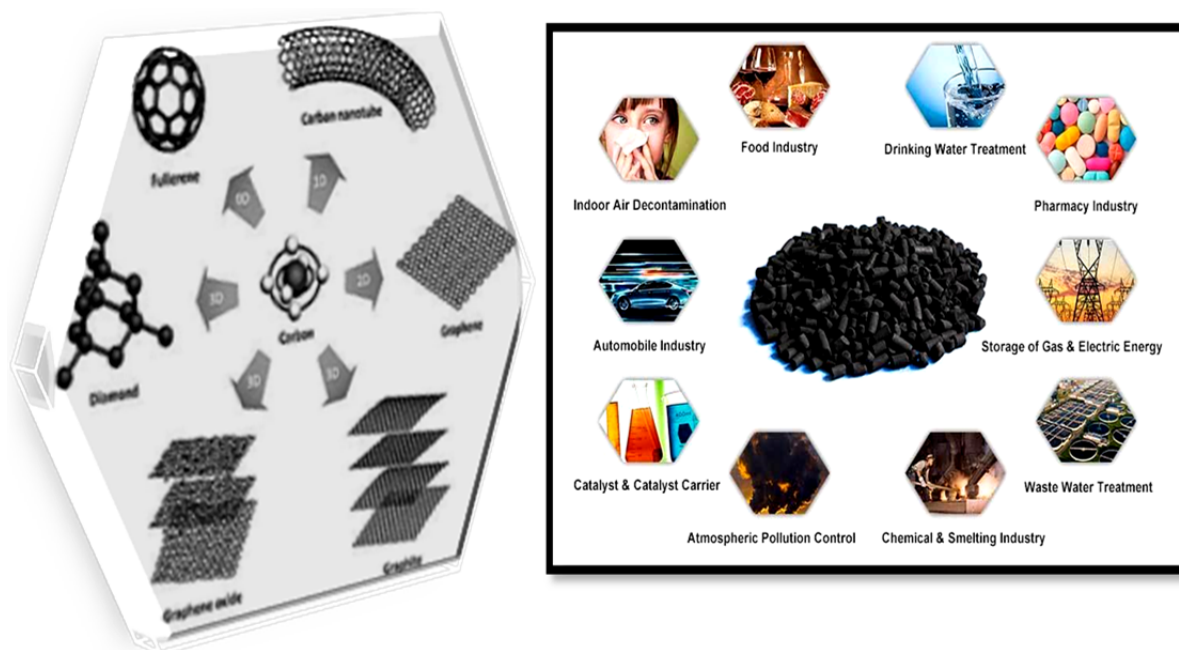
Figure 5: Different carbon allotropes (left) and the different industrial applications of carbon in industry (right).

2.5.2. (Hierarchical) Porous Carbon Materials

Porous solid materials are materials that contain voids in their internal surface area which are deeper than they are wide. These voids are known as pores and they vary in geometry (cylindrical, ink-bottle shaped/ spherical, slit, interstices, and funnel shaped/ conical) and size. The pores can be opened (accessible) or closed (inaccessible). The open pores can be blind (with a dead end), or inter-connected pores (connecting between the pores). According to IUPAC the pores are size categorized by their diameter (d) into:

- Micro-pores: d < 2 nm
- Meso-pores: 2 nm < d < 50 nm
- Macro-pores: d > 50 nm.

Three parameters are measured to characterize the porosity of a material its specific surface area (SSA), its total pore volume (TPV), and its pore size distribution (PSD) [23].

The importance of porosity in a material is not only to enhance its surface area by providing more contact between the surface of the material (inner and outer surface) and the surrounding phase, but by also providing efficient mass transfer. This can be possible by tuning the porosity in the material in accordance to the application.

Although the material can contain each pore type alone with a certain size distribution, it can also contain two or more pore sizes "hierarchical porosity" depending on the method to prepare the material. In some applications e.g. catalysis, the presence of a hierarchical porosity can improve the surface area of the material and the mass transfer within the

catalyst; hence influencing the catalytic performance [24-25]. A macropore system can minimize diffusion distances by serving as a micro – reservoirs, and a mesopore can provide larger accessible surface area and smaller ion-transport resistance, while a micropore system is beneficial for shape-selectivity and size- selectivity for guest molecules. Together as hierarchical system (for example macro-meso pores, or meso-micro pores) they can provide higher surface area with strong adsorption ability and avoid the mass transfer limitations resulting from the use of one pore system as micropores [26-27]. A depiction for the porosity and mass transfer in shown in (Figure 6).

Figure 6: Depiction for the different porosity and its importance in mass transfer.

Hierarchical porosity already exists in nature whether in trees for transportation of water and minerals to its upper parts, or even in human body in the lungs for example where branched pores for the exchange of oxygen and carbon dioxide are present at the interface between the lung and the air. Such accessible large surface area in a small space is desirable in many applications especially in catalysis for the aforementioned reasons. Carbons as supports stand out from other supports in being surface tunable and thermally stable in addition to the preparation from several cheap raw precursors and their high surface area. Therefore, improving its performance in catalysis is important and possible by tuning its porosity for a higher surface area and better mass transfer. A typical porous carbon such as activated carbons (ACs) can have up to 3000 m^2 /g of surface area [28] depending on the synthesis method and the size of its structural pores. Several synthesis methods are known for designing and templating the pore size in regard to carbon material. These methods vary according to the application intended. For example, in gas adsorption applications, more microporous system is favored whereas in catalysis a hierarchical porosity (meso– to macro–pores) are of an advantage especially for heterogeneous supported catalysts; therefore different synthesis methods are developed [29].

2.5.2.1.   Synthesis of Porous Carbon Material

As aforementioned, the synthesis of carbon and tuning its porosity is relevant to the intended application. In Industrial heterogeneous catalysis, carbons are mostly used as supports. Therefore, the method of synthesis needs to be economic, provides scaling up, and of course it has to provide the desired hierarchical porosity system for the above mentioned reasons.

Industrially, physical and chemical activation methods are applied for porous carbon synthesis. The *physical activation* is based on pyrolysis (temperatures above 500 °C) of raw material (e.g. coal, wood, fruit shell, polymers) into char at an inert gas atmosphere followed by the addition of activation agents (CO_2 or H_2O) which are inducing an etching of the carbon thus introducing porosity (etching of carbon in presence of CO_2 is a result of Boudouard equilibrium as in (Equation 5), while in presence of steam a water gas shift (WGS) takes place (Equation 6) followed by etching (Equation 7)). The disadvantages of such a synthesis are the resultant of small pore sizes which result in limited mass transfer of the molecules, the formation of undesirable defects and functional groups causing low in conductivity, and the instability of pore structure at high temperatures (e,g, during graphitization) [30].

$$x\ CO_2\ (g) +\ C_y(s) \rightleftharpoons 2x\ CO\ (g) +\ C_{y-x}(s) \qquad \textit{(Equation 5)}$$

$$x\ H_2O\ (g) +\ C_y(s) \rightleftharpoons x\ CO\ (g) +\ C_{y-x}(s) + xH_2(g) \qquad \textit{(Equation 6)}$$

$$CO(g) +\ H_2O\ (g) \rightleftharpoons CO_2(g) +\ H_2(g) \qquad \textit{(Equation 7)}$$
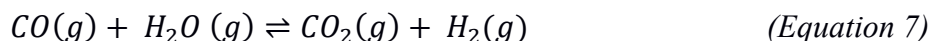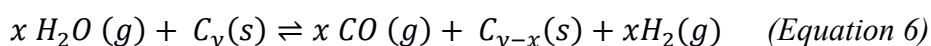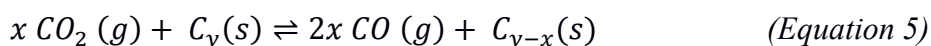
On the other hand, the c*hemical activation* is carried out by impregnating a raw carbon material with highly concentrated aqueous solution of a chemical activation agent such as potassium hydroxide (KOH) or zinc chloride ($ZnCl_2$) where dehydration for example with KOH occurs yielding H_2O (Equation 8) which by a steam activation process forms the porosity which results with carbon dioxide (CO_2) formation. This CO_2 reacts with the formed potassium oxide (K_2O) to produce potassium carbonate (K_2CO_3) (Equation 9). Moreover when pyrolyzing (Temperature >700 °C) the K_2O can be reduced to elemental potassium (K) by H_2 or the carbon causing carbon etching (porosity formation) (Equations 10 and 11). At the same time the K can go mobile and intercalate between the carbon layers causing layer separation which after washing the active agent forms a high internal micro-porosity [24, 31-32].

$$2\ KOH\ (s) \rightleftharpoons K_2O\ (s) +\ H_2O(g) \qquad \textit{(Equation 8)}$$

$$CO_2(g)\ +\ K_2O\ (s) \rightleftharpoons K_2CO_3\ (s) \qquad \textit{(Equation 9)}$$

$$K_2O\ (s) + H_2\ (g)\ \rightleftharpoons 2\ K\ (l) +\ H_2O\ (g) \qquad \textit{(Equation 10)}$$

$$x\ K_2O\ (s) + C_y(s) \rightleftharpoons 2x\ K(l) + x\ CO(g) + C_{y-x}\ (s) \quad \textit{(Equation 11)}$$
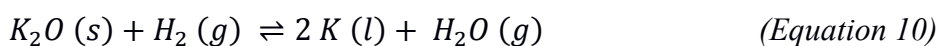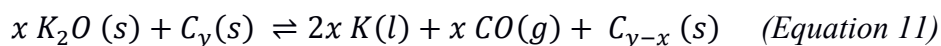
The pores resulting, whether by chemical or physical activation synthesis, are most often disordered and undefined micropores which contain a bottleneck or worm–like structure that are only a dead end for the mass transfer [33-34]. In accordance, other methods (such as soft– and hard– templating, and salt–melt synthesis) have been developed. These can overcome the drawbacks of activation synthesis and provide control of pore morphology. The main principle of templating is a structure directing material in which the carbon raw substance is synthesized, and the removal of the template results in porous carbon structure. Like that, templating offers a defined pore size and pore structure. According to the mechanism and the type of the structure directing agent, templating can be classified into soft– and hard– templating (also referred to as endo- and exo-templating respectively) [35].

Soft templating is to create a porous carbon structure from carbon precursor being structure directed/ templated via capturing on the surface of a micelle or liquid crystal, then allowed to crosslink, and then carbonized. The main drawback of soft templating is the fact that the polymer layer (structure directing agent) is thermally removed causing shrinkage of pores.

Hard templating is the use of a porous solid template as a mold filled with carbon precursor then heated to carbonize and remove the template ending up with porosity dictated by the structure of the mold. An illustration of soft and hard templating is given in (Figure 7).

Although hard templating overcomes the shrinkage of pores issue as present in soft templating, yet using hard templating synthesis it is challenging to infiltrate the precursor in the mold completely, or maintain low volatility of the precursor with sustained volume size. Multiple infiltrations can be applied to fill the mold pores completely, or a melt infiltration can be applied for homogeneous filling of the template pores. However, industrially hard templating is unfavorable for the cost, time, and material required to synthesize the template/ mold [36]. In conclusion, the Activation methods have limited control of porosity, the soft templating is difficult to synthesize and the hard templating is quite expensive with multiple step approach.
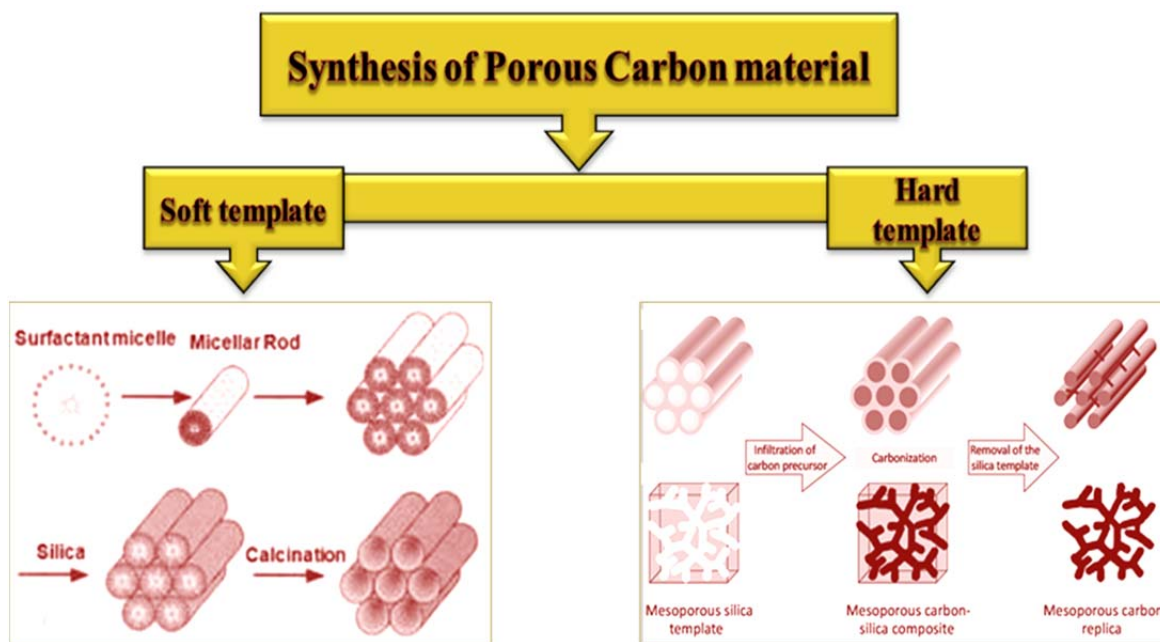
Figure 7: Schematic summary of soft and hard templating.

2.5.2.2.   **Salt–Melt Synthesis of Porous Carbon Material**

Salt–melt synthesis also referred to as salt templating (Fechler et. al) is when a carbonization reaction takes place in an ionic solvent, precisely in a eutectic molten salt [37]. This approach combines the advantages of high thermal stability of solvent during carbonization and high mobility of the reactants providing by that highly porous carbons. Three parameters need to be considered for the precursor–salt systems used [38]:

- Higher operating temperature than the melting point of the salt.
- Adequate solubility of carbon precursor in the molten salt.
- The salt–melt "solvent" is inert under reaction conditions.

Metal halides (e.g. Zinc Chloride $ZnCl_2$, or potassium chloride KCl) are most suitable for such reaction conditions. They are inert and their melting point can be adjusted (decreased) if a eutectic salt mixture is used; hence allowing the use of precursors with low decomposition temperature, such as inexpensive and sustainable sugars (e.g. glucose and glucoseamine). The application of salt–melt synthesis for synthesis of porous carbon materials was introduced by Liu et. al. [39]. A eutectic LiCl/ KCl salt mixture was added to glucose precursor and then heated under inert gas. Aqueous washing of remaining salt followed to obtain the porous carbon material. The results showed that the amount of salt mixed with the precursor can influence the carbon structure and porosity in a similar way as in templating.

The investigation proceeded by applying different salt to precursor ratios and different temperatures. The use of low salt to precursor ratio (10:1) resulted with irregular hierarchical randomly interconnected microporous carbon. In contrast, at high salt to precursor ratio (100:1) a graphene–like material of similar specific surface area (SSA) as that with lower salt ratio was obtained. The difference in morphologies is explained with different carbonization mechanism where the high ratio resulted in a solution process giving graphene structure, and the low ratio is a mean of precipitation producing the interconnected carbon morphology. The increase in temperature up to 700 °C led to an increase in SSA reaching 600 m^2 g^{-1}, however further temperature increase led to an opposite effect on SSA presumed to be a result of enhancing carbon layer stacking.

In the study related to salt–melt synthesis done by Fechler et. al. [37] They apply inorganic $ZnCl_2$ salt mixture mixed with carbonizable ionic liquids (ILs) in a 3:1 wt. ratio and treat the mixture at 1000 °C in an inert gas atmosphere. Aqueous washing followed the carbonization step to yield highly porous carbon material with SSA of 2000 m^2 g^{-1}. The main finding of this work was that the morphology/-pore structure of carbon is dependent on the salt mixture. The reason behind that lies in the different properties of the eutectic salt mixtures such as melting point, viscosity and polarity. They showed that a $LiCl/ZnCl_2$ salt mixture results mainly in microporous carbon, replacing the LiCl with NaCl resulted in hierarchy in porosity of supermicropores and small mesopores. This effect was related to the low melting point and the formation of large clusters of $NaCl/ZnCl_2$ salt mixture when the phase demixes at the later stage of carbon condensation in comparison to $LiCl/ZnCl_2$. Another comparison was made by using KCl instead. As $KCl/ZnCl_2$ mixture has the lowest melting point among the mentioned salt mixtures, the outcome was a hierarchical (micro to meso) porosity of spherical carbon particles. The explanation given is the enhancement of phase separation at early stages of the crosslinking process. A sketch of the different porosity in carbon by the different salt mixtures is illustrated in (Figure 8).
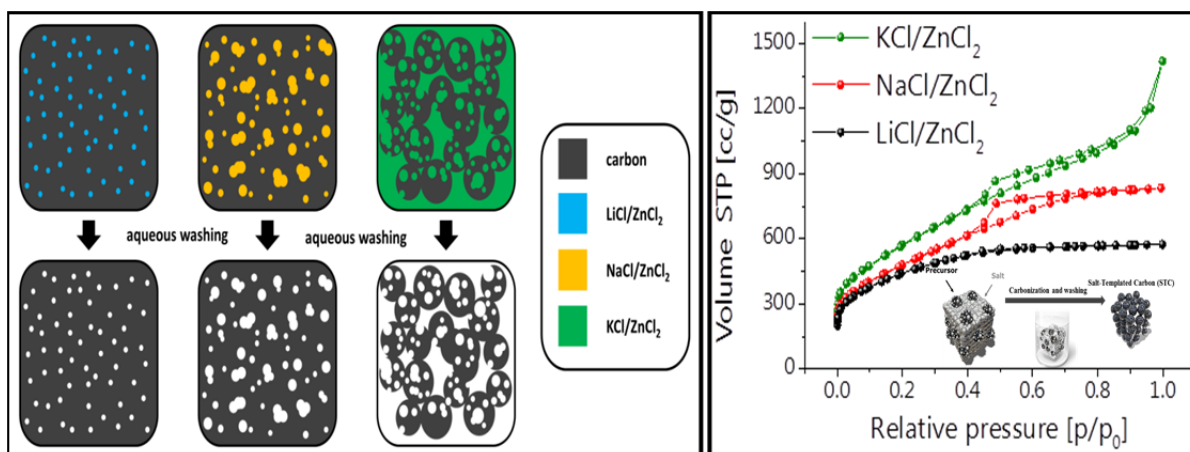
Figure 8: Sketch of the different porosity in carbon by the different salt mixtures [37].

In conclusion to the discussed methods and results, the salt–melt synthesis can be considered a promising method of synthesis for porous and even hierarchically porous carbon materials. It overcomes the challenges present in previously mentioned processes by providing better morphology control, facile "template" (salt-melt) removal, and possible scale up of the production. It can in a one pot synthesis provide porous carbon with functionalized surface if the carbon precursor contained functional groups. Accordingly, the salt–templating synthesis process referred to as *salt–melt synthesis* here was adapted for the research described in this thesis with the difference of using sugars instead of ILs and reducing the temperature applied. Thus, KCl/ZnCl$_2$ salt mixture is used as the solvent medium along with sugar compounds such as glucose and glucoseamine as precursors at low salt–precursor ratio 3:1 and at moderately high temperature of 900 °C.

2.6.   Heteroatom Functionalization of Porous Carbon Material

Catalysis has gone through so many developments and changes as well as discoveries. Catalysts have been in continuous change and progress since ever discovered/ applied around the 18th century. First, there was the metal discovery and understanding of its properties then applying and comparing metals to each other to realize its oxidation/ reduction manners (development of catalytic performance concept). Later by the development of analysis, synthesis and extraction methods and techniques, the need for catalytic optimization commenced and the heterogeneous catalysts were applied. Afterwards, nanotechnology and nanomaterial concepts evolved and the quest for new preparation methods of nanoparticles of a metal (also referred to as metal nanoparticles MNPs and represents particles sized between 1 and 100 nm) deposited on a support emerged, followed by the porosity importance in a system and its tuning procedures. All these changes and evolvements in the science of catalysis resulted not only due to new technologies development and new chemical, physical and theoretical principles arising, but also the challenges resulting of the request for energy resources and environmental friendly chemistry, and of course reaching to the parameters of an economical industrial production level [40].

Certain principles in regard of a heterogeneous catalyst cannot be overlooked for an enhanced catalytic performance such as the nanoparticle size of the metal, the presence of a support, and the porosity or structural properties of a support. These mentioned principles are intensively studied for several materials even for carbon material. Nevertheless, surface

functionalization of the support with heteroatoms, understanding its effect and applying it for catalysis is only briefly discussed in literature. Heteroatoms can have a big influence on the support properties and the catalyst performance as well as on the surrounding phase. Ergo, introducing heteroatoms (e.g. N, O, or H) to the carbon materials prompts for new approaches in tailoring the catalytic properties towards diverse applications. Heteroatoms (e. g. N) doped in the semiconducting carbon materials alter not only its surface properties but also its electronic structure. Mostly, the focus in research has been on N-doped carbons (NDCs) which attributed to improving electrical conductivity, basicity and oxidation stability for electrocatalysis applications. The introduction of N- heteroatoms to carbons can be distinguished either as surface or structural modification. The surface functionalization (e.g. amine) can hardly change the original properties of the carbon framework significantly, while the structural modification (e.g. graphitic nitrogen) is behind the difference in the physical properties if compared to non-doped materials [41] as given in (Figure 10). It is presumed that structural nitrogen modifies the band structure by lowering the valence band (E_v) and increasing the electron density at Fermi–level (E_f) as illustrated in (Figure 9). By that, carbon becomes more chemically stable which is referred to as "noble carbons" [42]. In the case of surface modification, mainly Brønsted basicity is introduced, whereas in the structural case N adds a Lewis-basicity to the carbon [43]. However, the influence of heteroatoms is not restricted to N, and other heteroatoms can be suitable for tuning carbon and inducing different effects.
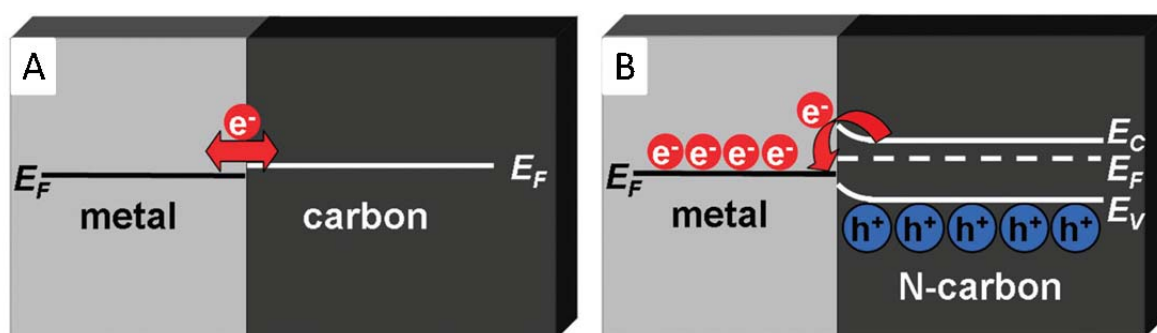
Figure 9: Illustration of metal – carbon support interaction at fermi level for non-doped carbon (A) and N-doped carbon (B) [43].

Heteroatom modification of a material was achieved through either thermolysis or chemical vapor deposition (CVD) of a heteroatom–containing precursor, or by post treatment of carbons in a heteroatom–containing atmosphere. Despite the functioning of these methods, they produce low yield, require a multi–step synthesis and are difficult to process. To overcome these drawbacks, a one–pot synthesis approach of the salt–melt carbon synthesis from a heteroatom–containing precursor is used in this thesis work.
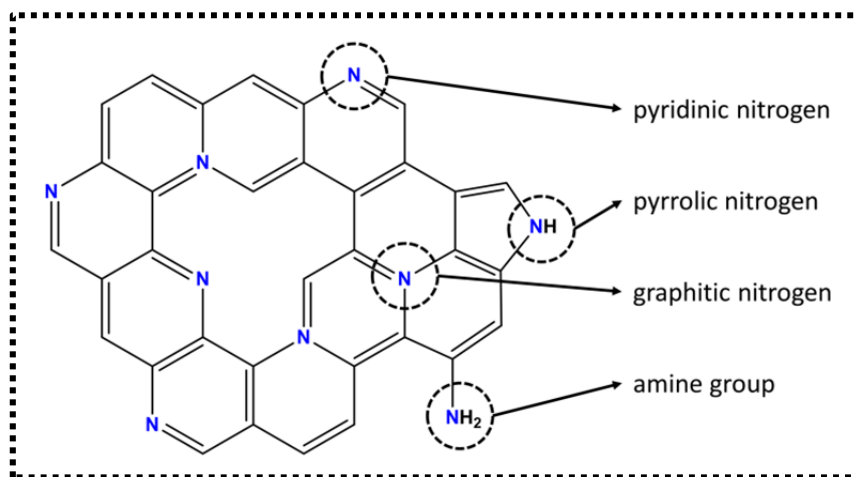
Figure 10: Illustration of various possible nitrogen states doped in carbon as functional group.

2.7.   Heterogeneous Catalyst Mechanisms of Reactions on Surfaces

When discussing catalysis, it is essential as well to discuss the mechanisms that take place during a reaction. In heterogeneous catalysis the metal nanoparticles (MNPs) deposited on the support exist as a separate phase from the phase where the reaction takes place. In accordance to Sabatier principle, the catalyst disrupts the bonding of the reactants when they interact with its surface and an adsorption process takes place. The strength of the adsorption is expressed as enthalpy/ heat of adsorption (ΔH_{ads}). Chemisorption (chemical bonding resulting of the reactant adsorbed to the surface) and physisorption (weak van der Waals interactions e.g. gas adsorption to a surface) interactions take place depending on the electronic – or bonding structure of the reactant adsorbed. In the case of chemisorption the activation energy is involved and the adsorbed species is a monolayer.

Several mechanisms (illustrated in Figure 11) occur in a heterogeneous catalysis reaction upon these are the dissociative adsorption, the Langmuir-Hinshelwood mechanism, and the Eley-Rideal mechanism. The dissociative adsorption mechanism is when dissociation/ breaking of bonds happen after chemisorption on the surface (e.g. Hydrogen (H_2)). The Langmuir-Hinshelwood mechanism describes the interaction between two reactive adsorbed species on the same surface with one another where interchange of atoms is possible (e.g. carbon monoxide oxidation to carbon dioxide). Finally, the Eley-Rideal mechanism states that an interaction happens between an adsorbed species on the surface with another reactive species from the surrounding phase but it is not adsorbed to the surface (e.g. carbon monoxide interaction with oxygen for carbon dioxide formation) [44].
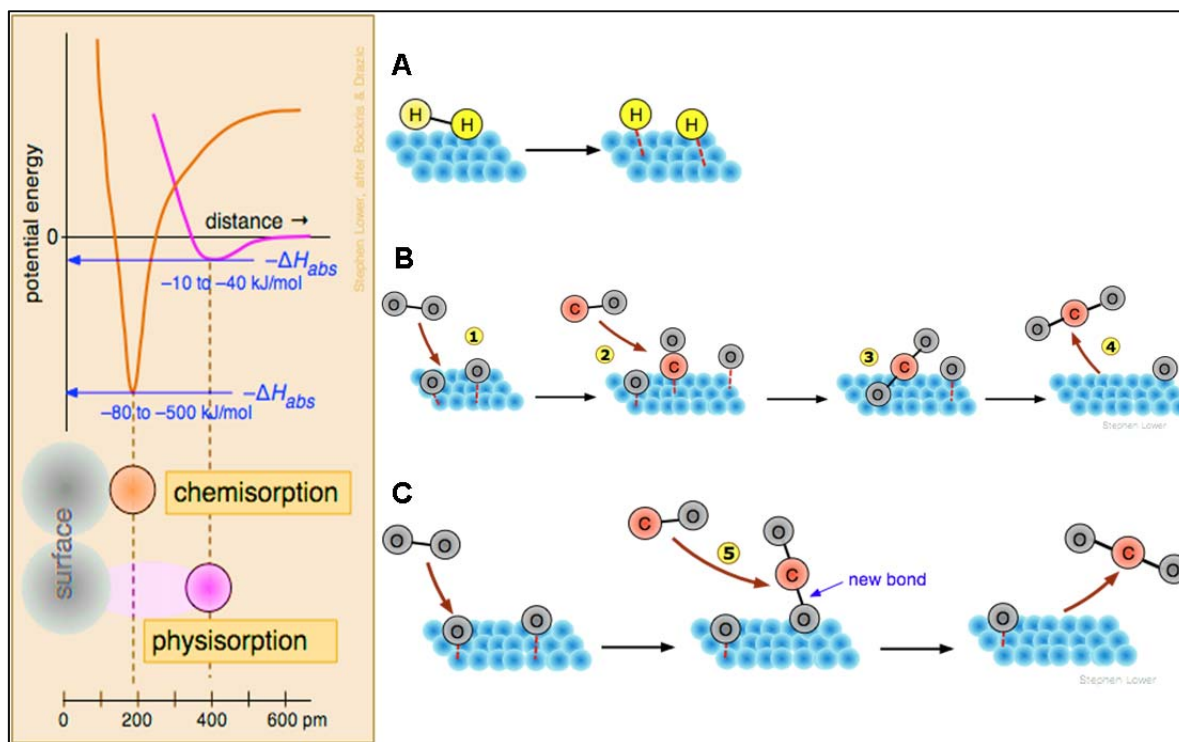
Figure 11:A summary of chemisorption and physisorption (left) and the mechanisms on the surface of heterogeneous catalysts (right), A) association desorption, B) Langmuir-Hinshelwood mechanism, and C) Eley-Rideal mechanism [45].

2.8.   Applications of Industrial Heterogeneous Catalysts

As mentioned earlier, the key to maintaining life balance and produce chemicals and energy resources can be via catalysis, especially the application of industrial heterogeneous catalysts. In correspondence, fossil fuels can provide the chemicals and fuels necessary, but their depletion and instability, the economic and political issues surrounding them, aside from their contribution to the environmental pollution all request for alternatives. Lignocellulosic biomass (LCB) and synthetic gas (syngas: CO and H_2) are few of many other alternatives favored over fossil fuels. The LCB and syngas sources are very interesting alternatives compared to the other alternatives present (such as solar energy, wind energy, or hydrodynamic energy). Catalytic transformation of these can not only produce energy and fuels, but also can provide vast of value-added chemicals (Figure 12). The raw material providing these sources is abundant, cheap, renewable, and less valuable as is, that performing catalytic transformation especially with carbon nanomaterials on the raw material for important chemical production is of an advantage [20].
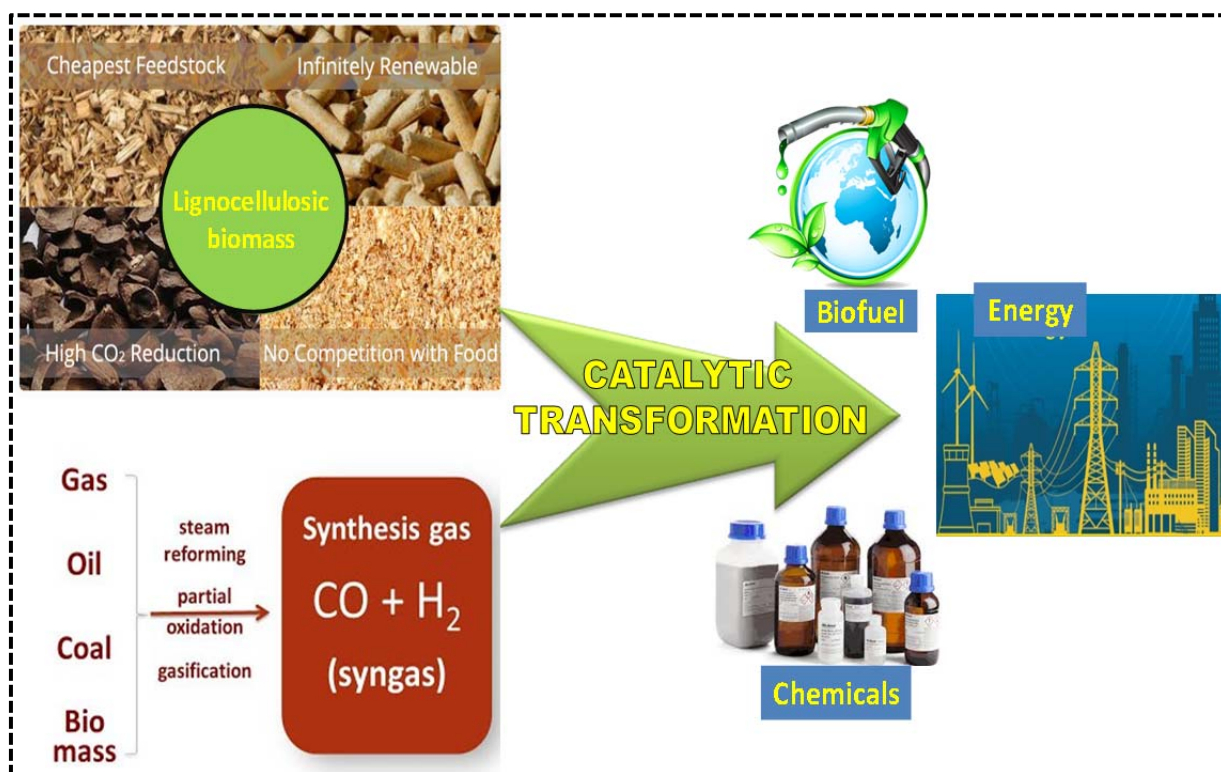
Figure 12: Schematic illustration of catalytic transformation of LCB and syngas as sources of chemicals, biofuels, and energy

It is essential to mention that carbon nanomaterials are applied in several other applications amongst them in pharmaceuticals, photo-catalysis, nanomedicine and filtration in where complex interactions with aqueous/ liquid phase are involved. These interactions remain poorly understood. Therefore, investigating the catalytic performance in liquid phase reactions (LPR) can provide further insight regarding such interactions and contribute to the scientific understanding of these interactions. In regards, this thesis studies the catalytic performance of nickel nanoparticles (Ni NPs) and gold nanoparticles (Au NPs) deposited on amorphous modified carbon supports for hydrogenolysis of kraft lignin reaction and oxidation of glucose reaction in a LPR (Chapters 4.1 and 4.2) respectively, but also looks into the catalytic performance of iron nanoparticles (Fe NPs) deposited on surface functionalized carbon nanotubes for syngas transformation to liquid hydrocarbons via a Fischer-Tropsch reaction (Chapter 4.3).

2.8.1. Lignocellulosic Biomass Transformation: Kraft Lignin and Glucose

Lignocellulosic biomass represents a promising sustainable renewable solution for replacing petroleum oil and assisting in reducing CO_2 emissions. It is composed mainly of cellulose (40–50 %), hemicellulose (16–33%), and lignin (15–30%) [46]. Cellulose is the most abundant renewable polymer source. It is used in the form of wood and plant fibers as

energy source, as well as used for building materials, paper, textiles, clothing, and many other fields in industry. It is a linear crystalline homopolysaccharide with a repeating unit of glucose dimers. Hemicellulose is mainly made of pentoses (xylose and arabinose) and hexoses (galactose, glucose, and mannose) as well as non-sugar components (e.g. acetyl groups). Lignin (from Latin lignum meaning wood) is the second most abundant renewable polymer after cellulose. It is a macro–polymer of aromatic lignols and consists of p–coumaryl, coniferyl and sinapyl alcohols. The catalytic valorization of hemi- and cellulose yields a variety of chemical building blocks especially sugars and their derivatives, while lignin represents a good renewable source of aromatic groups that vary in accordance to the source of lignin i.e. softwood (guaiacyl groups) or hardwood material (guaiacyl–syringyl groups) [47]. A summary of the composition of LCB is given in (Figure 13).
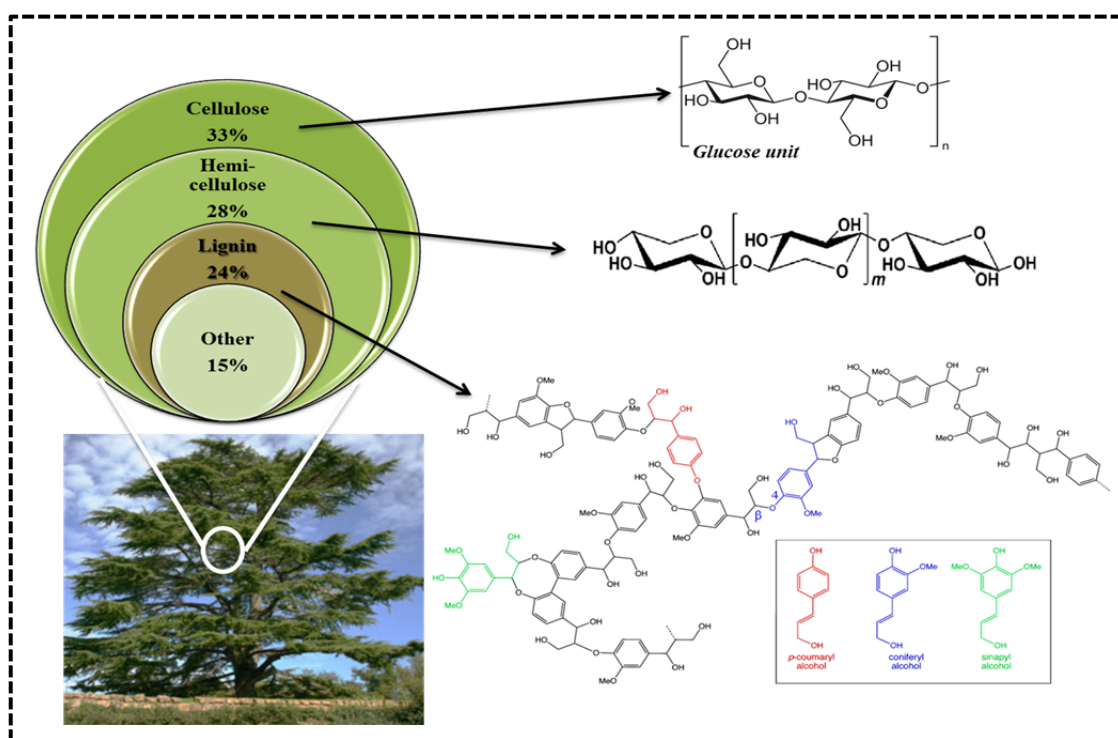
Figure 13: Summary of lignocellulosic biomass composition

In a cell wall, hemi- and cellulose form a rigid structure presenting the backbone of the cell wall and lignin provides the rigidity and resistance against external chemical or physical stress. Such a property burdens the degradation of lignocellulose for effective conversion unless it is sufficiently pre-treated. The most dominant pretreatment method is the kraft lignin process employed by pulp and paper industry. The separation of lignin from the other lignocellulosic components goes through harsh conditions (pH 2- 12, and 420-450 °C temperatures)[48] in presence of sodium hydroxide and sodium sulfide. The production of extracted lignin by pulp and paper industry is estimated about fifty million tons per year, but the lignin-product markets are limited to low value products (e.g. binding agents). Hence, around only two percent (2%) of extracted lignin is applied commercially whereas

the rest is commonly being burnt as a low value fuel, which is a huge loss of chemicals. The aromaticity of extracted lignin along with its abundancy and economic price in presence of the petroleum oil issues has a significant potential to contribute to the production of phenols that can be applied either as fuel sources or as chemical platforms for variable applications [48]. By that, a lignin hydrogenolysis processes is necessary to be developed. Hence, kraft lignin degradation via hydrogenolysis is studied here.

As already discussed, cellulose structure is a building block of glucose dimers. Glucose can be obtained from variable sources as starch or fat, and also from LCB. Such an abundant glucose source is important, especially because glucose applications are ranging from catalysis to crucial biofuel production and medicine. One important application of glucose is its oxidation into gluconic acid. Gluconic acid has versatile uses in chemical, pharmaceutical, food, beverage, textile, construction, and other industries. It is annually produced in 60 KT per year and costs 1.5 €/ Kg. It is industrially produced via microbial oxidation (fermentation) of glucose. However, fermentation process has several disadvantages related to the operational difficulties (e.g. enzyme activity maintenance, slow reaction rate, disposal of accumulated dead microbes), which can potentially be overcomed by metallic heterogeneous catalyst for oxidation of glucose as shown in (Scheme 1). Despite the efforts (e.g. applying platinum (Pt)/ palladium (Pd)/ bismuth (Bi) and a mixture of these), more improvement in catalytic activity is needed. Gold nanoparticles (Au NPs) have been reported to exceed the activity of the previously mentioned noble metals especially when deposited on a metal oxide support (i.e. Al_2O_3), but being 100% selective to sodium gluconate production. In another study by Rossi et.al., Au NPs deposited on carbon showed better activity than other noble metals deposited on the similar support. However, as carbons contain acidic functional groups on their surface, the methods of depositing Au NPs on carbon are challenging. [49-52] Therefore, a need for highly active heterogeneous catalyst with high selectivity towards gluconic acid production is required, as well as a suitable deposition method of Au NPs is needed. In this regard, gluconic acid production via glucose oxidation using catalytical Au NPs deposited on surface functionalized carbon supports is considered for this study.
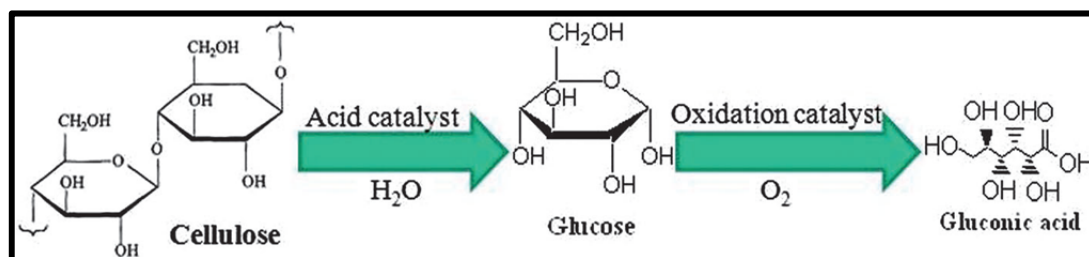

Scheme 1: Catalytic transformation of cellulose to glucose and oxidation of glucose to gluconic acid [53].

2.8.2. Syngas (CO and H_2) Transformation

The potential of lignocellulosic biomass lies not only in its degradation to obtain value added chemicals, but also in its produced gaseous phase out of its degradation process. After all, lignocellulosic biomass is made of carbohydrates that can be converted by reforming processes to valuable gases (e.g. synthesis gas which is a mixture of CO and H_2) which are useful for the production of hydrocarbons with different chain lengths, especially high value short olefins, and C_{5+} components such as fuel, diesel or waxes. The process involved in production of hydrocarbons from carbon monoxide (CO) hydrogenation is known as Fischer ‒ Tropsch synthesis (FTS) discovered in the 1920s. Usually the gaseous substrates (CO and hydrogen (H_2)) for this process can also be produced from coal or natural gas. This process is already widely applied in industry because it provides an alternative way for the production of chemical compounds which are commonly obtained from crude oil as the feedstock. The FTS yields high quality and clean hydrocarbon–based transportation fuels (due to low aromaticity and low content of impurities such as sulfur). Besides fuels, production of olefins and C_{5+} is highly desired because they present essential building-blocks for high-value chemicals, which are mainly obtained from petrochemical feedstocks, such as monomers for the production of plastics (e.g. styrene, ethylene, or propylene). However, the selectivity in the production of different chain length hydrocarbons via FTS is poor based on Anderson-Schulz-Flory (ASF) distribution. The carbon number of hydrocarbons produced differs according to the chain growth probability (α). Hence, adjustment to the probability (α) is required to increase the selectivity towards lower olefins. This is possible by altering the conditions that influence the (α) which are: the FTS conditions (e.g. temperature, pressure, and syngas ratio), the active metal type, the support, and the promoters [54].

2.8.2.1. Fischer-Tropsch Synthesis

FTS is an exothermic catalytic process where a conversion of syngas (CO and H_2) into different molar mass hydrocarbons in presence of a metallic catalyst occurs, as given in (Equation 12) below:

$$(2n + 1)\, H_2(g) + nCO(g) \rightarrow C_nH_{(2n+2)} + n\, H_2O(l) \qquad \textit{(Equation 12)}$$
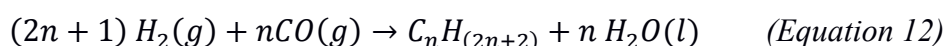
Where n is an integer.

In addition, another reaction takes place during the synthesis process which is the water-gas shift reaction (WGS) as given in (Equation 13) below:

$$H_2O(l) + CO(g) \rightarrow CO_2(g) + H_2(g) \qquad \textit{(Equation 13)}$$
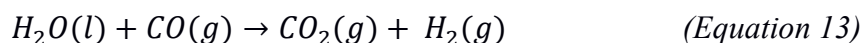
This reaction (WGS) is important to maintain the efficiency of a maximum conversion of syngas by increasing the H_2/CO ratio. The production of the different hydrocarbons as aforementioned depends on ASF distribution in accordance to α. This can be summarized by the given (Equations 14 -15) below:

$$P_n = \alpha^{(n-1)}(1 - \alpha) \qquad\qquad \text{(Equation 14)}$$

$$W_n = n\,\alpha^{(n-1)}(1 - \alpha)^2 \qquad\qquad \text{(Equation 15)}$$

Where P_n is the probability of producing a hydrocarbon of length n, W_n is the weight fraction, n is an integer, and α is the probability chain growth, $\alpha^{(n-1)}$ is the probability of adding n-1 carbons and (1-α) is the probability of terminating the chain growth as illustrated in (Figure 14).
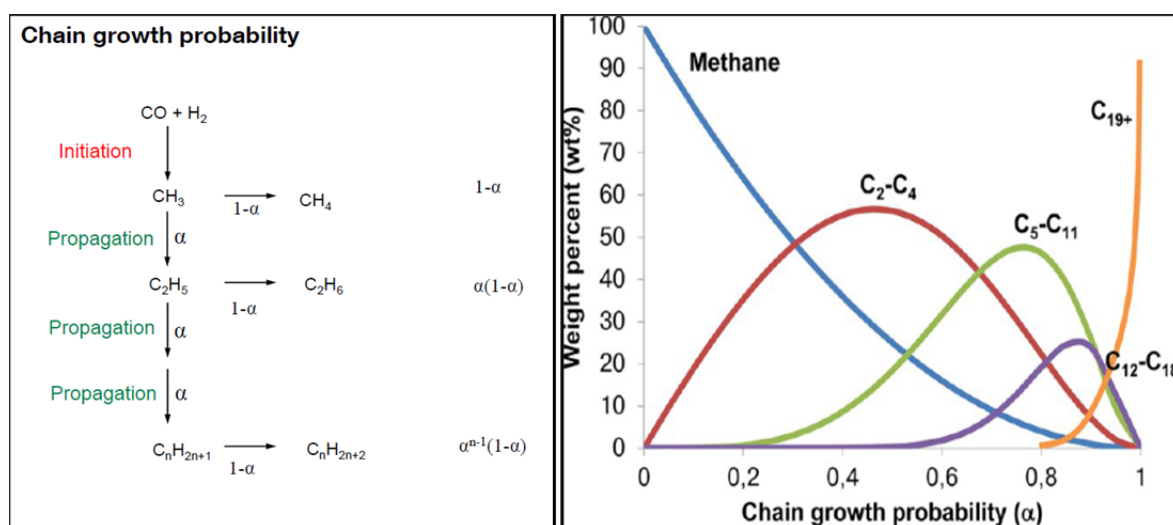
Figure 14: Chain growth probability according to Anderson-Schulz-Flory distribution [55].

As a result of the previous equations, the chain growth probability (α) can be tuned by controlling the reaction conditions depending on the active metal choice, the support, and the addition of promoters. Iron (Fe) for example is one of the commercially used FT catalysts. It is of relatively low cost and has a high WGS activity; hence more suitable for lower H_2/CO ratio. In addition, it is applicable for high- (300-350 °C) as well as for low- (220-270 °C) temperature ranges. This is of advantage as at higher temperatures a shift in selectivity towards lower carbon number products (e.g. Olefins) and hydrogenated products results which is shown in (Figure 15).

A T_{high} ($\alpha \sim 0.7$)

T_{low} ($\alpha \sim 0.88 - 0.95$)

Log mole frac.

Carbon #

Low T	Sasol Arge	High T	Sasol Synthol
• low $C_1 - C_4$	13.3	• higher $C_1 - C_4$	43.0
• low $C_5 - C_{11}$	17.9	• higher $C_5 - C_{11}$	40.0
• low $C_{12}-C_{19}$	13.9	• less $C_{12}-C_{19}$	7.0
• 50-70% wax	51.7	• low wax	4.0
• 220-270°C		• 325 – 350°C	
• α: 0.87+		• α: ~0.7	
• gasoline/diesel: 1:2		• gasoline/diesel: 2:1	
• 80° Cetane #		• 50-60 Cetane #	
• 0-20 Octane #		• 0-60 Octane #	

B

Dependency of Fischer–Tropsch synthesis ASF distribution on temperature. Product selectivities (in %) of the Sasol Arge (220 °C) and Sasol Synthol (325 °C) processes are on a C atom basis. Reprinted with permission from the author.[16]

Figure 15: A) Temperature influence on production of low weight hydrocarbons, B) Schematic structure of iron particle in presence of promoters [56].

Aside from the catalyst and the FT reaction conditions as an influence on the selectivity of lower hydrocarbon production, the addition of promoters (e.g. sodium (Na), sulfur (S)) and the particle size of active metal both contribute to enhancing the selectivity [54, 57].

Accordingly, FTS for olefin production (also referred to as Fischer–tropsch to olefins process FTO) has been adopted in this research to study the catalytic performance of a surface functionalized carbon support for heterogeneous iron-based catalysts.

Chapter 3

Outline

3. Outline

In the quest for alternative sources of energy and value-added chemicals, lignocellulosic biomass and syngas catalytic conversions can provide a green source and sustainable replacement for the environmentally unfriendly and unstable fossil fuel sources. Catalysis is therefore important to achieve high conversions and productivity of chemicals and energy sources on an industrial level. Accordingly, research and industry are striving for catalysts with ever-higher catalytic performance. Besides the use of an ideal active metal, the choice of a good support is also essential with regard to achieving this goal. Carbon materials make good candidates as supports for catalysts thanks to their structural (different allotropes e.g. diamond and graphene) and physical properties (for example hardness, conductivity, thermal and chemical stability, tunable surface) which make them available for different industrial applications. Modification of carbons, in peculiar its porosity, has proven higher efficiency and better catalytic performance with the active metal. Several studies have indicated the importance of hierarchical porosity in carbons as well as several methods to the synthesis and templating of the porous carbon materials. However, the modification of the surface of carbon material with heteroatoms is not well researched and it is rarely being applied to improve the catalytic performance. Yet in regards to what is done, the results indicate an advantage in using heteroatoms within the support along to the catalyst performance in general especially in electrochemistry, but none is considering the effect of heteroatoms functionalization of the support surface on the catalytic surrounding phase.

Consequently, this thesis research investigates the effect of chemically surface modified porous carbon materials with different heteroatoms (H, O, and N) applied as supports for industrial heterogeneous catalysts, aiming for improving the knowledge of the effect of the heteroatoms, which may contribute to explaining certain catalytic behavior in previous research literatures and can lead to discoveries of new application fields. The synthesized heterogeneous catalysts with functionalized carbon supports were tested for different catalytic conversions (hydrogenolysis, oxidation, and hydrogenation reactions) in liquid and gaseous phases. The investigation takes place with nitrogen functionalized hierarchical porous (micro-meso) sugar derived carbon support compared to another similarly prepared porous carbon support material without heteroatom functionalization to particularly investigate the effect of N on the catalytic system. Moreover, the two sugar-based hierarchically porous carbons were compared to a comparably commercial hierarchical porous carbon support to highlight the porosity influence on the reaction and the catalytic performance. The reaction performed is a liquid phase hydrogenolysis

of kraft lignin into value added chemicals. One further interesting point regarding this study is the application of kraft lignin degradation in flow and batch reactors to emphasize the advantages and importance of using certain reactor concepts for such industrial reactions. The interesting effect of the N-doped carbon detected on the catalysis urged the research to proceed by functionalizing sugar- derived hierarchical porous carbon supports with other heteroatoms (H and O) along with N heteroatoms and comparing them to a non-functionalized sugar-derived porous carbon support. Liquid phase glucose oxidation reaction with gold nanoparticles was employed as the model reaction to explore the different heteroatom functionalities effect. This study clearly showed the influence of surface polarity of the supports on the size of the deposited gold nanoparticles and thus the catalytic properties. Hence the catalytic performance was obviously different for each reaction despite the use of the same metal and support source. Although both prior mentioned reactions were performed in liquid phases, yet the heteroatoms influenced the supports and thus the catalysts differently resulting with different catalytic behavior and performance. In correspondence, the investigation proceeded in the direction of applying carbon nanotube supports functionalized with the similar heteroatoms (H, N, O) for hydrocarbon formation from syngas. In particular, the target of the Fischer-Tropsch CO hydrogenation reaction is to achieve higher selectivity to short (C_2-C_4) olefin formation. As the main finding, a junction between iron particles and carbon nanotubes modified with a nitrogen-doped carbon surface layer leads to higher catalytic activity and a higher selectivity towards the desired products. A summary of the research study is given below (Figure 16).
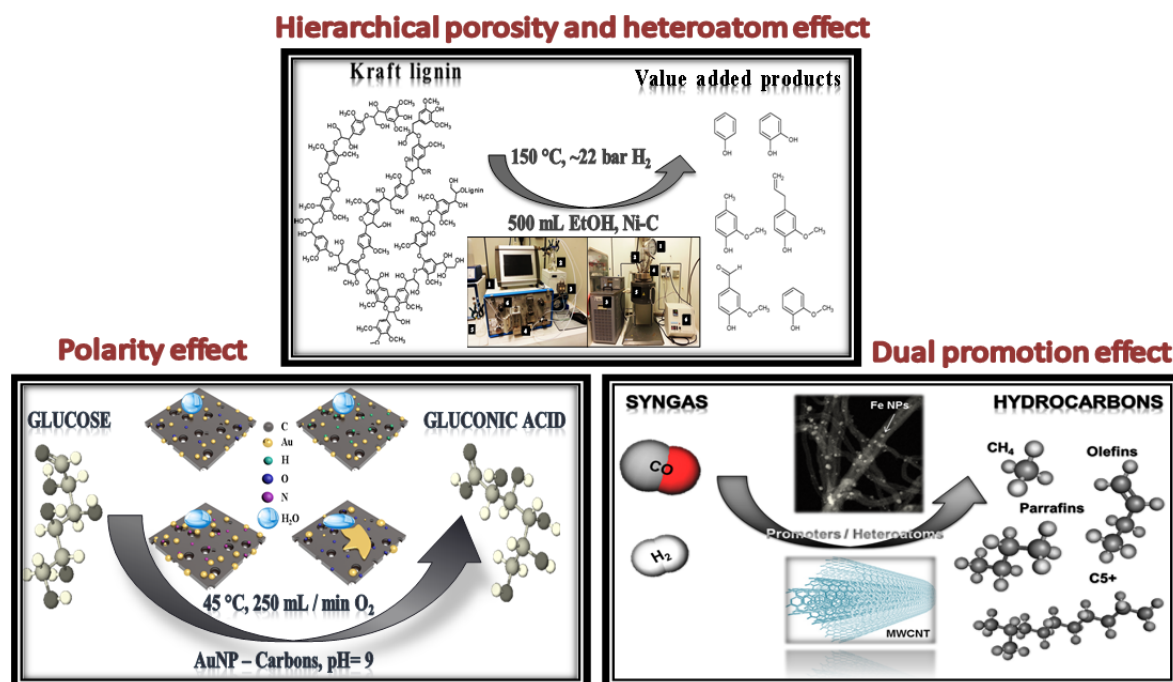

Figure 16: A summary of the investigation carried out in this thesis.

Chapter 4

Research and Outcomes

"During an intense period of lab work, the outside world vanishes and the obsession is total"
(L.M. Lederman)

Preface

This following chapter discusses the investigation made towards understanding the heteroatoms influence on the carbon support and the catalytic performance for industrial heterogeneous catalyst. The method of preparation, characterization, reaction and the results of the different reactions performed in this study are given in details. Starting from Nitrogen doped carbon (NDC) for kraft lignin hydrogenolysis, continuing to selective glucose oxidation using functionalized sugar-derived carbons and finally switching from liquid to gaseous phase reaction in a Fischer-Tropsch selective olefin hydrocarbon synthesis.

Profound perceptions are introduced regarding advancements in catalysis as well as interesting discoveries have been noted during this investigation which in turn can contribute to the progress of the effort in finding an appropriate solution to the previously discussed dilemmas (chapter 2).

4. Research and Outcomes

4.1.   Functionalized Carbons as Supports in Liquid Phase Reaction: *Nickel Nanoparticles Catalysts for Kraft Lignin Hydrogenolysis in Batch and Flow Reactions*

i. State of Art

In our everyday life, we use enormous amounts of chemicals in different applications. Chemicals are used in medicine, devices, food, buildings, cosmetics, detergents and more. They present an essential source of living. However, the increase in population results with an increase in consumption of the feedstock of these chemicals which is mainly fossil fuels. Rapid consumption of fossil fuels, economic and political dependence on other countries to obtain these fuels, environmental pollution due to industrial processing of these fuels are all reasons why it is convenient to switch to renewable sources of energy [58]. As has been discussed in (chapter 2.8.1), one of these promising sources is lignocellulosic biomass (LCB) as it is a renewable cheap source and not only capable of providing energy and biofuels, but also value-added chemicals for pharmaceutical or industrial use. Lignin (one of LCB main components) is a macro molecule of phenolic and aromatic groups, bond by C-C and ether linkages. Pulp and paper industries tend to produce large quantities (> 50 Mt/ year) of lignin after separating it from the other components of LCB via addition of acids containing sulfur; a procedure widely known as kraft process of which the resulting product is kraft lignin. The complexity of kraft lignin structure makes it an undesirable byproduct. Therefore, it is burnt as a low value fuel to produce energy and to recover any minerals. Only 2% of kraft lignin production is used commercially [47].

The abundancy of kraft lignin and its high phenolic-structure trigger the interests of scientists to investigate it for new applications. Catalytic hydrogenolysis of kraft lignin is an efficient method [59] by which valuable low molar mass building blocks can be obtained. Nickel (Ni) heterogeneous catalysts have been applied for hydrogenolysis of kraft lignin, and especially Raney-Nickel (RaNi) -which is derived from nickel-aluminum alloys- proved to be efficient for this reaction. Despite that, Ni metal is relatively lower in activity in comparison to some other metals (platinum (Pt) and ruthenium (Ru)). Yet it is more abundant, relatively cheap, and mainly selective to cleavage of ether bonds [60-63]. Degradation of kraft lignin does not only count to the

selectivity of certain bond cleavage, but also about overcoming the poisonous effect of the sulfur present in kraft lignin (1-3 wt. %) [64]. Therefore, improvement of the catalyst properties and structure (e.g. high surface area of the support, hierarchical porosity, small-sized nanoparticles of metal) is required. This can be provided by using a support material such as carbons. Carbon materials properties (as discussed in chapter 2.5.1) of high surface area and chemical inertness as well as thermally stable makes them good candidates for support application in catalysis [65-66]. Most importantly, their property of being of tunable surface allows for carbon modification as a support with different porosity and for functionalization with heteroatoms (e.g. N). The previously mentioned modifications are presented in this work to explore the heteroatom- and the hierarchical porosity effects on the catalytic performance of Ni nanoparticles deposited on modified carbon catalysts for degrading kraft lignin.

ii. *Catalytical systems*

1. *Sugar- and Sugar Amine-Derived Carbon Supports*

In order to obtain a hierarchical porous carbon material, an inorganic eutectic salt melt method is applied. In this method zinc chloride and potassium chloride are mixed with the precursor and followed by calcination at temperature 900 °C. This procedure allowed the formation of mesopores besides micropores in the carbon material; hence hierarchical porosity and provided high surface area .Moreover, sugar precursor (as glucose) is used for carbon material which is a cheap source, and decomposes at relatively low temperatures. In addition, using glucoseamine with only slight difference in chemical structure than glucose ensures the maximum possible comparability between the two formed supports.

So, the synthesis of hierarchical porous carbon supports proceeded by using glucose and glucoseamine hydrochloride as precursors to prepare unfunctionalized porous carbon support (referred to here as C) and functionalized porous carbon with nitrogen (denoted as NDC) respectively. The procedure of synthesis for these two supports is mixing potassium chloride and zinc chloride in 1:2 ratio and adding the inorganic mixture to the precursor in 1:3 ratio of precursor to the salts mixture. Later, the mixture is carbonized and converted to carbon material at heating temperature of 900 °C for 1 h dwelling at a heating rate of 2.5 K min^{-1} under N_2 atmosphere. A last step is to grind the resulting carbon and wash it with excess deionized water, then dry it in vacuum oven at 60 °C for 48 h. Along to these two in-house synthesized carbon supports, a third commercial carbon support (Vulcan® carbon) with hierarchical porosity (macro-, meso-, micropores)

is purchased (denoted here as C ref). The in-house carbon supports are compared to one another to identify the nitrogen heteroatom effect and the hierarchical porosity influence is studied by comparison with the commercial carbon support.

2. Nickel –Carbons catalysts

Afterwards, the deposition of the active metal nickel (Ni) followed. The method of deposition used was incipient wetness impregnation to provide homogeneous dispersion of particles all over the support. Nickel nitrate hexahydrate ($NiNO_3.6H_2O$) is used as Ni salt and is dissolved in distilled water (amount of solution depends on the porosity value of each support) to impregnate each of the carbon supports (C, NDC, and C $_{ref.}$) to get 32 wt.% Ni-carbon catalysts. Afterwards, the catalysts are dried overnight at 60 °C, and then reduced under 5 % H_2/Ar flow at a temperature of 450 °C for 3 h with a heating rate of 3 K min^{-1}.

A summary of the preparation method of the Ni nanoparticles catalysts is provided in (Figure 17).
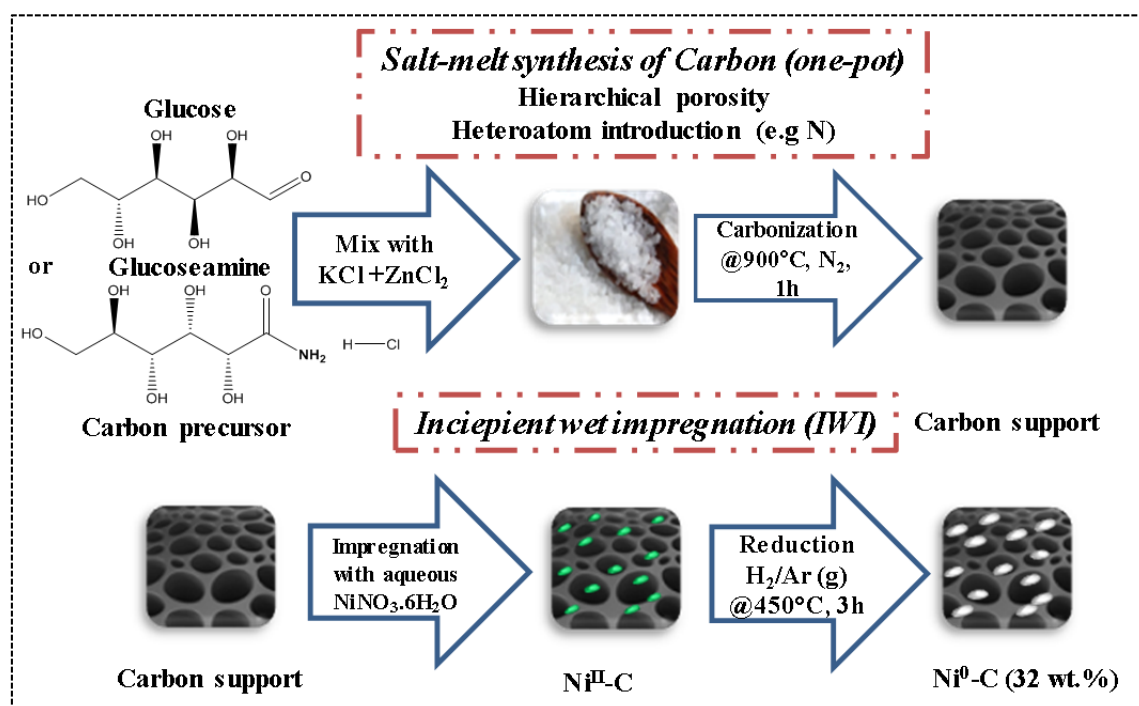

Figure 17: Schematic summary of catalyst preparation via salt-melt and IWI synthesis.

3. Scaling up catalysts

A large batch of the catalysts is successfully synthesized. However, scaling up the NDC support resulted with impurities (i.e. iron oxide denoted here as FeO) detected by x-ray powder diffraction (XRD) (Figure 18) to be an iron hematite phase (Fe_2O_3). This can happen during calcination step, which etches iron from the walls of the furnace. The supports were washed with diluted hydrogen chloride (HCl) to remove the impurity in the form of an aqueous iron chloride ($FeCl_2$) $_{aq}$. The unwashed support (NDC) contained

modest amount of FeO which after washing with 1M chloric acid (HCl) was further reduced according to the scanning electron microscopy equipped with energy dispersive x-ray spectroscopy (SEM-EDX) measurement (< 1 wt. % of Fe) and the thermogravimetric analysis (TGA) (< 4 wt. % of FeO) (Figure S. 1). However, the concentration of nickel (32 wt. %) in the catalyst prepared (Ni-NDC) is adequate to consider the low FeO concentration to be of negligible effect on the reaction.
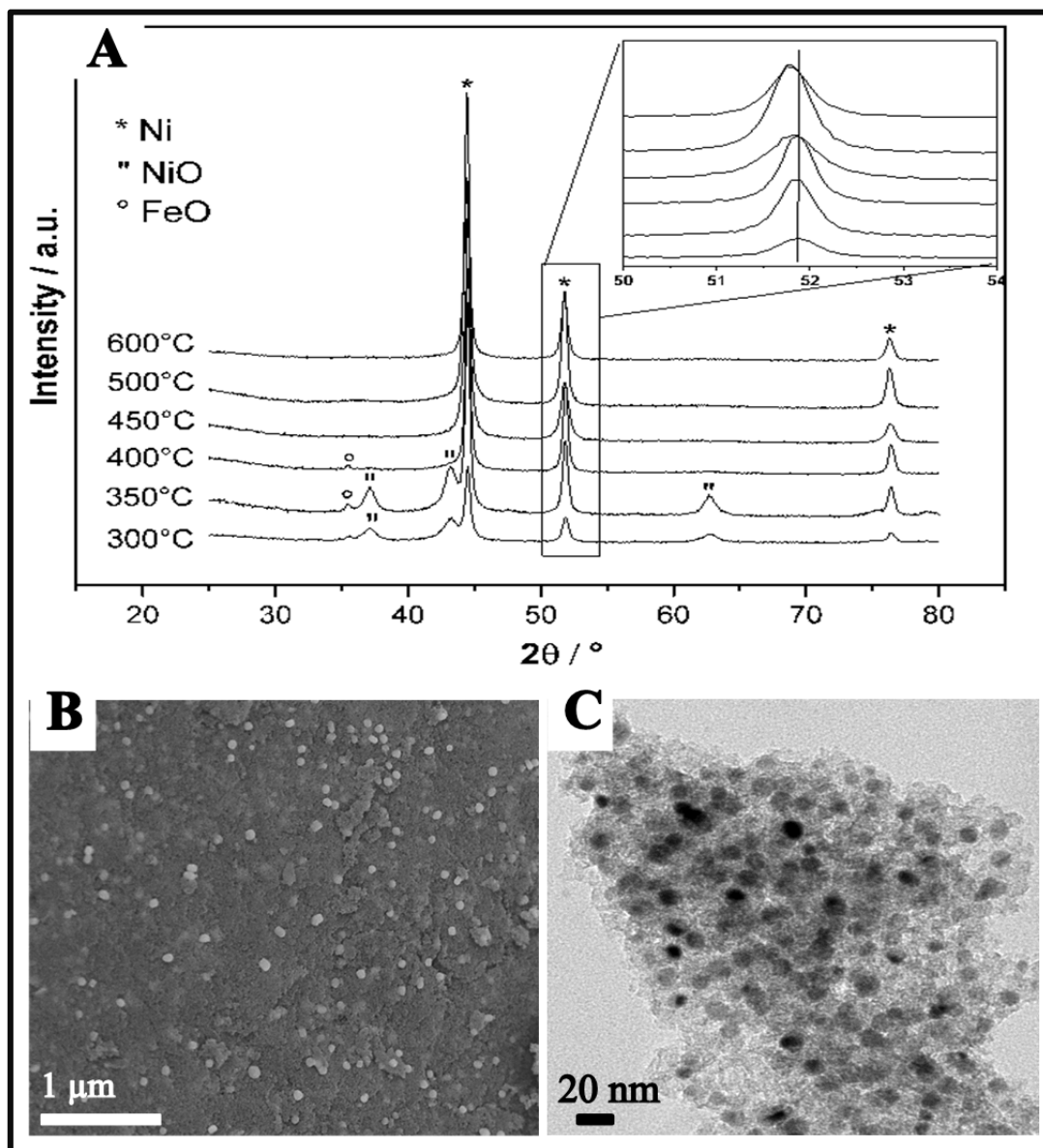

Figure 18: XRD of Ni–NDC at different temperatures (A), SEM (B) and TEM (C) images of Ni–NDC (32 wt. %).

4. Synthesis conditions of the Ni-composites

In this study variable reducing temperatures (300 °C-600 °C) and Ni concentrations (10 wt.%, 19 wt.%, and 32 wt.%) is tested before settling into the mentioned conditions of synthesis (in chapter 4.1.2.2). An interesting effect is observed which is rarely discussed in literature. The different heating temperatures led to understanding how the metal can

affect the structure of the carbon support at certain temperatures. The concentration of Ni as 32 wt. % is chosen as it allows a good distribution of particle on surface for better catalytic performance as seen by SEM (Figure S. 2) and from the XRD (Figure S. 3) analysis the temperature behavior is independent of the loading. The reduction temperature of Ni-C catalysts was considered 450 °C as it is the temperature where no nickel oxide (NiO) remains, similarly to the temperatures lower than 400 °C. At temperatures > 450 °C the reflections of the oxidized species disappear and a slight shift towards lower 2θ occurs in Ni reflections due to increase in the cell size; implying the Fe blending to Ni and forming an alloy (FeNi) highly enriched with Ni. This is detected by XRD analysis (Figure 18.A). In addition, the increase at temperatures above 500 °C, blending, and alloy formation causes reformation in the carbon support structure. The Fe and Ni active nanoparticles under high temperatures are assumed to cause dissolution in the support. The SEM images (Figure 19) reveal the changes occurring to the structure of the support at elevated temperatures in presence of Ni and Fe metals.
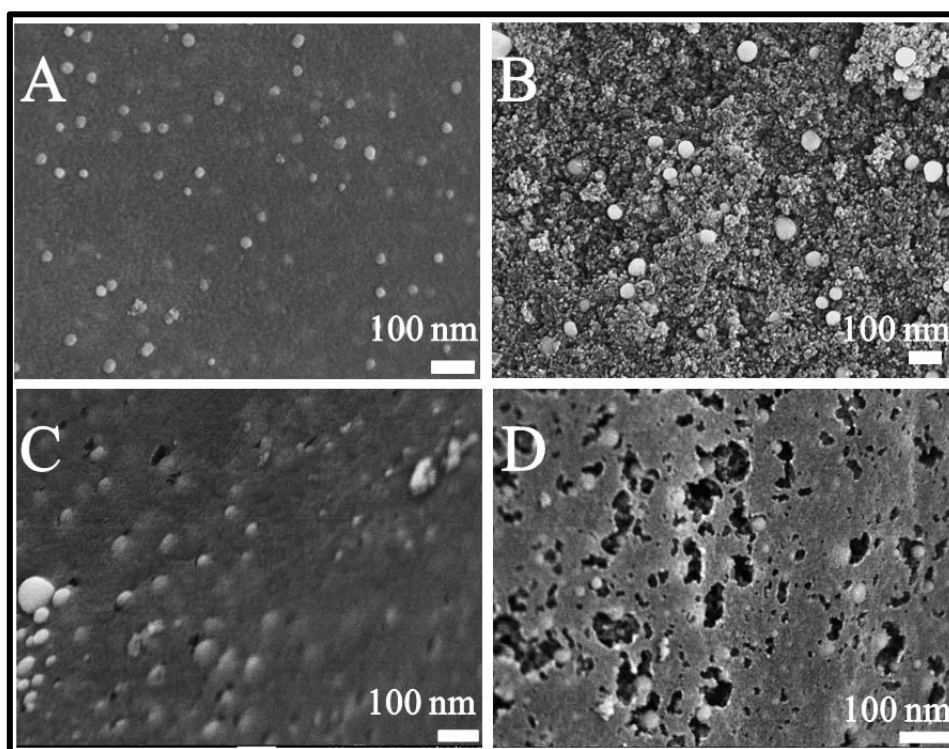

Figure 19: SEM images of Ni-NDC catalyst under different temperatures (A: 300 °C, B: 400 °C, C: 500 °C at which the etching happens, and D: 600 °C).

iii.   Analysis and discussion

After the preparation of the carbon supports and the pristine catalysts the carbon porous structure and its chemical composition is analyzed by N_2-physisorption (Figure 20) and elemental analysis (E.A.) (Table 1) respectively. The porosity data implies that the in-house prepared C-supports is relatively of high surface area (NDC: 790 m^2 g^{-1} and C:

980 m^2 g^{-1} vs. C $_{ref.}$: 305 m^2 g^{-1}) and that their physisorption properties (NDC and C) is comparable even after the deposition of Ni nanoparticles; thus these two systems can be compared to one another during reaction in terms of their porosity. Also, from the E.A. the amount of N detected in NDC support is ca. 3 wt. % and the ratio of N:C (0.04) is maintained after the deposition of Ni metal. Furthermore, the morphology and particle size distribution of the systems before and after Ni deposition is investigated via transmission electron microscopy (TEM) (Figure 18C and Figure S. 4) and SEM-EDX (Figure 18B and Figure S. 5). The morphology illustrates an amorphous support structure of each carbon material and a homogeneous distribution of the active metal all over the surface of the support with an average particle size range (21 nm – 29 nm) for pristine catalysts (Table 1). The comparable average particle size implies that any catalytic differences are a contribution of the different chemical structure (heteroatom modification and porosity) of the catalysts and not of the metal itself.
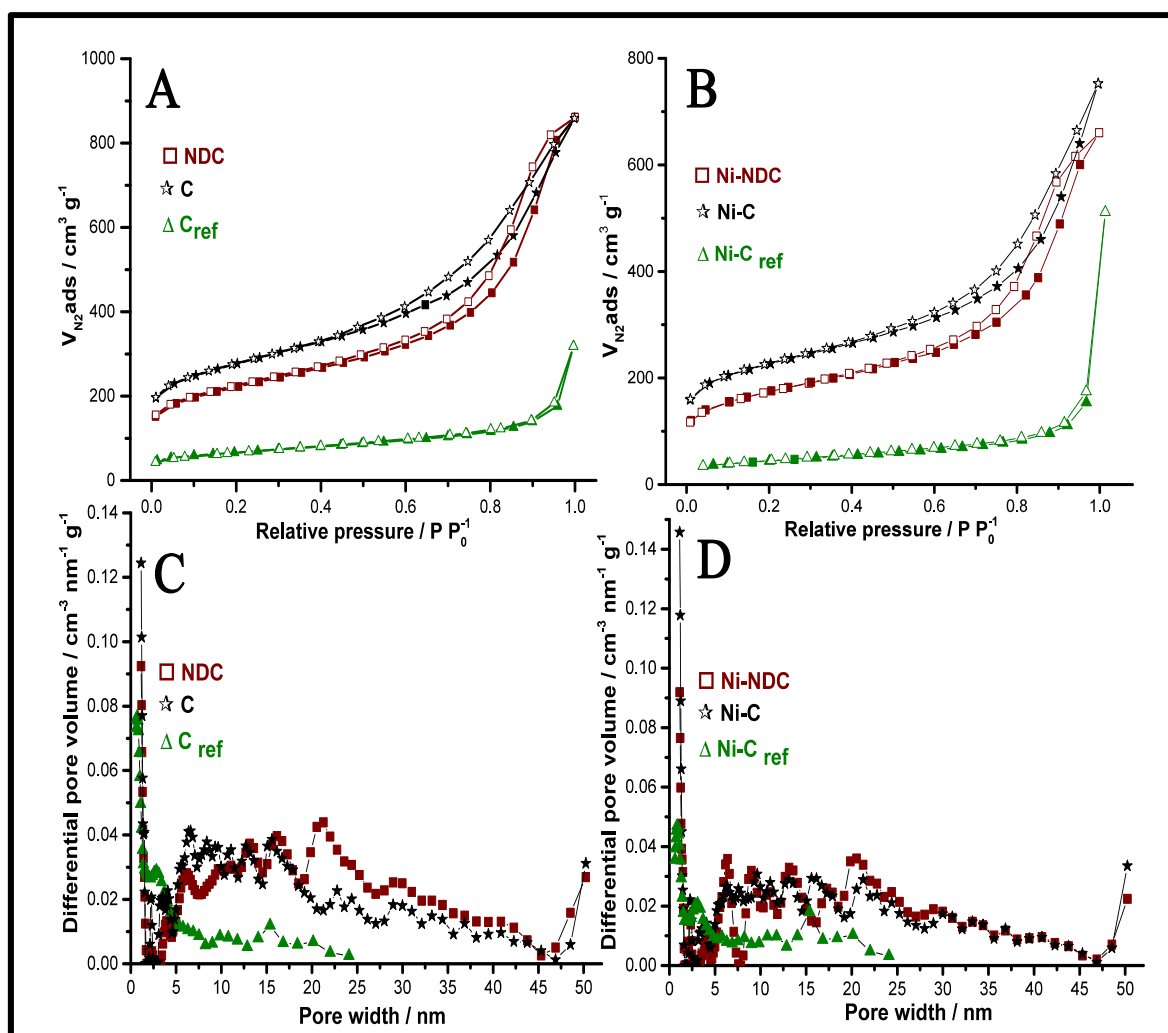

Figure 20: N$_2$-physisorption isotherms of the carbon supports (A) and Ni-C catalysts (B). Differential pore volume before (C) and after Ni deposition (D).

Table 1: Porosity, elemental analysis, av. particle size data summary of the support material and the Ni-C catalysts

	SSA (m² g⁻¹)	MPV (cm³ g⁻¹)	TPV (mL g⁻¹)	N/C (wt .%)$_{E.A}$	N:C (%)	Av. Ni particle size (nm)$_{TEM}$
NDC	790	0.16	1.3	3/80	0.04	-
C$_{ref}$	305	0.04	0.6	-/97	-	-
C	980	0.68	1.1	-/96	-	-
Ni- NDC	620	0.13	1.0	2/50	0.04	28 ± 8
Ni-C$_{ref}$	155	0.04	0.8	0.2/71	-	27± 16
Ni-C	805	0.22	1.2	1/56	-	21± 11[1]

[1] *SSA: specific surface area, MPV: Micropores volume, TPV: total pore volume*

Spectroscopic analysis followed to check the carbon structure fingerprints and to detect the phase of Ni metal in the catalysts. The sum of Raman spectra (Figure S. 7) shows the presence of D- and G- bands in comparable intensity-ratios between the different systems prepared as summarized in (Table S. 3). Also, Ni is detected between 300- 880 cm⁻¹ and the full width at half maxima (FWHM) (140-160) shows comparable structure of carbon material typical for amorphous carbon structure with slight order and aromaticity in Ni-C$_{ref.}$ catalyst and support, which is in line to HR-TEM images (Figure S. 4). Alongside, XRD measurements provided clear overview of the presence of solely reduced metallic Ni metal phases as shown in (Figure 21).
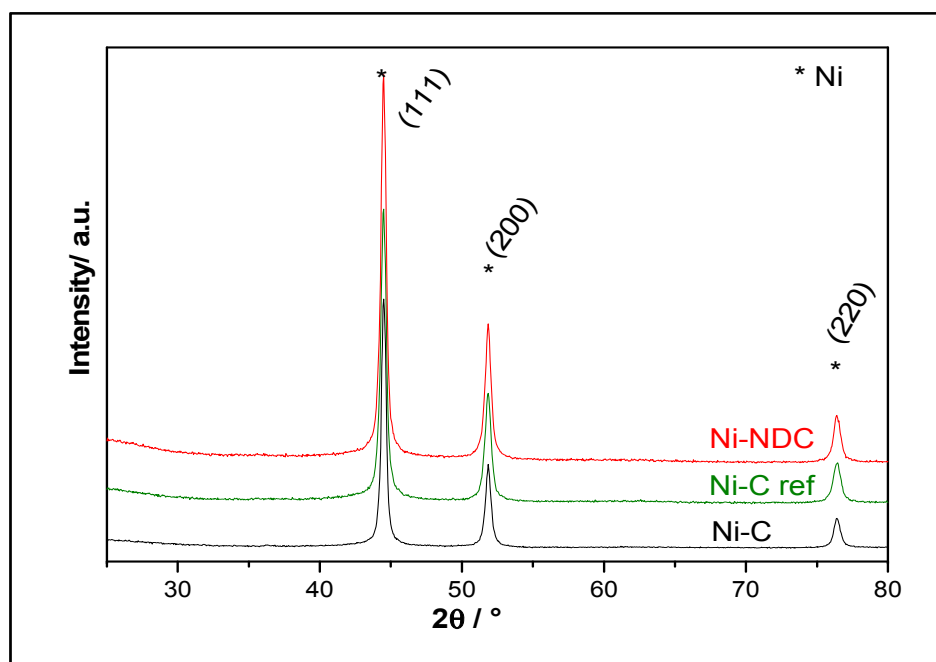

Figure 21: XRD of pristine 32 wt. % Ni-C catalysts at reducing T: 450 ° C for 3 h.

iv. Catalytic application: kraft lignin hydrogenolysis reaction

After synthesis and characterization, the catalysts are set to catalytic-experiments to value their performance in hydrogenolysis of kraft lignin. Degradation of kraft lignin is challenging. Particularly, selectivity towards the splitting of ether bonds is important to produce the desired valuable phenolic chemicals, stability towards the poisonous sulfur present in kraft lignin, and recyclability of the catalyst as discussed in the introduction part (chapter 2). Furthermore, the reaction is applied not only in a batch reactor, but also in a fixed-bed flow reactor to investigate whether the reaction system can contribute to the catalytic performance along to the catalyst properties themselves.

1. Hydrogenolysis in batch system: preparation and results

Softwood -derived kraft lignin purchased from UPM BioPiva is used to investigate the degradation in batch and flow reactions. Kraft lignin (2.5 g) dissolved in ethanol (500 mL) is loaded in a stirred autoclave with the catalyst (1 g). Then, the autoclave is sealed, purged and filled with H_2 (8 bar) at room temperature, and heated up to 150 °C where the pressure reached ~ 20 bar, while stirring for 24 h (more details and reactor description can be found in appendix Figure S. 9). After cooling the reaction, the product is filtered, the catalyst solid phase is washed with excess solvent (ethanol) for the purpose of removing any coked lignin or other products from it, and the liquid phase is further rotary-vaporized to remove the solvent and gather a concentrated product phase for analysis. A schematic summary is given in (Figure 22).
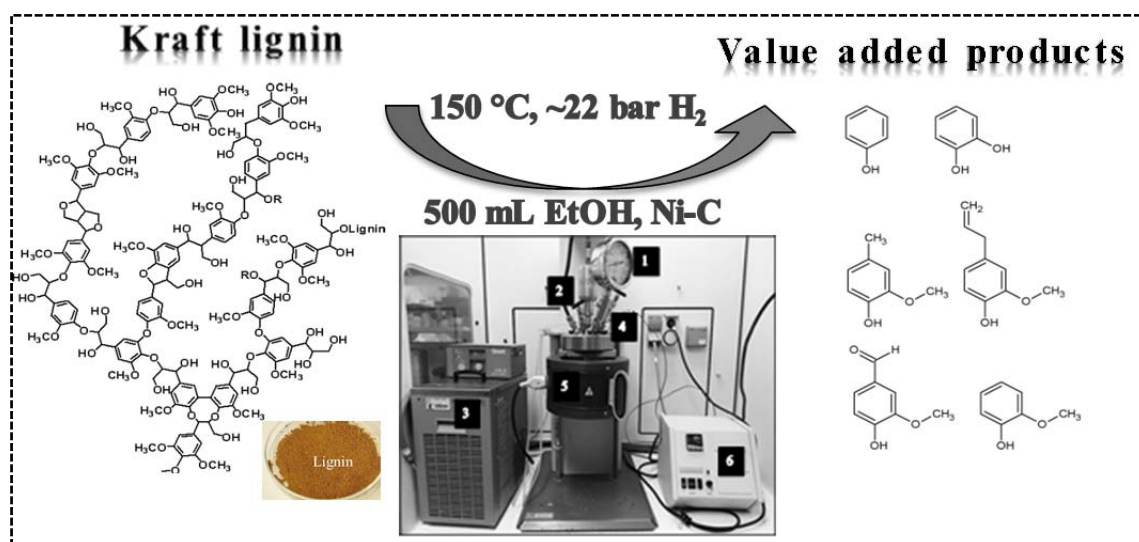

Figure 22: illustration of kraft degradation using batch reactor.

A variety of different analysis techniques is applied for product analysis to accumulate enough information to conclude on the products due to the complexity of lignin structure to analyze and understand. Applied techniques are 2D-NMR, inductively coupled plasma optical emission spectrometry (ICP-OES), gas chromatography coupled

with spectrometry (2D-GCxGC-MS and GC-FID), and gel permeation /size exclusion chromatography (GPC/ SEC). The data obtained by these techniques suggested that kraft lignin hydrogenolysis is successful and it is degraded into different phenolic groups. The 2D-NMR (Figure S. 12) showed the absence of ether linkages (β-O-4) in the batch and flow degraded product of lignin, and the formation of more aromatic groups. In agreement to that, the GPC/SEC (Table S. 11) measurement provided that the product is of lower average molar mass than the pristine kraft lignin. The composition of the batch reaction product is detected by 2D-GCxGC-MS and GC-FID (Figure 24 A-B). The 2D-GCxGC-MS measurement (applied by our collaborators in the chemistry department in the university of Serbia) provided that the dominant components are volatile 2- methoxy phenol derivatives beside cyclopentene, benzene methoxy derivatives, and bicyclic compounds, and the analysis corresponds to at least 85 wt. % of the content vaporized at 300 °C in the GC injector. A table of the detected components is summarized in the appendix (Table S. 6). The GC-FID applied to investigate the degraded kraft lignin allowed to clarify the difference between the three Ni-C composites. The salt-melt synthesized catalysts performed better than the reference catalyst (Ni-C $_{ref}$). The reason is their higher surface areas (620-805 m^2 g^{-1} vs. 155 m^2 g^{-1}) (Table 1). In addition, the reaction with Ni-NDC produced higher monomeric and dimeric compounds as well as oligomers than that with Ni-C. This effect is concluded to be the result of nitrogen in the carbon structure in Ni-NDC. This conclusion is supported by the XPS results (Figure S. 13) that shows the presence of different N-states e.g. pyrrolic, pyridinc, and graphitic of 23 at.%, 19 at.%, and 43 at.% in Ni-NDC respectively, which have contributed to improving the activity of Ni. Although via XPS no direct effect is detected of electron donating nitrogen strengthening the Ni binding to support (due to low wt.% of N), the increased electron density of active Ni sites in Ni-NDC can be an indirect proof of activity increase due to electron donating nitrogen. Supporting information given by Raman spectroscopy measurements (Figure S. 8) show the spectra for pristine Ni-NDC has Ni peak present at higher shift in comparison to Ni-C; thus the electron donating N seems to influence the Ni electronic state. Although the kraft lignin is successfully degraded and the porosity and nitrogen effects is realized experimentally, yet looking into ICP-OES results for the concentrated degraded kraft lignin product, a significant quantity of Ni (600-900 ppm) is detected indicating leaching of metal into product. Although this might refer to the filtration method where the filter paper used is a 150 mm folded filter paper, through which the catalyst might pass to the product, yet the possibility of metal leaching during

reaction cannot be ruled out. Also, the XRD of fresh and spent Ni-C catalysts for batch reaction (Figure S. 11) demonstrates that the Ni reduced state is maintained and is not oxidized or poisoned during hydrogenolysis. The recycling of the catalyst is demanding as the collected spent catalyst had increased in mass implying deposition of lignin on the surface of the support as a result of coke formation, where washing these out with common solvents failed. Hence, a large surface area range is unavailable for additional reactions as seen in the N_2-physisorption for spent catalysts (Table S. 10), where the available surface significantly dropped for all catalysts, e.g. specific surface area (SSA) for Ni-NDC fresh was 620 m^2 g^{-1} then dropped to 13 m^2 g^{-1} for Ni-NDC from batch reaction.

2. Hydrogenolysis in flow system: preparation and results

In the intentions of understanding the effect of the different systems on the catalysis reaction, the degradation of kraft lignin is applied as well in a flow reactor. The same reaction temperature was applied as with the batch reaction (T: 150 °C) and H_2 pressure of 25 bar was provided by hydrogen cells equipped in the device. The weight of the catalyst used is less than half of that for batch (350 mg) and the educt is pumped with a flow of 0.3 mL min^{-1}. These parameters are limited by the size of the cartridge and the volume of the flow reactor (~ 1 mL within 3.3 min). More details regarding the flow system are given in (Figure S. 10). An illustration of the reaction is described in (Figure 23).
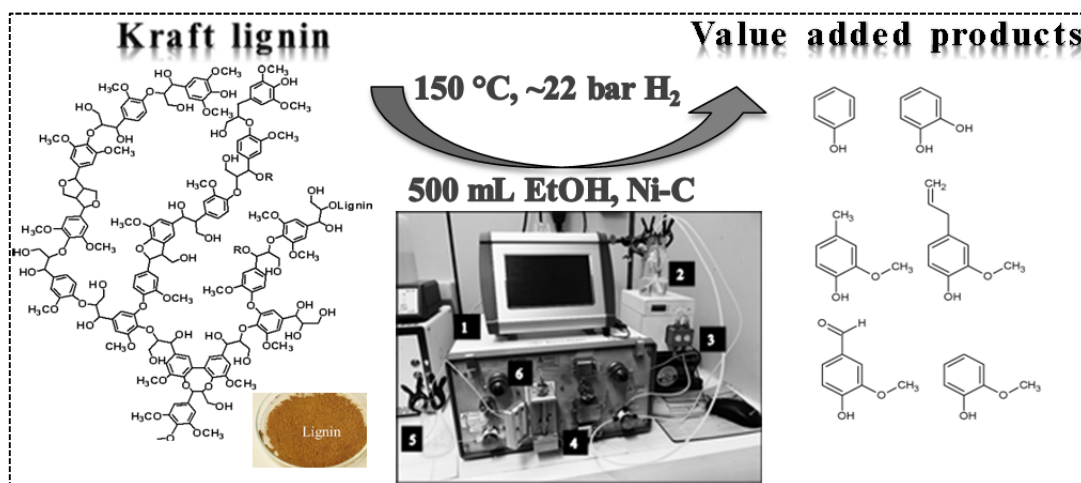

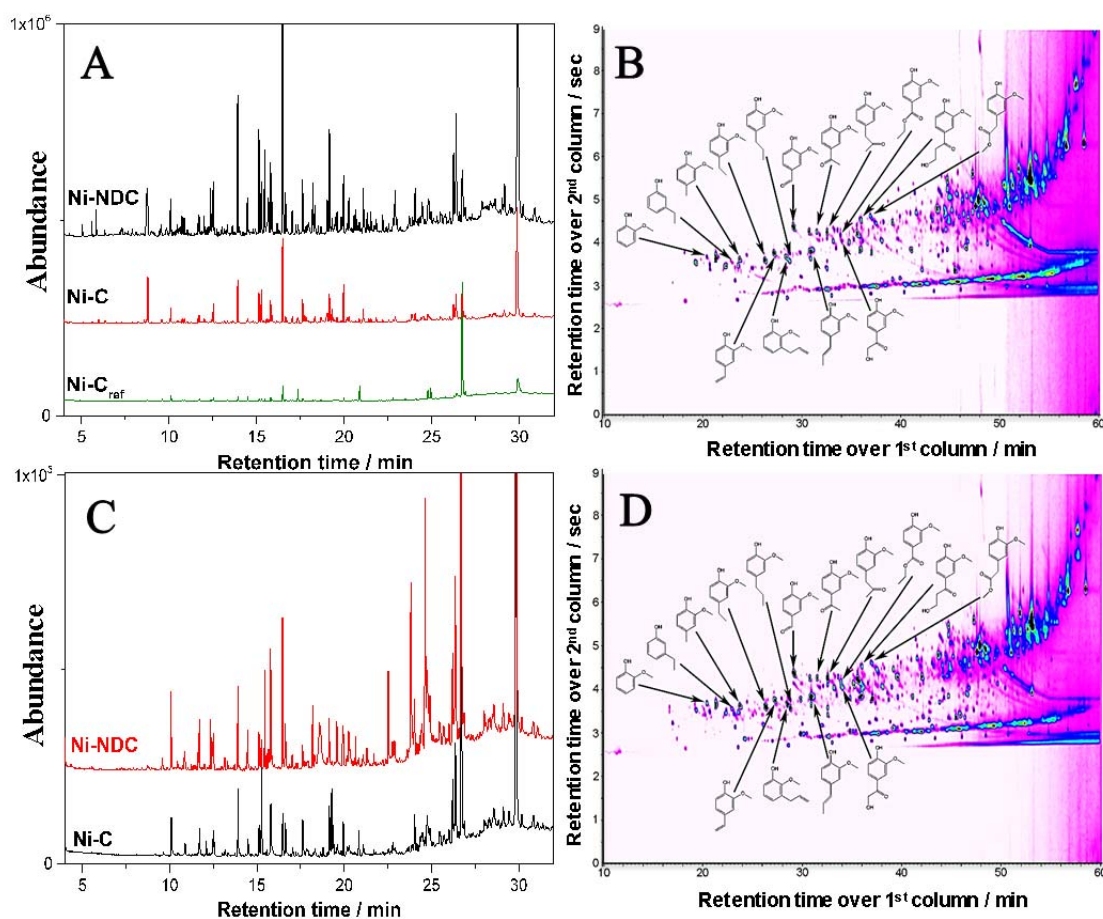*Figure 23: Illustration of kraft degradation using flow reactor.*

Figure 24: Data obtained for kraft lignin degradation by GC-FID and 2D-GCxGC-MS for batch (A and B) and flow (C and D) reactions respectively.

The same concentration of kraft lignin in ethanol (5 mg mL^{-1}) is streamed into the catalyst cartridge, degraded, and collected in a product vessel to be later rotary vaporized and concentrated for characterization. The 2D-NMR (Figure S. 12) indicates the selectivity of the catalyst towards cleavage of the ether linkages as in batch reaction. Also, the GC‑FID and the 2D GCxGC – MS results imply the presence of small molar mass molecules (Table S. 6) and the Ni‑NDC catalyst has higher abundancy of degraded lignin products compared to Ni‑C (Figure 24 C-D). Noticeable, the intensity of the signals from the products of the flow reaction compared to that of the batch reaction for Ni-NDC is higher by 2 orders of a magnitude measured via using heptane as the internal standard. The stability of Ni-NDC was retained for at least 50 h (Figure S. 14). Finally, the ICP technique detected negligible amounts of Ni leaching in degraded lignin product (~ 8 ppm) (Table S. 7), which explains the decrease in activity over time but also indicates a better control in flow reactor than in the batch. Also, after 100 h of continuous reaction an ~ 83 wt. % of the initial content of the Ni on NDC was still preserved. In contrast, Ni – NDC after the batch reaction preserved only 30 wt. % of its initial content. This decrease is a result of deposition of coked lignin on the surface of

the catalyst during reaction, causing an increase in the C value compared to that in the fresh catalyst, by that affecting the wt. % of Ni on the carbon support. This is seen less in flow reactor, because this system allows direct collection of product and shorter time contact of lignin with the catalyst compared to the batch reactor.

Furthermore, ~ 99 wt. % of degraded kraft lignin was collected when applying the two salt-melt catalysts even up to 50 h of reaction, providing less crosslinking and coking to occur due to direct separation of the product from the catalyst before potential condensation of reactive degraded lignin fragments. In addition, the flow reactor is blocked whenever applying the reaction with Ni-$C_{ref.}$ causing the device to automatically stop. The reason behind that is presumed to be the size of lignin macromolecule (3.5 nm) [67] being blocked by the micropores of Ni-$C_{ref.}$causing high back-pressure and stopping the system. Further investigation regarding this matter is not considered. This is due to the fact that this catalyst has a low surface area and performed lower than the in-house prepared catalysts in the batch reaction. Thus, implicating the importance of a higher surface area in catalysis and the effectiveness of the salt-melt synthesis compared to a commercial synthesis method.

After recovering the catalysts, N_2 – physisorption showed a decline in the SSA of Ni – NDC after 100 h reaction from 620 m^2 g^{-1} to ~ 225 m^2 g^{-1} as well in the TPV from 1.02 cm^3 to 0.42 cm^3 (Table S. 10). This decrease occurs from sorption of degraded molecules in the pore system of the support. Once saturated and filled no further decrease in SSA can be reached even after 100 h.

The hydrogenolysis of kraft lignin in both batch and flow reactions formed a majority of 2 – Methoxy phenol derivatives such as guaiacols, benzene methoxy derivatives and bicyclic compounds (Table S. 6). Among the resultant phenols, especially guaiacols, are in dominance of the products as the origin of the used kraft lignin is softwood lignin which guaiacyl units are its essential constituent along to syringol and hydroxyl phenols.

v. Summary and conclusion

In desire to contribute to the development of an industrial heterogeneous catalyst for production of value-added chemicals, a hierarchical porous carbon support modified with nitrogen heteroatom is synthesized. Ni nanoparticles are deposited on it and the resulting catalyst is investigated for the hydrogenolysis of kraft lignin.

The hydrogenolysis of kraft lignin is a process of added value due to the difference in price of kraft lignin (cheap and abundant) to the obtained phenols and molecules from lignin degradation, aside from the important products formed that can be used as

valuable chemicals and fuels. Therefore, lignin degradation is considered as a model reaction.

Knowing that Ni metal is selective to the cleavage of ether linkages and thus active for lignin hydrogenolysis, it was used as the active metal. The carbon supports have high surface area, are thermally stable, and convenient to retrieve the metal thus good for recyclation. A salt–melt synthesis method is used to prepare the carbon support of sugar source (glucose and glucoseamine) to provide the hierarchical porosity and the functionality (e.g. N) in one pot synthesis. Based on that, three Ni – C catalysts are prepared. Ni–NDC prepared from glucoseamine and Ni–C prepared from glucose are synthesized and compared to a Ni–C $_{ref}$ prepared from a commercial Vulcan$^{®}$ carbon. The main aim is to understand the effect of the heteroatom on the metal activity, selectivity and stability and to provide a deeper insight about the influence of the reactor (continuous flow system vs. a batch autoclave system) on the catalytic performance.

The kraft lignin degradation is successful in both reactors and showed selectivity towards the cleavage of the ether bonds (β–O–4 linkages) as observed via 2D–NMR, 2D GCxGC–MS, and GC–FID. A clear variation in the performance results of each catalyst is also observed. Ni–NDC is of the highest performance in comparison to the other prepared catalysts (Ni-C and Ni-C$_{ref.}$). According to the several analysis techniques applied to study the catalysts before and after flow and batch reaction, the hierarchical porous salt-melt synthesized catalysts (Ni-NDC and Ni–C) performed significantly better than a commercial catalyst (Ni–C $_{ref}$) due to their higher surface areas. Moreover, the nitrogen heteroatoms influencing the activity of the Ni metal is detected via XPS and observed via the quantification of the spectra of GC–FID for degraded lignin where Ni–NDC performed the highest signal magnitude (abundant degraded lignin products) among the applied catalysts. In addition, considering the batch and the flow reactions, the results of the quantification of the product and the catalytic performance of the Ni–NDC catalyst provide that continuous flow reaction is more convenient. The reason derives from the stability of Ni–NDC activity up to 50 h and its production of similar phenolic molecules as in the batch reaction, but in a higher signal magnitude of 2 orders. Moreover, the catalyst could maintain its structural surface properties intact for up to 50 h before charring or crosslinking took place which was in very low amounts at up to 100 h reaction. Finally, the conversion of kraft lignin was ~ 99 wt. % in the flow reaction.

Despite the efficiency of Ni–NDC catalyst in degrading kraft lignin macromolecule in presence of only ~ 3 wt. % N, and not get deactivated by sulfur, its ease of preparation

and relatively cheap to synthesize, the products of kraft lignin degradation showed the presence of Ni leaching whether in flow or batch reactions. Hence, an optimization of the catalyst by reducing the active metal wt. %, improving the N wt. % or doping different heteroatoms is recommended for clearer and deeper understanding of the effects. A depiction summarizing the idea of this research project is given in (Scheme 2).
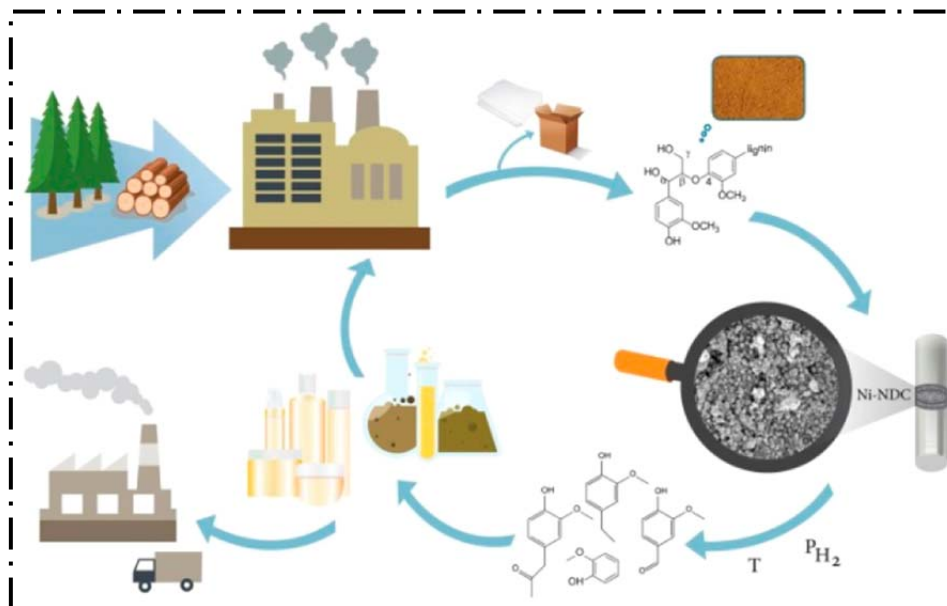
Scheme 2: A depiction of kraft lignin catalytic degradation for production of value added chemicals.

4.2.   Functionalized Carbons as Supports in Aqueous Phase Reaction: *Gold Nanoparticles Catalysts for Selective Glucose Oxidation*

i.   Preface

As the influence of the nitrogen modification of the carbon support is observed qualitatively but not strongly detected, further investigation is required. Hence, research proceeded by investigating the functionalization of the sugar-carbon salt melt support with different heteroatoms. This time gold deposited on carbon (Au–C) composites are synthesized for selective glucose oxidation to gluconic acid in an aqueous phase reaction (APR). The focus this time is to determine the influence of the heteroatoms on the catalytic performance (activity, selectivity, and stability) in correlation to another reaction type (in this case an oxidation reaction), but still in a liquid (aqueous) phase reaction.

ii.   *State of art*

Sugar–derived salt–melt carbon materials used as supports has many advantageous properties, as mentioned in prior chapters, upon them the ability to tune their atomic structure. The addition of heteroatoms or functional groups alters the surface and the electronic properties of the carbons in particular and the catalytical performance in general as can be concluded from (chapter 4.1)[68]. The doping of heteroatoms not only influences the support or the metal and thus the catalytic performance, but it impacts the interaction between the catalyst and the surrounding phase as well. The presence of oxygen-functional groups such as carboxyl groups on the surface of the support for example alters the tendency of the active metal to oxidize. It can also adjust the growth of the metal particle size which is a known anchoring effect widely studied. Usually such interaction is related to porosity effect, metal loading, or particle size, however less is known about heteroatoms influencing the interaction with the surrounding phase [69-70].

In order to investigate that, modification of sugar–derived salt–melt carbon supports with variable heteroatoms (O, N, and H) was carried out. Then a catalyst system was prepared via deposition of gold (Au) on these supports to end up with Au–$C_{Glucose}$–O, Au– $C_{Glucose}$–H, Au–$C_{Glucoseamine}$, and Au–$C_{Glucose}$, for comparison between heteroatom doped versus heteroatom-free systems. As all catalysts synthesized of the same carbon source (glucose) except Au–$C_{Glucoseamine}$ (glucoseamine precursor) which is comparable in properties to Carbon from glucose according to (chapter 4.1.2), their carbon structure is of similar porosity structure and the resultant of any difference would be of the modification with the particular heteroatoms applied. The catalysts were used in the liquid phase oxidation reaction of D-Glucose to D–gluconic acid in presence of oxygen flow as oxidizing agent. This reaction has been chosen as a model reaction as it has already been extensively used for investigating gold catalysts in liquid phase and thus reference data is widely available [49, 71-74]. Moreover, the reaction was investigated for economic reasons, because a large amount of gluconic acid of ~ 100000 t is annually produced [75] and used as additives in food, pharmaceutical products, textiles, and in constructions industry. Currently, it is manufactured by biotechnological processes where fermentation is taking place [75-77]. However, gold catalysts show a promising alternative source in means of reaction rate and high space time yield for gluconic acid production (as given in Figure 25) [78].
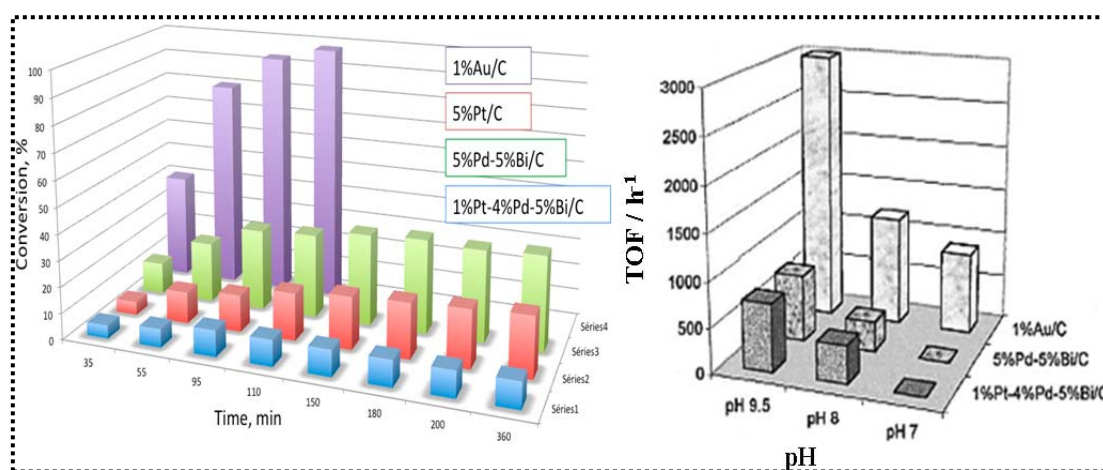
Figure 25: The conversion of glucose by different metal nanoparticles [79] and the activity as a measure of TOF. [78]

Furthermore, hydrogen peroxide (H_2O_2) can be used as oxidizing agent for the reaction rather than molecular oxygen flow, but it decomposes in alkaline medium and as a commercial product it contains side products e.g. glycerol used to stabilize the H_2O_2 from decomposition which might influence the reaction.

The oxidation of glucose to gluconic acid in presence of a heterogeneous catalyst is proposed to proceed through an Eley–Rideal mechanism [78, 80]. In this mechanism, the surface of the catalyst adsorbs the molecular oxygen which would interact with glucose molecules in the liquid phase and convert/ oxidize the glucose molecules to gluconic acid. In general, the catalytic performance is measured as a function of the Au deposition method, the structural properties of the support, and the reaction conditions. The influence of heteroatoms on a catalyst and the catalytic properties remains seldom investigated. As a result, the relation of carbon surface structure with the catalytic properties is studied with focus on the effect of the heteroatoms.

iii. Catalytical systems

1. Heteroatom Modification of Sugar–Derived Salt–Melt Carbon Supports

In consequence, sugar–derived hierarchically porous salt–melt carbon support was synthesized and modified with three different heteroatoms (O, H, and N). Similar to the synthesis in Ch.4.1.2, a scaled–up mixture of glucose and salts ($ZnCl_2$ and KCl) in 1:3 ratio respectively was carbonized at 900 °C under N_2 flow then washed with excess of distilled water (D. W.) to remove any remaining salt. Afterwards, part of the carbon (denoted here as $C_{Glucose}$) was heated using the muffle furnace at 400 °C for 1h in air to obtain ($C_{Glucose}$–O). Another part was treated in a tubular furnace under H_2/Ar flow at 600 °C for 2 h with a heating rate of 20 K/min producing by that ($C_{Glucose}$–H). In

addition, to obtain a nitrogen doped carbon glucoseamine was used as precursor and similarly to ($C_{Glucose}$) it was synthesized as described in Ch.4.1.2 and denoted as ($C_{Glucoseamine}$).

2. Gold – Carbon catalysts

Synthesis of gold–carbon catalysts was based on colloidal gold nanoparticle deposition method that provides particle sizes less than 5 nm to exhibit high catalytic activity. Furthermore, the method does not require an additional temperature treatment due to the use of pre-reduced gold nanoparticles (Au NPs) and provides homogeneous dispersion of the particles over the support. A 500 mL of distilled water (D.W.) was mixed with 29 mL of 0.2 wt.% gold precursor tetra–chloro auric acid salt ($HAuCl_4.3H_2O$ (49 % Au)) while stirring. Then, 11.6 mL of 1 wt. % aqueous sodium citrate (the gold stabilizing ligand) was added. After 30 s, 5.80 mL of cooled sodium borohydride mixture was added as the reducing agent (85 mg of $NaBH_4$ in 50 mL of ice-cooled 1 wt. % sodium citrate solution in water). Then the color of the dispersion immediately turned to wine–red color. Afterwards, each of the previously prepared carbon supports were immersed into a defined volume of the synthesized colloidal Au NPs solution to obtain 1 wt. % Au – C catalysts. The carbon – gold solution mixture was sonicated for 2 h, then separated via centrifugation (4000 rpm · 20 min $^{-1}$) and dried in vacuum oven overnight at 80 °C (Figure 26).
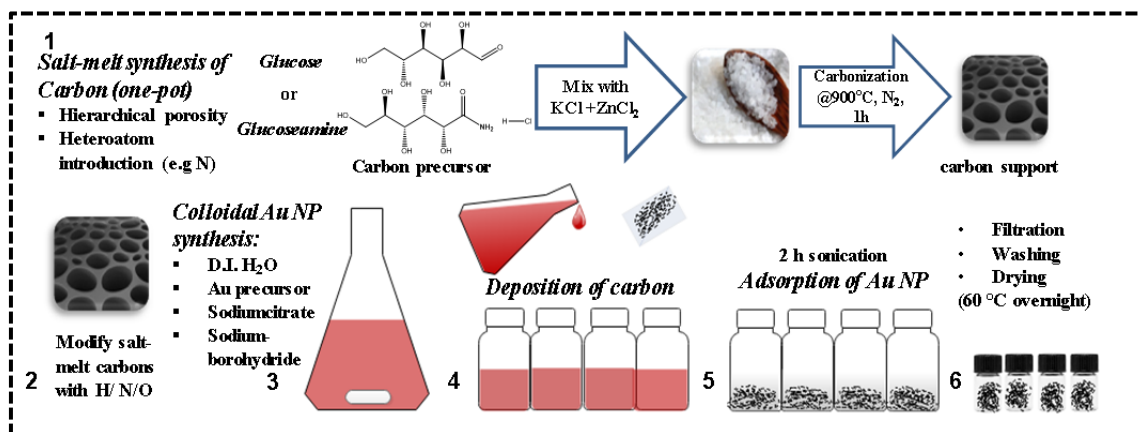

Figure 26: Illustration of synthesis of gold nanoparticle carbon catalysts.

iv. Analysis and discussion

In order to investigate the effect of heteroatoms on the catalyst properties and the catalytic reaction, four catalysts were prepared with gold deposited on surface modified carbon supports (Au–$C_{Glucose}$–O, Au– $C_{Glucose}$–H, Au–$C_{Glucoseamine}$, and Au–$C_{Glucose}$). Prior to applying them in a reaction to study the effect on the catalytic performance, these pristine catalysts were characterized using several methods. Elemental analysis

(E.A.) data (in Table 2) revealed that $C_{Glucose}$–O has higher content of oxygen compared to unmodified $C_{Glucose}$ meaning the treatment under air for the introduction of oxygen surface groups at 400 °C was successful. The $C_{Glucose}$–H support has slightly reduced oxygen content as compared to unmodified $C_{Glucose}$. Significant oxygen content is detected in $C_{Glucose}$–H and $C_{Glucose}$, keeping in mind that porous carbon supports adsorb molecules from the surroundings (e.g. water, carbon dioxide) which can influence the measurement. In the case of Nitrogen heteroatoms modification, $C_{Glucoseamine}$ support contained ~ 3 wt. % nitrogen (in consistency with NDC support previously mentioned in CH. 4.1.2) and no significant nitrogen content was detected in the other supports. The presence of nitrogen in $C_{Glucoseamine}$ material detected by E. A. has been supported by XPS measurements (Table 3). It is also noticeable that oxygen content of $C_{Glucoseamine}$ is higher than $C_{Glucose}$. This result introduces the idea that the polarity (hydrophilicity and hydrophobicity) of the surface structure of $C_{Glucoseamine}$ and $C_{Glucose}$–O is high, and is behind the increase in the oxygen content in these two carbons (more water from surroundings is adsorbed). Even after the deposition of Au NPs to the carbon supports, where the formation of Au NPs was in liquid phase, the E.A. for the catalysts reveal similar trends of elemental content to those of the supports; thus the metal deposition has no major influence on the surface modification of the carbon supports. Thermogravimetric analysis has been applied (under He atmosphere) as well to check the different surface structures of the prepared catalysts (Figure S.20). The results show Au–$C_{Glucose}$–H has the lowest weight loss as the oxygen groups that are present in the system were removed. Au–$C_{Glucoseamine}$ and Au–$C_{Glucose}$–O have high number of surface groups as also detected by E.A; thus they have higher weight loss. The mass lost during TGA measurement for these catalysts up to 100 °C is due to water evaporation which is especially in the catalysts modified with nitrogen and oxygen groups as stated prior in the E.A. data discussion.

Table 2:N_2-physisorption and E.A. data summary of carbon supports and Au − C catalysts

Support/ Catalyst	SSA ($m^2 \cdot g^{-1}$)	TPV ($cm^3 \cdot g^{-1}$)	MPV ($cm^3 \cdot g^{-1}$)	C/N/H/O (wt%)$_{EA}$
$C_{Glucose}$	705	0.62	0.18	86/0.2/1.3/12
$C_{Glucose}$-O	1032	1.10	0.28	70/0.2/2/26
$C_{Glucose}$-H	904	0.93	0.25	87/0.2/1.3/10
$C_{Glucosamine}$	807	1.26	0.16	73/3/2/22
Au-$C_{Glucose}$	559	0.98	0.09	89/0.4/1.4/9
Au-$C_{Glucose}$-O	926	0.78	0.28	75/0.2/2/22
Au-$C_{Glucose}$-H	935	1.02	0.26	93/0.3/2/4
Au-$C_{Glucosamine}$	812	1.22	0.16	76/3/2/19

According to the N_2 physisorption results of the supports (Figure 27 A and C), the isotherms illustrate the high nitrogen uptake at low relative pressure and the hysteresis loop at $P \cdot P_o^{-1} > 0.8$. The quenched solid state density functional theory (QSDFT) was applied to analyze the pore size distribution (Figure 27 C) and a broad distribution of micro– to meso– pores of different sizes exist. The SSA for these carbon supports is between $700 - 1000$ $m^2 \cdot g^{-1}$ and the total pore volume (TPV) up to 50 nm is between $0.6 - 1.26$ $cm^3 \cdot g^{-1}$ (Table 2). In the case of micropores, $C_{Glucose}$–H and $C_{Glucose}$–O (0.25 $cm^3 \cdot g^{-1}$ and 0.28 $cm^3 \cdot g^{-1}$ respectively) contain higher micropores than the two others. despite these slight differences, the pore structure for the supports stay comparable. TEM imaging for the carbon supports illustrate the homogeneous mesopore carbon structure (Figure S.21) independent of the surface chemistry.

Similarly, Au–C catalysts have been analyzed by N_2– physisorption, and their isotherms indicated no significant difference than the supports, meaning the mesopore carbon structure remained unaffected by the Au NPs. Similarly, the micropore volume for the Au–C catalysts didn't differ much compared to the carbons, except for Au–$C_{Glucose}$ which had a slight decrease likely due to clogging of small pores by small particles in the catalysts.

The modification of the support material with heteroatoms can influence the polarity (hydrophilicity or hydrophobicity) of the material and thus will affect the interaction of the catalyst while synthesis or in a reaction. Therefore, water physisorption of supports and catalysts was tested at 25 °C. The isotherms (Figure 27 E and F) clearly state the $C_{Glucoseamine}$ and $C_{Glucose}$–O are more hydrophilic than $C_{Glucose}$–H and $C_{Glucose}$. The water adsorption analysis is an indicator for the strength of the water–surface interaction. This interaction strength in these carbon supports is determined according to their pore size and the density of the heteroatom groups present on the surface of the carbon. Considering the comparable pore size distribution of the supports the lower pressure for water to bind with the surface of the support indicates more hydrophilic properties of $C_{Glucoseamine}$ and $C_{Glucose}$–O. Also, after the metal loading to the support similar trend of water adsorption isotherm is observed. Interestingly, the water adsorption isotherms for the Au–C catalysts can be comparable in shape and water uptake to their pristine supports, except for Au–$C_{Glucose}$–O which has a distinctive high water uptake of $0.5 - 0.9$ $P.P_o^{-1}$. This attributes to the stronger surface attraction to water adsorption after metal deposition. The water adsorption measurement provided sufficient information regarding the surface wetting and dispersability in water for the salt–melt carbons as well as for the catalyst synthesis and catalytic reaction in aqueous solution.

The morphology of the Au–C catalysts as investigated by TEM (Figure 28, Figure S. 22, Table 3) shows well distributed Au NPs on the surface of the least hydrophilic $C_{Glucose}$–H and $C_{Glucose}$. The particle size for Au–$C_{Glucose}$ is smaller and has narrower distribution (3.4 ± 1.1 nm) compared to the Au– $C_{Glucose}$–H (4.4 ± 2.4 nm). In contrast, larger particle sizes are obtained for the hydrophilic Au–$C_{Glucoseamine}$ (6.8 ± 2.4 nm) and Au–$C_{Glucose}$–O (4.4 ± 2.4 nm). Upon all the Au–C catalysts prepared, TEM for Au–$C_{Glucose}$–O reveals the presence of large agglomerates of Au particles and only a small fraction of the metal is in sizes < 10 nm (Figure 28 C vs. Figure S. 22 C). In conclusion, the surface wetting of the more hydrophilic carbon supports appears to lead to different kinetics of ligand exchange around Au NPs from the citrate stabilizer to the carbon support, resulting in larger Au particles deposition.
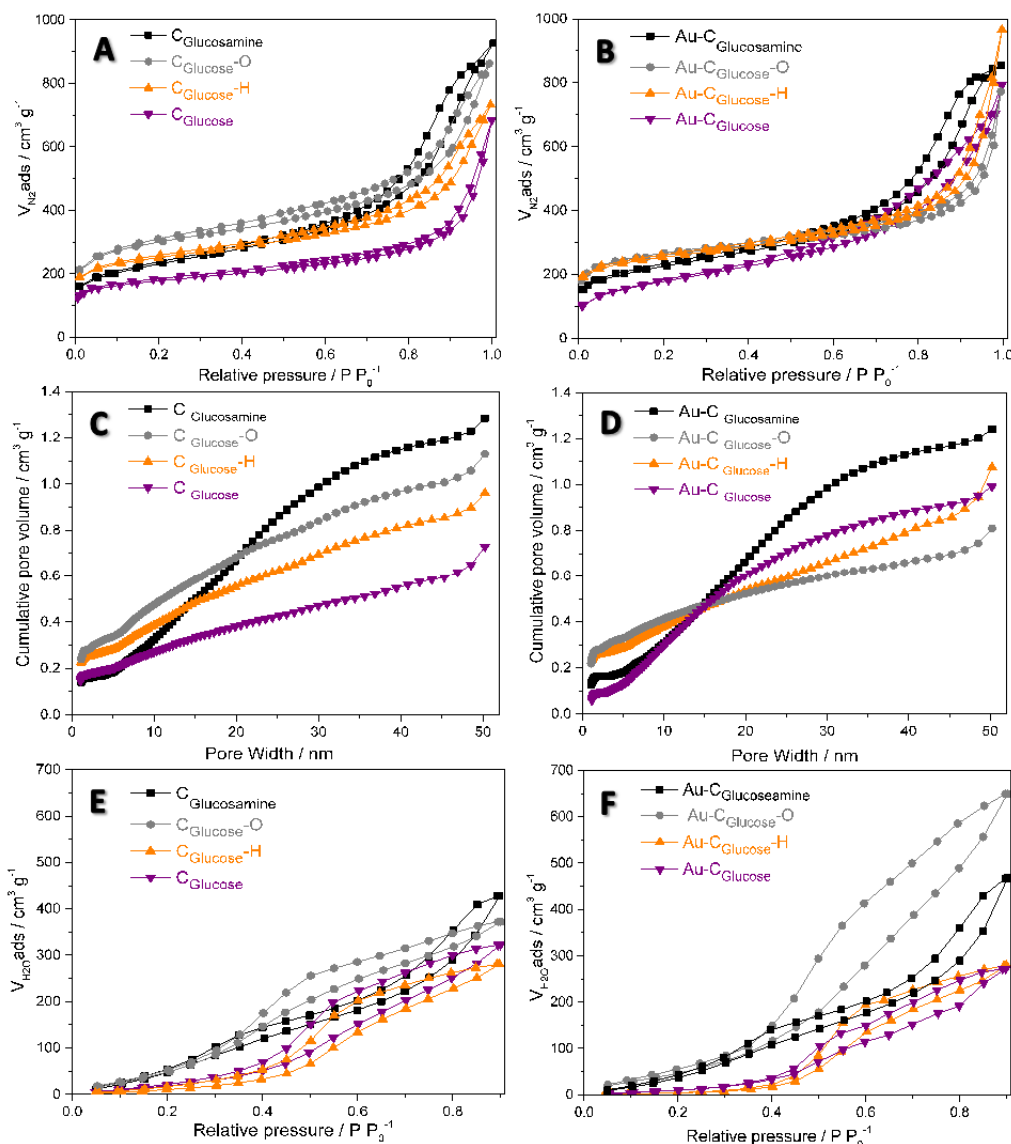
Figure 27: Nitrogen physisorption isotherms (A,B) with corresponding cumulative pore size distributions (C,D) and water vapour physisorption isotherms (E,F) of the catalyst supports (A,C,E) as well as the Au–C catalysts (B,D,F).
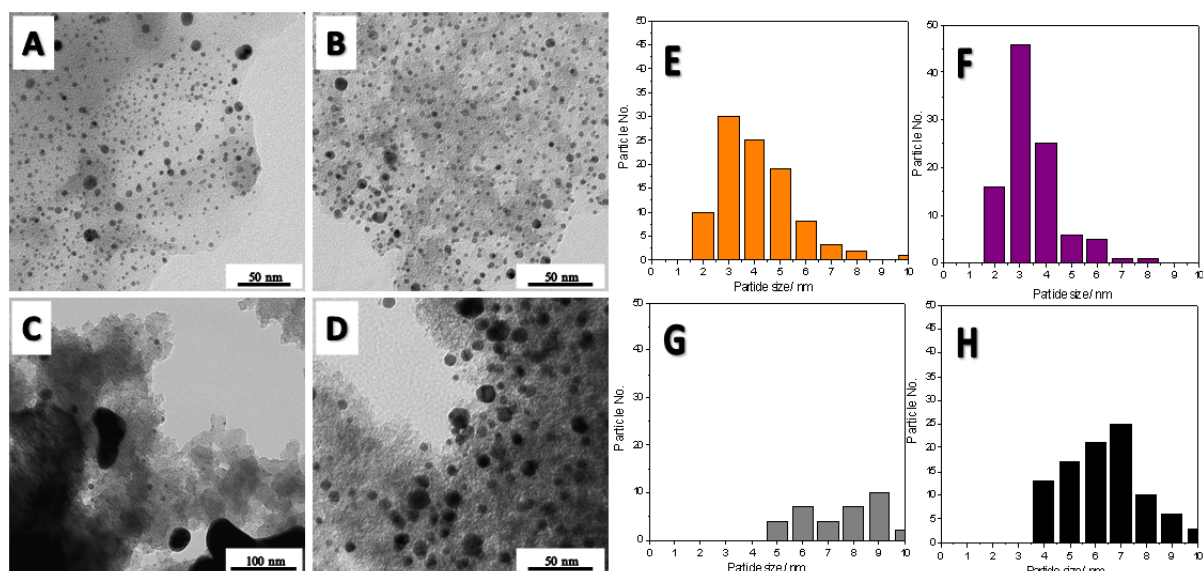
Figure 28: TEM images (A-D) and corresponding Au NP size distributions up to 10 nm (E-H) of Au-$C_{Glucose}$-H (A,E), Au-$C_{Glucose}$ (B,F), Au-$C_{Glucose}$-O (C,G), and Au-$C_{Glucosamine}$ (D,H).

The Au particles size and distribution was also supported by the XRD patterns (Figure 29) of the catalysts, in which Au–$C_{Glucose}$–O show sharper peaks originating from agglomerated Au metal. The presence of broadened peaks is observed for the rest of the catalysts which is caused by the nanoparticle sized metal on support. Another point to clarify, the peaks present in Au–$C_{Glucoseamine}$ XRD pattern between 32 ° and 37 ° belong to the iron oxide which results during calcination in the oven as explained in Ch. 4.1.2.3 and contributes to the increase of oxygen content in $C_{Glucoseamine}$ support as seen from E.A. Along to investigating the particle distribution and size with TEM and XRD, the gold content of the catalysts was inspected by ICP–OES (Table 3). The Au–$C_{Glucoseamine}$ contains 0.7 wt. % of Au in comparison to 0.4 wt. % present in the rest of the catalysts, referring to high adsorption of water in support before Au NP deposition.
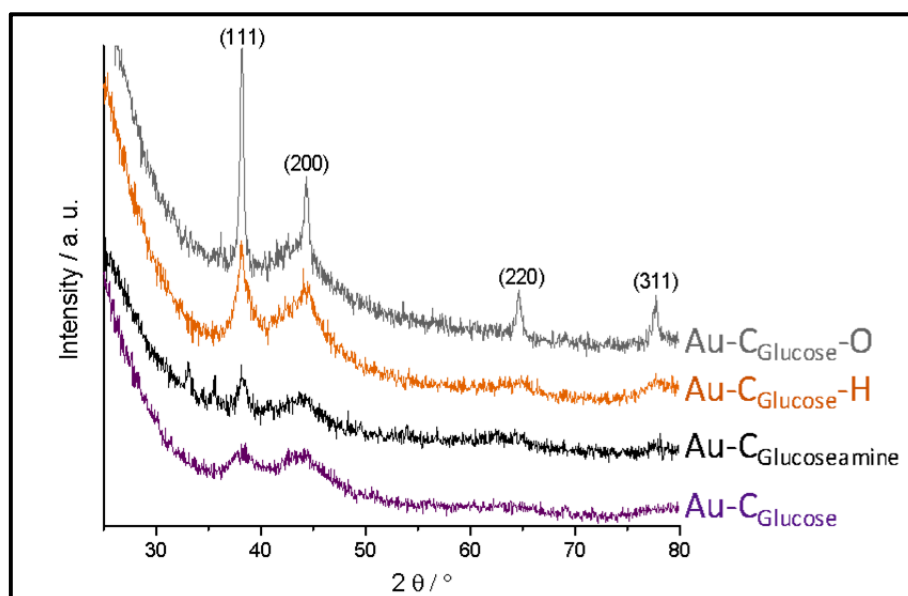
Figure 29: XRD patterns of the Au-$C_{Glucose}$, Au-$C_{Glucose}$ -H, Au-$C_{Glucosamine}$, and Au-$C_{Glucose}$-O catalysts.

Another analysis method applied is XPS for the Au–C catalysts illustrates the gold content on the particle ranging between 0.4 – 2.7 atom % (Table 3, Figure S. 23, Figure S. 24). Comparing the value of XPS with those of ICP indicates the presence of the Au particles mainly on the external surface of the support, or in other words, the particles are not entering the internal porosity of the carbon particles when depositing from the aqueous solution. The XPS scans reveal the presence of Au 4f peaks that are comparable for all catalysts. The Au 4f signal shows a doublet for the metallic gold at binding energy of ~ 84 and ~87.5 e.V and no oxidized state of Au was detected in agreement with the XRD study.

Out of these analyses, the presence of different surface chemistries leads to compelling changes in the catalysts structure after Au NP deposition. This means the catalytic properties will be influenced by the particle size, surface properties of support, and reduced state of gold metal.

Table 3: XPS and ICP data summary, average particle sizes before and after (given in brackets) glucose oxidation reaction, and gold-specific activity (expressed as metal time yield, MTY) of the Au-C catalysts

Catalyst	C/N/O/Au (atom%)$_{XPS}$	Au (wt%)$_{ICP}$	Average Au size (nm)$_{TEM}$	MTY (Mol$_{Glucose}$·Mol$^{-1}_{Au}$·s^{-1})
Au-C$_{Glucose}$	90/-/6.7/2.7	0.4	3.4 ± 1.1 (3.8±1.2)	1.5
Au-C$_{Glucose}$-O	89/-/10/0.5	0.4	n. d.	n. d.
Au-C$_{Glucose}$-H	90/-/9.9/0.4	0.4	4.4 ± 2.4 (5.2±2.5)	1.0
Au-C$_{Glucosamine}$	88/1.8/8.6/1.3	0.7	6.8 ± 2.4 (8.4±3.8)	0.2

v.   *Catalytic application: D – glucose oxidation reaction*

After synthesis and characterization of Au – C catalysts they were tested in a titration system for an oxidation reaction of aqueous D – glucose to form D – gluconic acid with molecular oxygen as the oxidizing agent. The conditions of the reaction were pH = 9, temperature of 45 °C, oxygen flow of 250 mL min^{-1} and stirring at 800 rpm. 50 mL of 0.1 M of glucose dissolved in D. W. was used, and the change of pH during reaction was adjusted by automatic addition of certain volume of 1 M aqueous NaOH solution. Details of the setup and the reaction are given in (Figure S. 26).

The results of the titration (Figure 30) illustrated a full glucose conversion for all catalysts used except for Au–C$_{Glucose}$–O. A varied catalytic activity expressed as metal time yield (MTY) for each catalyst was observed (Table 3).

The highest MTY between the catalysts is for Au–C$_{Glucose}$ (1.5 mol$_{Glucose}$· mol$_{Au}^{-1}$·s^{-1}) followed by Au–C$_{Glucose}$–H (1.1 mol$_{Glucose}$· mol$_{Au}^{-1}$s^{-1}). Both of these catalysts have hydrophobic surface chemistry as discussed in Ch.4.2.3 about the water adsorption measurement, and have smaller Au NPs which contributed to the rapid glucose conversion. Contrarily, Au–C$_{Glucoseamine}$ had significantly lower catalytic activity (0.2 mol$_{Glucose}$· mol$_{Au}^{-1}$s^{-1}) and the Au–C$_{Glucose}$–O had barely notable conversion. This can be referred to the particle size which is large in these two catalysts as detected by TEM (Table 3). Furthermore, it can be presumed that the hydrophilicity and strong adsorption of the substrate and product molecules on the porous catalyst support slower their transport to the catalytically active sites.
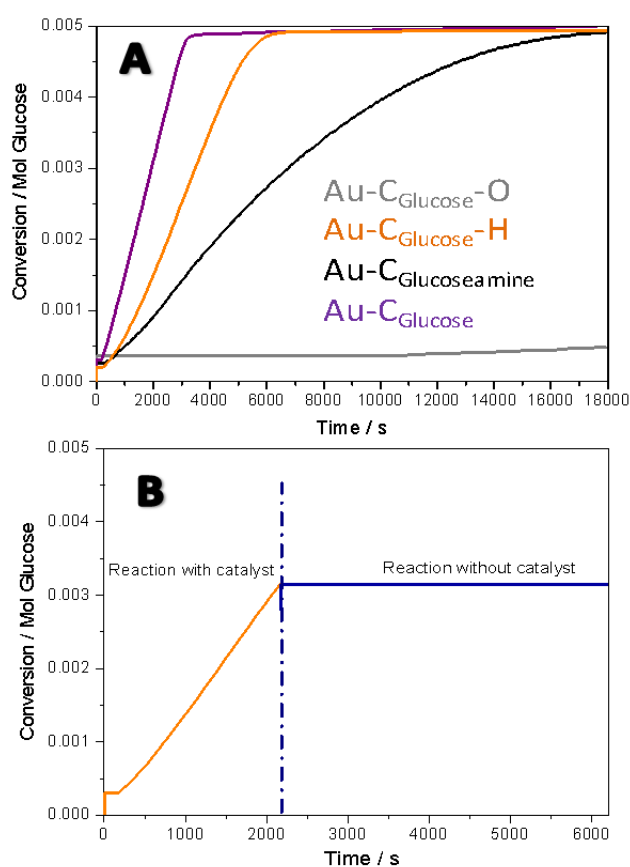
Figure 30: Glucose conversion of the Au-C$_{Glucose}$, Au-C$_{Glucose}$-H, Au-C$_{Glucosamine}$, and Au-C$_{Glucose}$-O catalysts as a function of time (A) and heterogeneity test of Au-C$_{Glucose}$ –H (B). Reaction conditions: ϑ = 45°C, pH = 9, O$_2$ flow ~ 250 mL.min^{-1}, C$_{Glucose}$ = 0.1 mol.L^{-1}, V = 50 mL, magnetic stirring at 800 rpm.

After the reaction the product was collected and separated from the catalyst by first centrifugation then filtration. Afterwards, it was analyzed by high pressure liquid chromatography (HPLC) to detect the selectivity of each catalyst. The data obtained (Figure S. 27) demonstrated the selectivity to producing gluconic acid from oxidizing glucose under the given conditions for all catalysts used except the Au–C$_{glucose}$–O and achieving full conversion of glucose as already given by titration.

Among various applications, Gluconic acid is applied in pharmaceuticals and food additives aside from the other applications. Therefore, for safety and health reasons leaking of metal in the product during catalysis has to be ruled out. To detect any possible Au NPs leaked in the glucose solution during reaction, a heterogeneity test was performed. This test is just a titration reaction of glucose under the same conditions and parameters applied. The only difference is at middle of the reaction the catalyst is removed and the reaction is continued to observe any possible change in pH and test for Au NPs leak. The titration outcomes (Figure 30 B) for Au–$C_{glucose}$–H, show a complete stop of addition of NaOH volume due to no change in pH and hence no Au leakage and no glucose conversion to acid without the catalysts takes place.
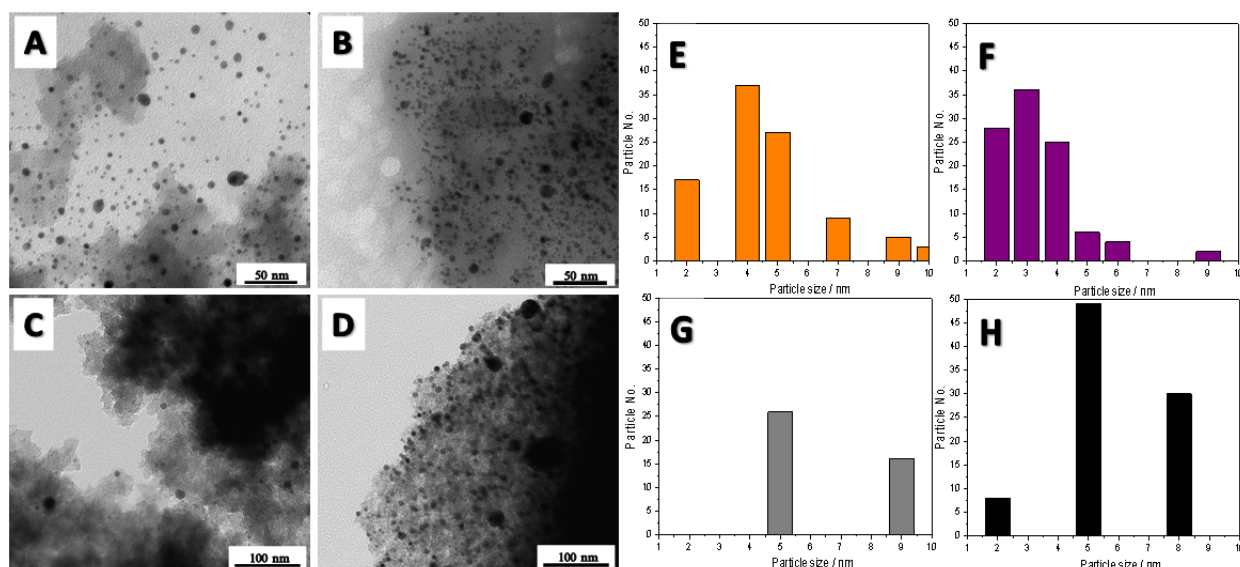
Figure 31: TEM images (A-D) and corresponding AuNP size distributions up to 10 nm (E-H) of the spent catalysts Au-$C_{Glucose}$-H (A,E), Au-$C_{Glucose}$ (B,F), Au-$C_{Glucose}$-O (C,G), and Au-$C_{Glucosamine}$ (D,H).

After the titration reaction, the catalysts were separated by centrifuge from the product and washed twice with deionized water (D.W.) then dried overnight in a vacuum oven at 60 °C. This is to observe the changes to the spent catalyst structure after a reaction but also to check for its stability. A TEM analysis was performed and provided that Au–$C_{Glucose}$–O had few Au NPs just as identified by TEM and XRD of the fresh catalyst. The other spent catalysts show that Au NPs have slightly grown in size compared to their fresh state and remained well dispersed, despite achieving full conversion and being active during reaction (Figure 31). The Au NPs of Au‑$C_{Glucoseamine}$ showed a distinctive growth of average diameter increasing from 6.8 nm to 8.4 nm.

A recyclability test was therefore performed for the three active catalysts (Figure S. 28). After a second cycle of titration and oxidation reaction the activity of Au–$C_{glucoseamine}$ has decreased notably, whereas Au–$C_{glucose}$–H and Au–$C_{glucose}$ had almost unchanged activity during the second cycle.

vi.   Summary and conclusion

In continuation step to understand the influence of heteroatoms on carbon supports and the catalyst, three different heteroatoms (H, O, and N) have been used to modify a hierarchically porous salt–melt carbon support. Later, four catalysts have been synthesized of the modified and unmodified porous salt–melt carbon supports to result with Au–$C_{Glucose}$–O, Au–$C_{Glucoseamine}$, Au–$C_{Glucose}$–H and Au–$C_{Glucose}$. In order to investigate the heteroatoms effect, oxidation of glucose in aqueous solution to form gluconic acid reaction has been applied. The activity, selectivity, and stability of the catalysts alongside with the heteroatoms influencing the properties of the carbon support and the catalyst and its interaction with the surrounding phase have all been investigated and discussed. Several characterization methods were performed. The results and data collected can be summarized as follows. A hydrophobic/ non–polar carbon surface ($C_{Glucose}$–H and $C_{Glucose}$) leads to smaller Au NPs and higher catalytic activity. Au–$C_{Glucose}$–H and Au–$C_{Glucose}$, and Au–$C_{Glucoseamine}$ have all reached full and selective conversion. Yet, the latter catalyst showed less activity due to its slightly larger average Au NPs. In contrast, Au–$C_{Glucose}$–O had almost no sign of activity regarding its large size of Au NPs formed during deposition on the hydrophilic support. An illustration is given in (Scheme 3). Under the applied reaction conditions, all catalysts showed full selectivity for the production of gluconic acid. In conclusion, the surface chemistry structure of the carbon material has direct influence on the metal deposition mechanism in aqueous solution and thus on the structure of the catalyst. As a result, an indirect influence of the surface of the support can be observed on the catalytic properties especially in oxidation reaction of glucose in an aqueous phase on gold surfaces. In this regard, a precise adjustment of this property of carbon supports is essential for the synthesis of suitable heterogeneous catalysts for liquid phase reactions.
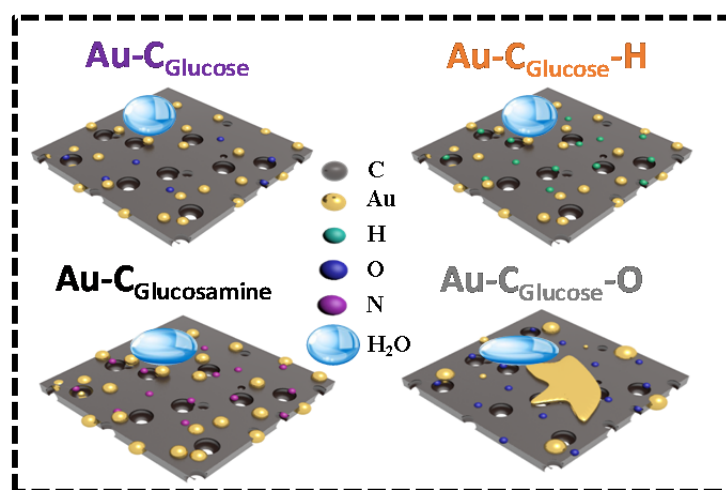
Scheme 3: Schematic structure of gold catalysts on salt-templated porous carbon supports with different surface polarity.

4.3.   Functionalized Carbons as Supports in Gas Phase Reaction: *Iron Nanoparticle Catalysts for Selective Lower Olefins Production from Syngas via Fischer Tropsch Synthesis*

i.   *Preface*

In this project a different carbon allotrope than salt-melt sugar- derived carbon is used. As mentioned in previous chapters, carbon material has several allotropes each with unique properties allowing it to advance in certain applications. Herein, salt-melt synthesized carbons are replaced with multi-walled carbon nanotubes (CNTs). In a process like Fischer-Tropsch, carbon nanotubes have better performance compared to the salt-melt carbon supports, all due to the CNTs' graphitic cylindrical layers shape which provide it with advanced properties e.g. high surface area, high conductivity, high thermal stability, good metal immobilization, and good mass transfer. Several studies have been given regarding the properties of CNTs; however the functionalization of CNTs' chemical surface is shortly introduced. Therefore, CNTs have been chosen for this study to provide more insights about CNTs functionalization and the influence of these functionalities on the catalytic properties especially in a gaseous phase.

ii.   *State of art*

The increase in global population requires sustainable resources of chemicals and energy that can comply with the rapid increase in demands [81-83]. The instability of fossil fuel reserves and price trigger the need for alternative routes for the production of chemical compounds that are so far produced from oil-based feedstock [84-85]. Carbon monoxide (CO) hydrogenation process, also widely known as the Fischer-Tropsch synthesis (FTS), is one possible strategy to provide various valuable chemicals. The hydrogenation reaction is a mixture of hydrogen (H_2) and CO known as synthesis gas/ syngas.[86-87] Syngas can be derived from biomass [88], coal [89], or natural gas [90] and can be converted into various hydrocarbon fractions via FTS process, which is also considered a surface polymerization reaction [54, 91]. Lower hydrocarbon chains as olefins (C_2-C_4) are of particular interest since they are important building blocks in the chemical industry [92]. The process involved for the direct transformation of syngas to such molecules is known as Fischer-Tropsch to olefins (FTO) reaction [93]. While metallic cobalt (Co) is the more attractive catalyst for the production of long-chain

molecules at low temperatures [54, 91], iron (Fe) especially Fe(carbide) is known to be selective to the production of low olefins (C_2-C_4) at relatively high-temperatures (300-350 °C) and thus the most established FTO catalyst [54, 91, 93-96]. Promoters (e.g. sodium/ sulfur (Na/S) [56, 97-98], or potassium (K) [99]) [100-101] are added to the metal active sites to enhance the selectivity and activity of FTO catalysts towards lower olefins production. Such an addition provides more facile carbide formation (to maximize the CO conversion), controls chain length distribution of the products (optimize C_2-C_4 yield and minimize methane formation), and favors ß-hydride abstraction instead of α-hydrogenation for chain growth termination (increase olefin/paraffin formation). In most cases, porous supports (e.g. silica (SiO_2) [102], alumina (Al_2O_3) [103], porous carbon [97]) are used to stabilize Fe nanoparticles and avoid deactivation of the catalysts due to particle growth. High surface area carbon supports have recently attracted considerable attention as FTO catalyst, because the transition metal (of which typically an oxidized phase is present after calcination) has only weak interaction with the carbon surface [66, 104]; Hence can be activated to the catalytically active Fe-carbide phase once exposed to syngas. Besides the strength of interaction of the Fe species with the support surface, other factors such as the carbon pore structure [102], surface chemical properties [105-106] and the Fe particle size [56-57] influence their activation behavior and stability.

1-dimensional carbon materials like carbon nanofibers and carbon nanotubes (CNTs) [107-109] are attractive supports for FTO catalysts. They are capable of immobilizing the active metal on their large external surface. Thus, the active sites are readily accessible for carbide formation and conversion of the syngas without diffusion limitations. Moreover, the inter-particular distance can be maximized allowing to a slow particle growth during FTO operation [108, 110-111], maintaining catalyst stability and activity for a longer time on stream.

The activation of Fe particles on carbon surfaces and the catalytic properties dependence on the surface functional groups are practical indications that a strong electronic communication is between the carbon support and the metal nanoparticles. The Fermi energy in both systems adapt to each other by changing the electron density in the interface layer [43, 112-113]. Besides the support geometry and the promoters' effects, this "junction" is another reason to further tune the properties of FTO catalysts.

In accordance, in this study, CNTs are modified with nitrogen doped carbon layer and compared to the catalytic properties of CNTs functionalized with standard surface functionalities. These functionalities are obtained after treatment in air (denoted as O),

hydrogen (denoted as H), ammonia (denoted as NH_3), or cyanamide solution (denoted as CN and referred to in text as N-doped carbon layer). N-doping in the surface of the carbon layer of the CNTs led to stabilization of small Fe particles up to ultra-small sub-nm Fe agglomerates even before activation. Additionally, the promoters (Na and S) led to enhancing the selectivity towards the production of low olefins chain (~47 %C), low methane formation (8 %C), high catalytic metal time yield activity (up to 94 x10^{-5} mol_{CO} g_{Fe}^{-1} s^{-1}) as compared to the unpromoted catalysts. Despite the low overall N-content (1 wt.%), the heterojunction effect between iron carbide and N-doped carbon layer on CNTs led to improved catalytic properties of the FTO catalysts as compared to the conventional surface functionalized CNTs.

iii.   Catalytical systems

1. Treatment of carbon nanotube supports

A batch of multi-walled CNTs (MWCNTs) purchased from Sigma-Aldrich (CAS 308068-56-6) is first oxidized in a muffle oven under air at 400 ^{o}C for 1 h. The corresponding support is denoted as CNT-O. Then, for CNT-H preparation, CNT-O material is heated in 5 vol. % H_2/Ar flow at a heating rate of 20 K min^{-1} up till 600 °C and hold for 2 h. CNT-CN is prepared by dispersing CNT-O in aqueous cyanamide (CN_2H_2) solution of 1 g$^.$ mL^{-1} with a CNT: CN_2H_2 ratio of 1:2. Then, the mixture is dried under static air at 60 ^{o}C for 12 h followed by subsequent calcination at a heating rate of 1 K min^{-1} up to 800 °C for 4 h under N_2 flow. The CNT-NH_3 is prepared through amination in a tubular oven. CNT-O is heated to 400 °C with 2.5 K.min^{-1} (from 25 °C to 350 °C within 2 h and 1 min hold followed by heating to 400 °C within 30 min to avoid overshooting of temperature) in a flow of 1 mL min^{-1} of 10 vol.% NH_3 in N_2. After 4 h at 400 °C the flow is changed to 900 mL min^{-1} N_2 and the oven is cooled down to room temperature.

2. Synthesis of Promoted and Unpromoted Iron Nanoparticles on functionalized Carbon Nanotubes Catalysts

The Promoted catalysts are labelled as Fe^P-CNT-X and the unpromoted ones as Fe-CNT-X where CNT-X is representing the respective support. 270 mg of each CNT-X support is impregnated with the following solution to prepare Fe^P-CNT-X: 187.5 mg of ammonium iron (III) citrate (Fluka, 14.5- 16 % iron) (iron precursor), 3.8 mg sodium citrate dihydrate (Na precursor), and 2.6 mg of iron (II) sulfate heptahydrate (sulfur

precursor) in ca. 0.6 mL H_2O in a mortar. Theoretically, from this procedure a 10 wt. % Fe promoted with 0.1 wt. % Na and 0.1 wt. % S are loaded on CNT-X supports.

Later on, the impregnated CNTs are first dried overnight at 60 °C under static air, then calcined at 500 °C in a tubular furnace under N_2 flow for 2 h on a heating rate of 2 °C · min^{-1}. The unpromoted catalysts are synthesized and calcined similarly as the Fe^P-CNT-X, but without the addition of the promoters (sodium citrate and iron (II) sulfate heptahydrate). Furthermore, the calcined promoted and unpromoted catalysts are sieved to a particle size between (63- 250) μm. An illustration of the functionalization and synthesis procedure is given in (Figure 32).
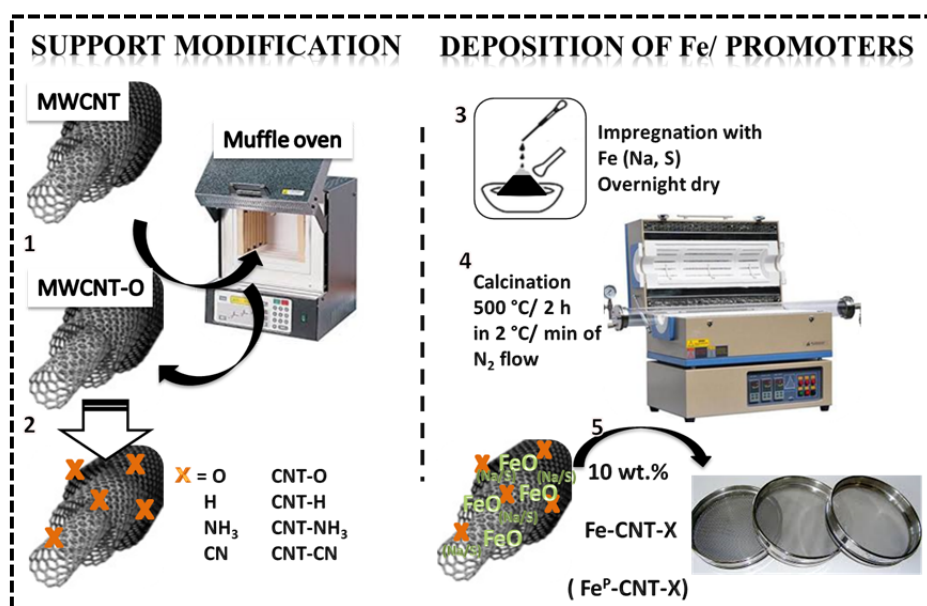
Figure 32: Sketch about carbon nanotube functionalization and impregnation with iron nanoparticles and promoters.

iv. Analysis and discussion

The surface structure of purchased multi-walled CNT material is modified with four different heteroatoms. Oxygen-functionalized CNTs is obtained by treatment of pristine CNTs at 400 °C in air (denoted as CNT-O). Part of this material is further treated once in ammonia at 400 °C and once in hydrogen at 600 °C to introduce amine and hydrogen groups replacing the oxygen groups (denoted as $CNT-NH_3$ and CNT-H). Another part of CNT-O is modified by a layer of N-doped carbon via the addition of cyanamide followed by calcination (CNT-CN). Resulting modified CNTs are used as supports to synthesize four promoted (~3 wt. % Na and ~1 wt. % S, relative to Fe) and four unpromoted catalysts with theoretical Fe contents of 10 wt. % to all by incipient wet impregnation followed by a calcination step.

Elemental analysis (E.A.) is carried out to quantify the elemental composition of the catalysts and the pristine supports (Table 4). Although the elemental compositions are not very different from each other, the amount of O detected is the highest in the CNT-O support and traces of nitrogen are detected in CNT-NH$_3$ and CNT-CN. Hence, the modification of the supports is successful. Also, higher nitrogen content is detected in the Fe-CNT-CN and Fe-CNT-NH$_3$ catalysts with and without promoters in comparison to Fe-CNT-O and Fe-CNT-H indicating that the nitrogen surface functionalization of the supports is also successfully translated to the calcined catalysts. The detected amount of oxygen and Fe of ~15 wt.% in calcined catalysts corresponds well to iron oxide (Fe$_2$O$_3$) and the surface oxygen groups which relates well with the targeted Fe loading of the catalysts of 10 wt.%. Moreover, there is no significant change in the compositions between Fe-CNTs-X and Fe^P-CNT-X catalysts, because only traces of promoters are added which do not influence the content of other elements during calcination.

In agreement to that, inductively coupled plasma optical emission spectroscopy (ICP-OES) data (Table 4) shows that all calcined catalysts contain 8-10 wt.% Fe, ~0.3 wt.% Na and ~0.1 wt.% S in good accordance with the targeted loadings. Thermal gravimetric analysis (TGA) results support the previous analysis where the remaining residual mass is comparable between each catalyst and is ~ 14 wt. % Fe (Figure S. 36). Significantly lower amounts of Na and S are detected in the unpromoted catalysts. Due to the comparable amount of these elements in the respective series of catalysts, it can be concluded that potential differences in their catalytic properties will not be caused by unwanted fluctuations of their promoter content. All the elements are homogeneously distributed on a microscale and no larger Fe agglomerates are observed outside of the CNT network as shown by SEM-EDX mapping (Figure S. 30-33). N$_2$-physisorption results (Table 4 and Figure S. 29) show the specific surface area (SSA) of the catalysts decreases slightly after Fe deposition due to the increase in mass loading. However, the pore features of the CNTs with large external surface area and large meso- and macro-porosity are neither changed significantly by the surface treatments nor by deposition of Fe$_2$O$_3$ nanoparticles resulting in a series of FTO catalysts with similar textural properties.

Table 4: Summary of porosity analysis, elemental analysis, ICP-OES and XPS data of the CNT-X material and the Fe-CNT-X catalysts

Support/ Catalyst	SSA (m²/g)	PV @ 20 nm (cm³/g)	C/N/H/O (+Fe) (wt%)$_{EA}$	Fe/C/O/N (wt. %)$_{XPS}$	Fe/Na/S (wt. %)$_{ICP}$	Average particle size ± standard deviation (pristine/ *spent*)
CNT-O	281.2	0.3	96.3/0.2/0.8/2.5	-/98/1.7/-	-	-
CNT-H	227.8	0.2	97.1/0.2/0.9/1.7	-/98/2.3 /-	-	-
CNT-CN	225.4	0.2	96.9/0.8/0.9/1.3	-/99/0.7/0.3	-	-
CNT-NH₃	231.7	0.2	96.6/0.4/1.0/2.0	-/99/0.9/0.1	-	-
Fe-CNT-O	183.8	0.2	82.2/0.7/1.0/16.0 (O+Fe)	0.8/97/2.2/-	9.2 /0.1/0.04	9.6 ± 3.9/ *9.7 ± 4.8*
Fe-CNT-H	173.7	0.2	82.9/0.7/1.1/15.3 (O+Fe)	0.8/95/4.2/-	8.6/0.06/0.02	7.0 ± 2.3/ *12.2 ± 10.1*
Fe-CNT-CN	207.3	0.3	81.5/1.2/1.0/16.3 (O+Fe)	0.9/95/2.9/0.9	7.9/0.06/0.03	8.6 ± 3.1/ *7.7 ± 3.4*
Fe-CNT-NH₃	220.0	0.4	82.9/0.8/1.0/15.3 (O+Fe)	0.9/95/3.6/0.5	8.9/0.1/0.02	9.0 ± 2.4/ *14.8 ± 12.6*
Fe^P-CNT-O	125.1	0.2	83.4/0.7/0.9/14.9 (O+Fe)	0.6/96.9/2.5/-	9.3/0.3/0.1	8.3 ± 4.0/ *13.8 ± 6.1*
Fe^P-CNT-H	161.8	0.3	83.7/0.7/1.1/14.4 (O+Fe)	1.0/96/3.0/-	9.8/0.3/0.1	12.8 ± 7.3/ *16.9 ± 4.0*
Fe^P-CNT-CN	153.4	0.2	81.7/1.2/1.0/16.1 (O+Fe)	1.2/94/3.8/0.9	8.7/0.3/0.1	7.5 ± 2.8/ *14.3 ± 6.6*
Fe^P-CNT-NH₃	184.9	0.3	82.3/0.8/1.1/15.8 (O+Fe)	0.6/97/2.3/0.3	9.4/0.3/0.1	9.7 ± 4.1/ *14.7 ± 15.3*

X-ray diffraction (XRD) measurements of the pristine supports (Figure 33A) show the typical graphitic-type peaks at 25.8°, 43°, and 53.6° 2θ resulting from the (002), (100), and (004) diffraction planes of the multi-walled CNTs. After Fe loading and calcination (Figure 33B and 33C), Fe is present as hematite in agreement with Raman spectroscopy and XPS discussed below. Significant peak broadening is observed for all catalysts, indicating the presence of Fe_2O_3 nanoparticles independent of the presence or absence of promoters and for all catalyst supports employed.

Raman spectroscopy measurements of the supports (Figure 33D) and the calcined catalysts (Figure 33E and 33F) show the typical D- and G-band contributions of the CNT supports as sharp peaks as well as the overtone bands D+G and G` at higher Raman shifts as it is typical for carbon materials with a high degree of local order such as CNTs. Independent of the support pretreatment, the shape of the spectra remains comparable thus indicating that all the supports will have a comparable carbon microstructure and that the different pretreatments do not significantly change the carbon atomic arrangement in the bulk of the CNTs. After loading of Fe precursor and calcination, peaks at wavelengths around 200-700 cm⁻¹ are seen in the promoted and unpromoted catalysts, which correspond to Fe species typical for α-Fe_2O_3 [114]. Due to the almost similar hematite content of all samples, their intensity is in the same range independent of the support and the presence or absence of Na and S.
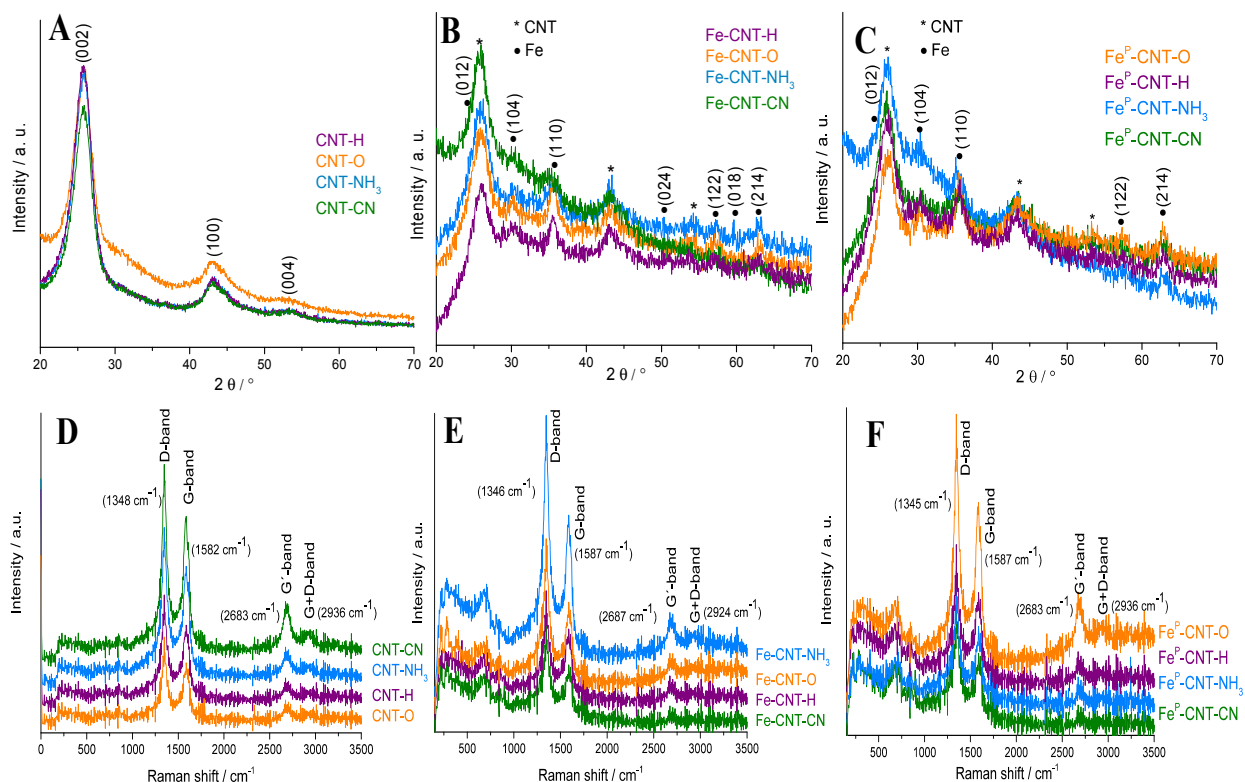
Figure 33: X-ray diffraction patterns (A-C) and Raman spectra (D-F) for CNT-X supports (A and D) as well as Fe-CNT-X catalysts (B and E) and Fe^P-CNT-X catalysts (C and F).

In agreement with the E.A., X-ray photoelectron spectroscopy (XPS) analysis of the supports and Fe-CNT-X catalysts (Table 4 and Figure S. 40) show the presence of traces of surface nitrogen in the supports and catalysts that contain NH_3 functional groups or an N-doped carbon surface layer. Although the detected nitrogen content is relatively low and the N 1s line scans have a low signal-to-noise ratio, it is clearly seen that the nitrogen signal for the ammonia-treated supports and catalysts is located at a binding energy of ~ 400 eV representative for surface-amine groups. Whereas, for the CNT-CN materials with a nitrogen-doped carbon layer on their surface the signal is located at slightly lower binding energy (Figure S. 40 [3] [6] [10]). The latter signal is typical for pyridine- or cyano-type nitrogen as typically present in nitrogen-doped carbons [115-116]. All catalysts and supports show comparable shapes of the C 1s spectra after the different surface treatments and after iron loading and calcination, which is in agreement with Raman spectroscopy analysis. The increase of the intensity of the O 1s contribution at ~530 eV after Fe loading corresponds to oxygen bonded in the Fe_2O_3. The Fe 2p is detected as two peaks that show the characteristic shape for Fe^{3+} at binding energy between ~709 eV ($Fe2p_{3/2}$) and ~725 eV ($Fe2p_{1/2}$), indicating that the Fe is present in form of Fe_2O_3 after calcination in all samples.

Scanning transmission electron microscopy (STEM) imaging of promoted (Figure 34 and Figure S. 35**)** and unpromoted (Figure S. 34) catalysts show the dispersion of Fe nanoparticles on the surface of the carbon material which is of typical appearance for Fe particles deposited on 1-dimensional supports. Particle size analysis shows the presence of Fe_2O_3 particles with an average size of 7-12 nm for promoted catalysts and 7- 9 nm for unpromoted catalysts (Figure 35).

The STEM-EELS mapping images (Figure 35) illustrate that solely Fe_2O_3 nanoparticles are present on the CNT-O and CNT-H supports. In contrast, the CNT-NH$_3$ and especially the CNT-CN supports can obviously stabilize much smaller Fe species even down to clusters of only few atoms or single Fe atoms. In agreement with literature [57, 106, 117], nitrogen groups can act as anchoring sites for the stabilization of smaller metal domains.
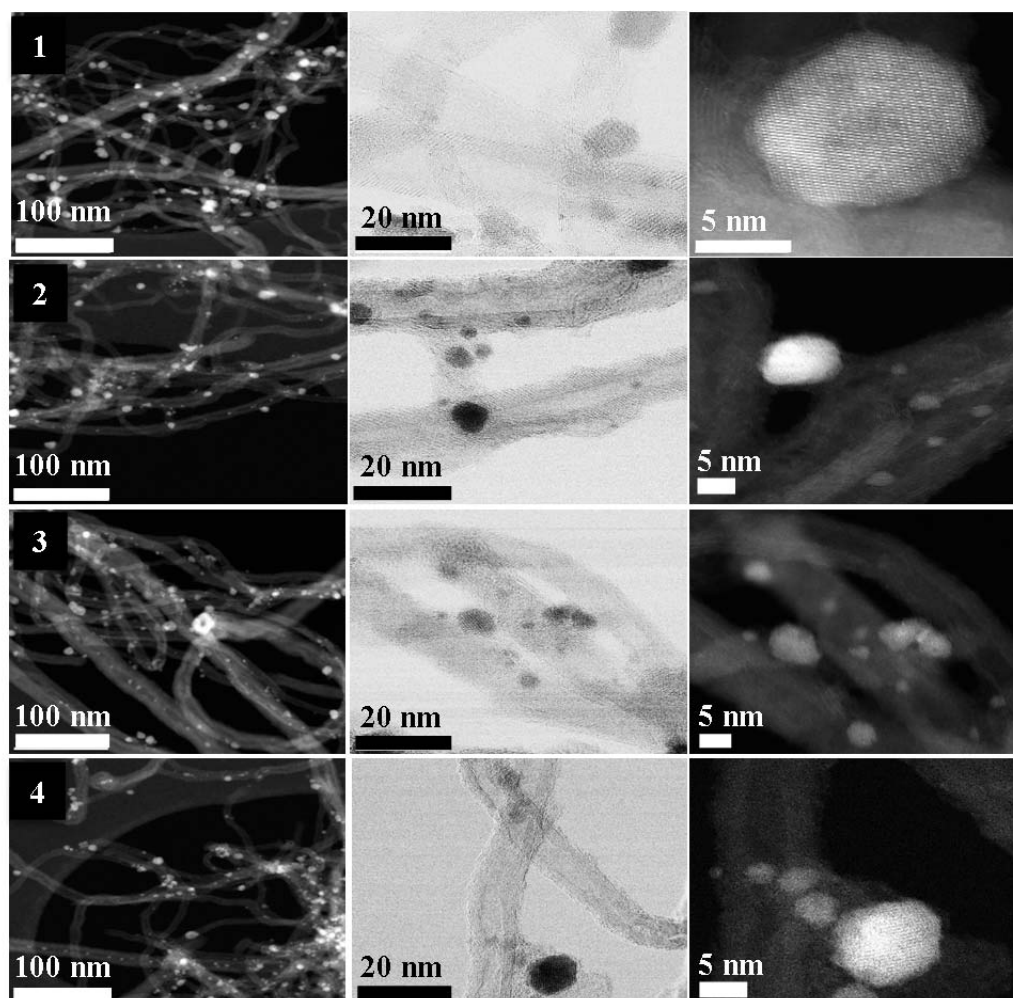
Figure 34: HR-STEM imaging of Fe^P-CNT-O (1), Fe^P-CNT-H (2), Fe^P-CNT- NH$_3$ (3), Fe^P-CNT-CN (4)
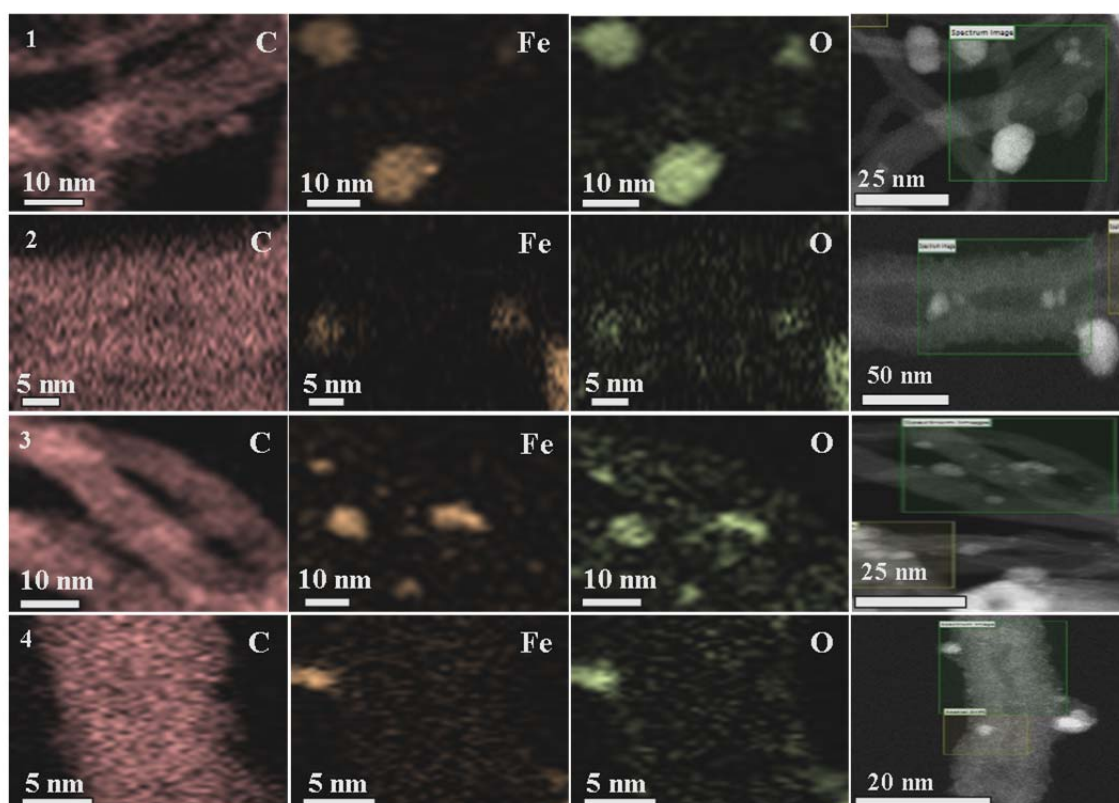
Figure 35: STEM- EELS mapping of Fe^P-CNT-O (1), Fe^P-CNT-H (2), Fe^P-CNT- NH_3 (3), Fe^P-CNT-CN (4).
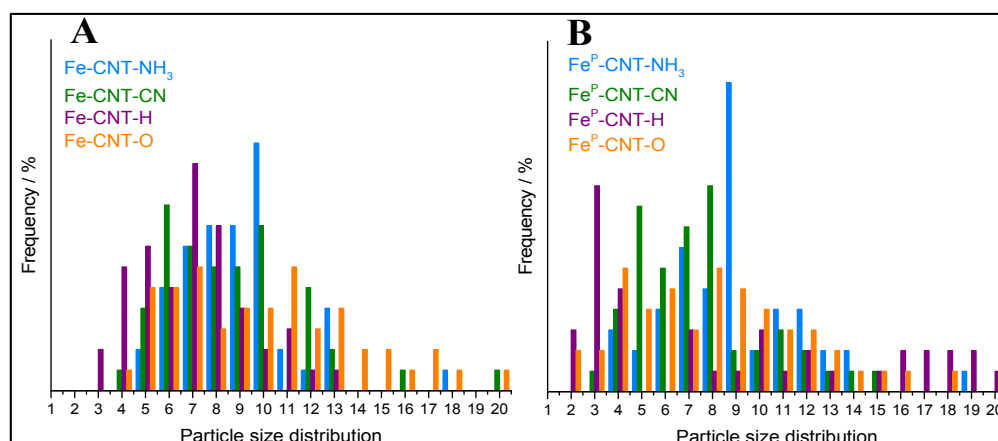
Figure 36: Particle size distribution of promoted (A) and unpromoted (B) pristine catalysts.

v. Catalytic Application: Fischer-Tropsch Reaction for Olefin Production

The catalytic testing is carried out in a 16-port high throughput fixed bed reactor system (Avantium Flowrence). The Fe-CNTs-X sieved catalysts are set in the fixed bed reactors to have the FTO reaction happening simultaneously, where 20 mg of the catalysts were diluted with 120 mg of SiC. Prior to application of reaction conditions, the calcined catalysts are reduced in-situ at 350 °C (5 °C min^{-1}) for 2 h in 30 % H_2 in He (v/v) at 3 bar and a gas hourly space velocity (GHSV, based on volume of undiluted FTO catalyst) of 3300 h^{-1} followed by a carburization step to convert the metallic iron to

iron carbide at 290 °C (5 °C min^{-1}) for 1 h in synthesis gas (H$_2$: CO = 1 v/v) at 3 bar and GHSV of 6000 h^{-1}. After carburization, reaction conditions are applied by increasing temperature to 340 °C with 5 °C min^{-1} in 10 bar of synthesis gas (H$_2$:CO= 2 v/v, 5 %$_{vol}$ He as internal standard) and GHSV=5000 h^{-1}. The product stream is diluted with N$_2$ (flow$_{diluent}$: flow$_{reactor, in}$ = 2.5) after the reaction to avoid condensation. The products are analyzed with an online-gas chromatograph equipped with a flame ionization detector (FID), a thermal conductivity detector (TCD), and a backflush system to analyze C$_1$-C$_9$ hydrocarbons and permanent gases. The syngas conversion by Fischer Tropsch reaction and the analysis of the products took place in the inorganic chemistry department of Prof. Krijn P. de Jong in Utrecht University in the Netherlands. A summary of the procedure of activating the catalyst for a FTO reaction is shown in (Figure 37). The selectivity of the promoted catalysts was calculated at a CO conversion of 80% and within a range of 36 - 57% for the unpromoted catalysts.
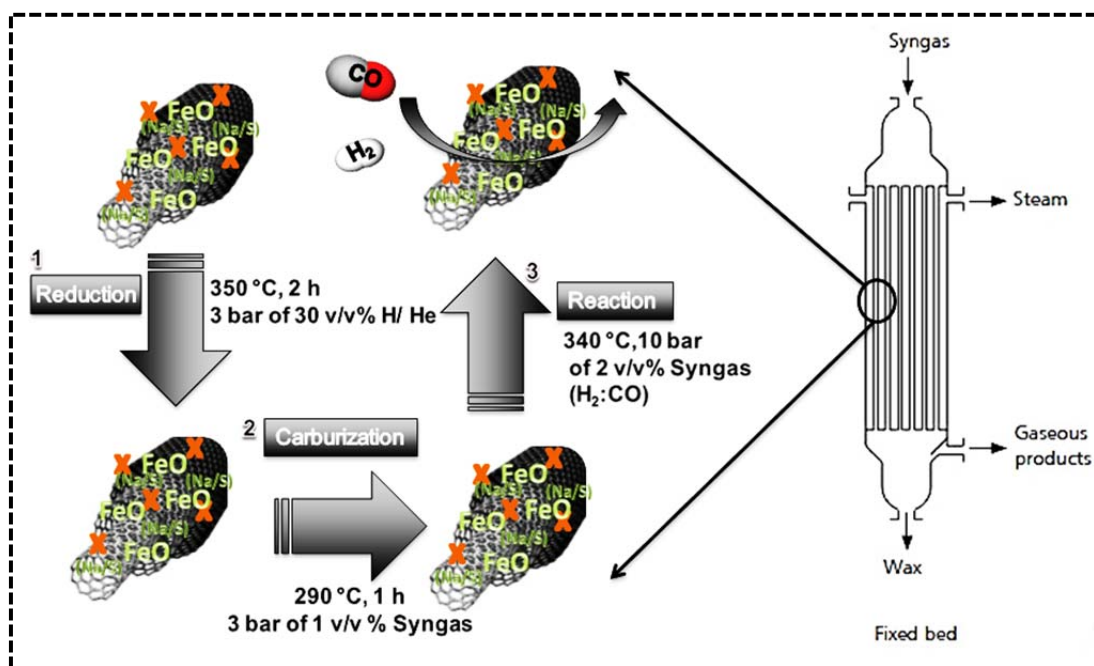
Figure 37: Summary of the reaction process of Fischer-Tropsch conversion of syngas in a fixed bed reactor.

After characterization of the pristine catalysts and the supports, the catalysts stability, selectivity, and activity are tested for FTO process. As this research aims towards further insights about the functional groups effect regarding a more efficient industrial catalyst, the conditions applied for this FTO test is in relevance with an industrial FTO conditions (T: 340 °C at 10 bar of synthesis gas (H$_2$:CO = 2 v/v). Therefore a ratio of H$_2$:CO= 2 v/v is employed to reduce coke formation and avoid sudden increase in pressure in the FTO experiment.

Among the unpromoted catalysts, Fe-CNT-CN shows the most rapid activation under FTO conditions and reaches its maximum activity already after ~37 h of time on stream with an iron time yield (FTY) of 85 mol_{CO} g_{Fe}^{-1} s^{-1} (Figure 38C) at 77 % CO conversion (Figure 38A) followed by slow loss of activity due to particle growth. Such a rapid Fe-carbide formation is usually not observable for unpromoted FTO catalysts on carbon supports [57, 97].

All other catalysts show a much slower carbide formation and do not reach a maximum in catalytic activity even after more than 180 h of time on stream (TOS). This significant difference is showing the beneficial promoting effect of a nitrogen-doped carbon surface layer on the formation of catalytically active Fe (carbide) species - even in absence of additional chemical promoters.

The origin of this enhanced activation is likely the formation of a space charge layer between Fe species and N-doped carbon. The latter is significantly more noble (i.e., the electrons in the N-doped carbon layer have a higher working potential than those in the surface-functionalized CNTs) [118]. Such interactions thus enhances the activation of Fe species by increasing their electron density [43]. In other words, this junction leads to enhanced CO binding properties of the Fe-based particles and thus more rapid carburization.

A comparable effect is described for N-doped carbon-supported nickel nanoparticles which showed high efficiency in methanol dehydrogenation due to the tailored adsorption enthalpy at the metal-support interface [112]. Furthermore, the N-doped carbon layer leads to enhanced dispersion and stabilization of much smaller Fe species as seen in TEM images which also lead to more rapid carbide formation.

In agreement with previous studies on mesoporous carbons and CNT supports with various surface functionalities [106-107], the NH_3-treated CNT support provides a higher activity and more rapid activation than CNT-O- and CNT-H supported unpromoted catalysts. However, the enhancement is less pronounced as compared to Fe-CNT-CN, indicating the importance of the particular species of nitrogen which is present on the support surface.

These significant differences in the activation properties of the catalysts become even much impressive when taking into consideration that there is only a comparably low ratio of nitrogen present on their surface. Selectivities of all unpromoted catalysts are comparable at 29 – 32 %$_C$ for C_2-C_4 olefin production and methane formation of more than 30 %C which are in a typical range for unpromoted FTO catalysts on carbon

supports under these conditions (Figure 38E)[97].

As it is typical for Na/S promoted FTO catalysts, all of them show a remarkably more rapid carbide formation (Figure 38D) as compared to the unpromoted analogues independent of the support. The Fe^P-CNT-CN catalyst reaches its maximum CO conversion (Figure 38B) still in significantly shorter time than the promoted catalysts on the other supports while the deactivation rate remains comparable. Moreover, this catalyst achieved the highest FTY among the promoted catalysts of 94×10^{-5} mol_{CO} g_{Fe}^{-1} s^{-1}. This FTY is among the highest reported so far, even as compared to optimized and promoted FTO catalysts that have been operated at higher syngas pressure [57, 66, 99, 105].

As it is typical for Na/S promoted FTO catalysts, methane and C_2-C_4 paraffin formation is lowered and C_{5+} formation increases as compared to the unpromoted catalysts. While no significant influence of the CNT surface structure on the product selectivity became obvious for the unpromoted catalysts, even further decreased methane formation, higher olefin/paraffin selectivity in the C_2-C_4 region and higher C_{5+} formation can be observed for the Fe^P-CNT-CN catalyst and (less pronounced) for the Fe^P-CNT-NH$_3$ catalyst – in spite of their comparable Fe particle size before (Figure 36) and after catalytic operation (Figure 40).

The rate of deactivation is comparable for all catalysts after 187 h of TOS with slight increase for both promoted and unpromoted catalysts, while the latter show the lower growing rate (Table 4). This is due to the loss of Fe (carbide) surface area as a result of particle growth which mainly trigged the catalyst deactivation (Figure 39). In agreement with previous studies, oxygen-treatment of the CNTs leads to undesired delay of catalyst activation and lower catalytic activity independent of the presence or absence of promoters [105-106]. A summary table of the catalysts performance is given in (Table S. 18).
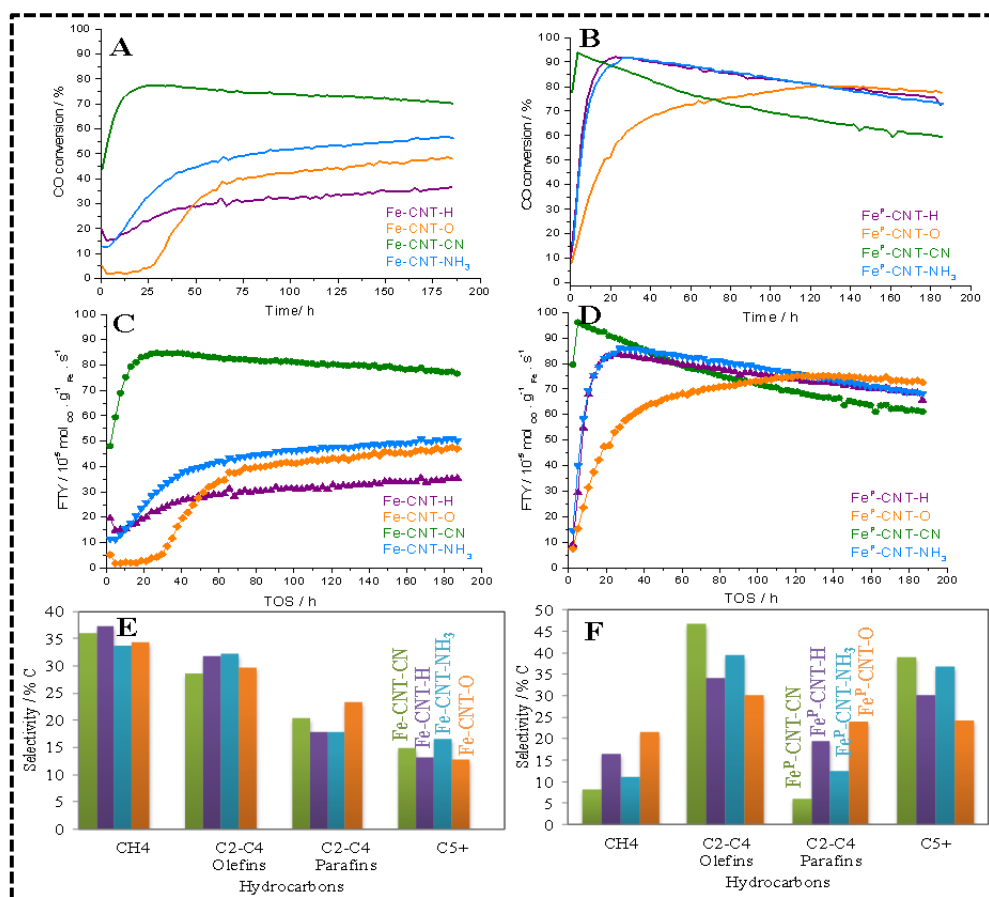
Figure 38: Percentage conversion of syngas (CO) per hour for unpromoted (A) and promoted catalysts (B).Iron time yield per time of stream for unpromoted (C) and promoted catalysts (D). Selectivity towards certain hydrocarbon groups for unpromoted (E) and promoted catalysts (F).
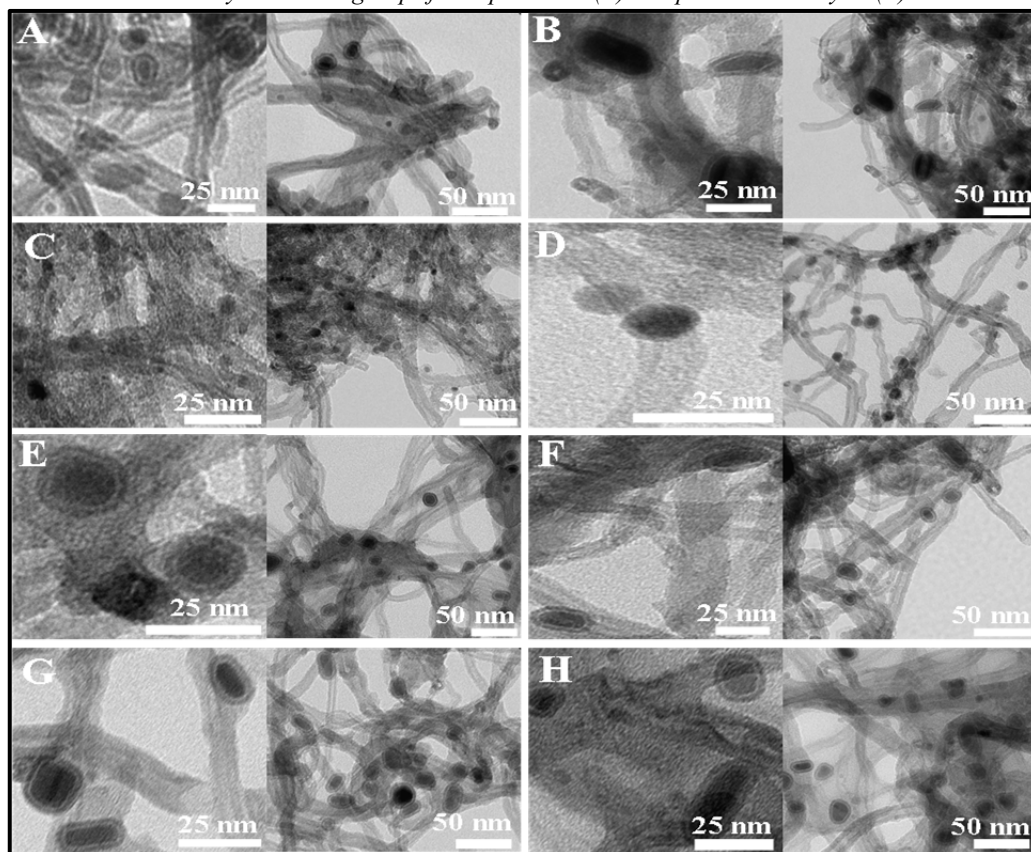
Figure 39: TEM of spent catalysts. sFe-CNT-O (A), sFe-CNT-H (B), sFe-CNT-CN (C), sFe-CNT-NH$_3$(D), and the sFe^P-CNT-O (E), sFe^P-CNT-H (F), sFe^P-CNT-CN (G), sFe^P-CNT-NH$_3$ (H).
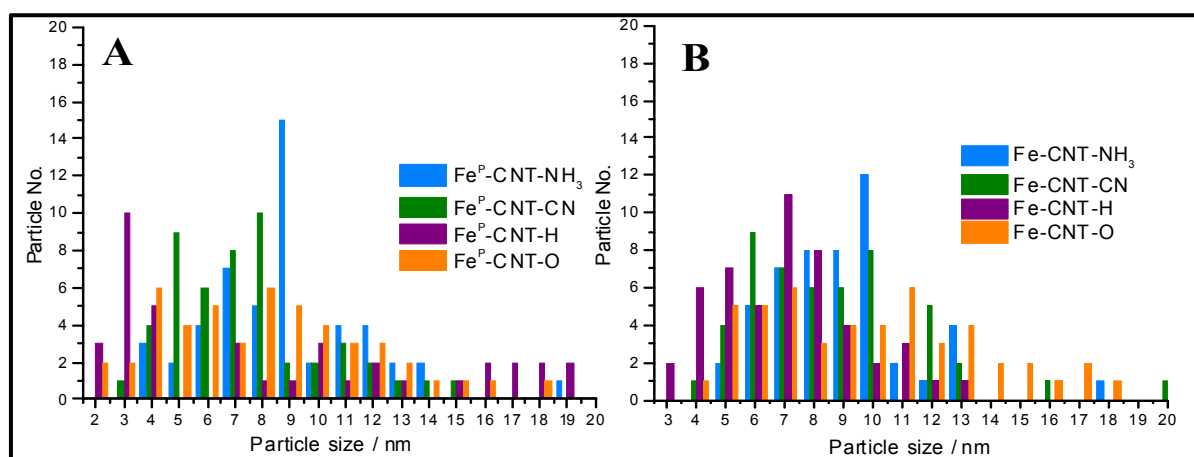
Figure 40: Particle size distributions of promoted (A) and unpromoted (B) spent catalysts.

vi. Summary and conclusion

Eight Fe- CNT catalysts are synthesized via incipient wet impregnation (IWI) using modified CNT material with O, H, CN, and NH_3 functional groups. Then, four of these catalysts are prepared with promoters (Na/ S) and the other four are used as such. The catalytic test is performed by a Fischer-Tropsch reaction in an aspiration to acquire high of the lower olefin hydrocarbon production selectivity with a main aim of providing deeper insights about different functionalities effect on the catalytical activity of Fe-CNTs-X catalysts in a gaseous phase. The modification of CNTs with various surface structures and their influence on the FTO catalytic properties of supported Fe nanoparticles is reported. While the textural properties (catalyst porosity, Fe phase, carbon microstructure of the CNTs) remain unaffected by the surface modifications, significant effects on the catalytic properties are observed in both presence and absence of Na/S chemical promoters. A nitrogen-doped carbon layer on the CNT surface can stabilize atomically small Fe species, in addition to Fe nanoparticles. Moreover, it can enable much faster activation of the Fe species and result in favorable C_2-C_4 olefin selectivity as compared to the supports modified with standard surface functional groups. In conclusion, based on the structure-performance relationships, a "tandem promotion" effect takes place in the Fe^P-CNT-CN catalyst. From the one-side, an electronic junction originates between the Fe species and the N-doped carbon layer on the CNT support, and on the other hand, the widely established Na/S promotion which is leading to rapid activation and record-high catalytic activity of the Fe(carbide). In this regards, this novel concept holds a great promise for future design of Fe-based FTO catalysts with still wide range for improvement regarding the nitrogen species and content in the support surface layer, thickness of the layer, its interplay with the chemical promoters, and the support geometry.

Chapter 5

Summary

„Nicht Kunst und Wissenschaft allein, Geduld will bei dem Werke sein."

(Goethe)

5. Summary

Chemicals represent an essential part in our daily life. They are applied in various products as for instance preservatives in food, in any kind of polymers, in IT products such as smart phones and computers, in transportation as fuel sources, and in many more. An increase in population number leads to an increase in the consumption of these chemicals resulting in an increase in demand for them. Fossil fuels, the main feedstock for energy and chemical production, are unstable resources and not renewable. Besides, they contribute to different environmental and political matters. Hence, the necessity for alternative sources for production of chemicals and energy raises. These feedstocks such as lignocellulosic biomass, coal, natural gas and others require different processing than fossil fuels, and thus industry needs to adapt its established systems and processes. Since industrially, heterogeneous catalytic conversions are the most applied process to obtain the chemicals from these feedstocks, the catalytic systems need further study and improvement. The catalyst activity, selectivity, stability, cost of preparation, and recyclation as well as the conditions required for activation of the catalyst influence the production rate, quantity, quality, and cost of the final product. Thus, optimization of these catalyst properties is crucial for being capable of satisfying the increasing demands in the future.

The development of a heterogeneous catalyst is investigated herein by modifying a catalyst surface chemistry structure not only with a hierarchical porous system, but also with surface functional heteroatom groups. The aim is to enhance the catalytic performance but to also provide a deeper insight regarding the interaction between the surface structure of catalyst and the surrounding phase. Such a study has rarely been carried out, especially the application of surface structure-modified catalyst in different phases (liquid and gaseous) and for different reactions (hydrogenation, oxidation, and hydrogenolysis). The heteroatoms utilized for the modifications are H, O, and N. Their effect on the metal particle size growth, polarity of the support (hence the catalyst), and the catalytic performance (activity, selectivity, and stability) has been explored.

At first, hierarchical porous sugar– and sugar amine– derived carbon supports (C and NDC) were synthesized via salt-melt method and compared to a commercially produced support (C $_{ref}$). Nickel (Ni) nanoparticles were deposited to produce Ni–NDC, Ni–C, and Ni–C $_{ref}$ catalysts. To investigate the effect of the heteroatom and the different porosity between these catalysts, hydrogenolysis of kraft lignin was chosen as a modal reaction and was performed in batch and continuous reactors. This investigation brought to sight the difference a heteroatom functionalized support can cause even when present in low concentrations (3 wt. %), besides the importance of a hierarchical porosity and

the surface area in a catalyst for higher performance. Moreover, deeper insights were given into the importance of utilizing a continuous reaction whether for the upmost use of the catalyst, or for the high product quality and quantity collection in comparison to a batch reaction.

Ni–NDC catalyst preparation via one–pot salt-melt support synthesis and incipient wet impregnation was successful. It performed efficiently compared to the other comparably prepared catalysts (Ni–C and Ni–C $_{ref}$) in means of activity, selectivity and stability. Its performance in a continuous reaction showed qualitatively to be higher than in a batch reaction. Eventually, complex kraft lignin structure degradation has been approved by the several techniques and analyses applied into lower molar mass molecule product mostly of guaiacol derivatives. Despite the successfulness, few drawbacks were present: one, the use of a relatively high concentrated Ni active metal for the catalysis in presence of low Nitrogen content making the Nitrogen effect less observable. Also, the leakage of the active metal (Ni) into the product collected. Therefore, for this project it is recommended to reduce the concentration of Ni metal, increase the density of the N-heteroatoms, or apply different heteroatoms to improve the immobilization effect.

In correspondence, synthesis of gold on carbon (Au–C) composites followed by exploring the functionalization of the sugar–derived carbon salt–melt support with varied heteroatoms (N, O, and H), and depositing Au nanoparticles via pre-reduced solution of Au. The functionalization of the heteroatoms was made without needing harsh acids that would require post treatment and are expensive when scaling up. In addition, impregnation method is replaced with pre-reduced Au nanoparticle solution for the reason of less energy and time consumption compared to impregnated catalyst.

The catalysts were applied for the selective glucose oxidation to gluconic acid in a liquid phase. The aim from this project is to determine the influence of these heteroatoms on the catalytic performance (activity, selectivity, and stability), on the particle size growth, and on the supports properties in correlation to another reaction type (e.g. oxidation) which is still applied in a liquid phase reaction.

Therefore, four catalysts have been synthesized of the modified and unmodified porous salt–melt carbon supports to result with Au–C$_{glucose}$–O, Au–C$_{glucoseamine}$, Au–C$_{glucose}$–H and Au–C$_{glucose}$. As the same support and metal are used, similar reaction rates and mechanism would take place. Hence, any different effect resulting for the catalytic performance is due to the different heteroatom modification. Of the different techniques performed, the heteroatoms showed direct effect on the supports polarity, and thus on

the size of the Au-nanoparticles deposited. Hence, the catalytic performance varied significantly. The results and data collected can be summarized as follows. A hydrophobic non–polar carbon surface ($C_{glucose}$–H and $C_{glucose}$) led to a smaller size of Au NPs and higher catalytic activity and selectivity. Au–$C_{glucose}$–H and Au–$C_{glucose}$, and Au–$C_{glucoseamine}$ have all reached full and selective conversion. Yet, the latter catalyst showed less activity due to its slightly larger average Au NPs. Whereas, Au–$C_{glucose}$–O had almost no sign of activity regarding its large size of Au NPs formed during deposition on the hydrophilic support. Of this work, it was concluded that the surface chemistry structure of the carbon material has direct influence on the metal deposition mechanism in aqueous solution and on the structure of the catalyst. As a result, an indirect influence of the surface of the support can be observed on the catalytic properties especially in oxidation reaction of glucose in an aqueous phase. Accordingly, a precise adjustment of such property in carbon material as supports is essential for the synthesis of suitable heterogeneous catalyst for liquid phase reactions.

As heteroatoms effect was obvious for the previous investigations, the study of the influence of these heteroatoms is further examined on a different allotrope of carbon such as multi-walled carbon nanotubes (CNTs) in a gaseous phase. Previously, heteroatoms were tested on amorphous and low ordered carbon supports and were found influential, and therefore it is intriguing to learn of any effect of heteroatoms on graphitically-layered and more ordered carbon support like CNTs. Furthermore, the carbon structure functionalization was checked in liquid phase in oxidation and hydrogenolysis processes, ergo exploring the effect in a gaseous phase would add a valuable understanding and provide a complete inquiry for the influence of functional modification of carbon surfaces in liquid and gas phases. In this regard, eight iron deposited on CNTs (Fe–CNT) catalysts have been synthesized via Incipient wet impregnation (IWI) using modified CNT supports with O, H, carbon nitride layer (CN), and NH_3 functional groups. As CNT is purchased, the incorporation of nitrogen heteroatoms was via soaking with cyanamide to obtain a N-doped/ carbon nitride layer on the CNT and via ammonia gasification to obtain amine functional group (NH_3). As these catalysts were used for a Fischer-Tropsch synthesis (FTS) process, and literature shows that the addition of promoters is an advantage, four of these catalysts have been prepared with promoters (Na/ S) and the other four have been used as such. The catalytic test is performed in Fischer-Tropsch reaction in the aim to acquire higher olefin- lower methane production selectivity. The results of this test show that promoted catalysts with modified CNT surface has higher stability, activity, and selectivity

compared to unpromoted ones. The N-groups are better heteroatoms in this case than the O or H functionalities. Distinctively, nitrogen from cyanamide treatment is much better than NH_3 treatment due to the state of N-incorporated in the CNT surface as a carbon nitride layer (CN) compared to that formed by NH_3 according to XPS data. Moreover, the combination of heteroatoms and promoters boosted the catalytic performance. Additionally, the faster the active phase iron carbide (Fe_3C) is formed during activation step, the higher the activity leading to more production despite the faster coking and reduced stability. Eventually for all the previous reasons, promoted iron nanoparticles deposited on CN modified CNTs (Fe^P-CNT-CN) performed the highest upon the rest of the catalysts with an activity of 94 x 10^{-5} mol_{CO} g $_{Fe}^{-1}s^{-1}$, selectivity to lower olefins production of 47 %, and a CO conversion reaching 92 % within 37 h.

Chapter 6

Conclusion

"Research is what I'm doing when I don't know what I'm doing."
(W. von Braun)

6. Conclusion and Perspective

The need for alternative sources of chemical feedstocks drives the quest for an improvement of the present industrial catalytic systems. Previously, diverse known approaches have been applied to improve the performance of a heterogeneous catalyst amongst them the focus on studying different metals, different supports, different methods of depositing the metal on the support, various preparation methods of nano-sized active metal, and the hierarchical ordered- and templated porosity of the support. However, very few is known regarding the influence of heteroatoms on the catalyst and its interplay with the surrounding phase. Such an influence is of huge importance but neglected by many literatures due to lack of information. Therefore, within the given context, a deeper insight into the heteroatoms effect on the catalyst and its performance has been achieved. The aim of the study was to expand the knowledge towards better understanding of the catalyst system, as well as to improve the industrial catalytic systems for the alternative feedstocks. From the discussed research in this thesis, it has been experimentally proven that even at low concentrations of (1-3) wt.% the heteroatoms clearly influenced the performance of the catalyst, regardless of the different concentration of the active metals used, and the different phases (liquid/ gas) and reactions (hydrogenolysis, oxidation, and hydrogenation/ polymerization) applied. Several points could be concluded from these experiments:

- Heteroatoms significantly influence the performance of the catalyst by effecting the deposition, stabilization, and electronic properties of the metal particles and the interaction of the catalyst with the surrounding phase as such.
- The same heteroatom can enhance or depress the activity of the catalyst depending on the phase and the type of the reaction applied.
- The state of bonding of the heteroatom to the support (e.g Nitrogen can bond in different states: such as amine, tertiary, or graphitic) influences the catalytic properties of the metallic nanoparticles.
- Different heteroatoms provide different influence on the catalyst performance depending on their electronic configuration influencing the electronic transfer between support and active metal.

In regards to the overall influence mentioned above, obviously precision in preparing such systems is very important and thus every single catalytic system and reaction has to be well controlled. Hence, in regards to the experimental results showing that heteroatoms can enhance the catalyst performance and in regards to the aim to provide

an improved industrial catalytic system, more is needed to be studied. Incorporation of other heteroatoms (e.g. sulfur and phosphorus) should be applied. This is important in order to further understand the interaction of the heteroatoms with the support and the active metal and how these interactions can be controlled. In addition, a study of different concentration of heteroatoms modifications is recommended. The density of the heteroatoms when functionalized in higher concentrations could reveal better and clearer information about the interaction with the metal for example, or with the support. The increase in the density of the heteroatoms may have a different effect on the properties of the catalyst compared to low density of heteroatoms.

Finally, heteroatom functionalization of the support is one interesting approach to achieve an advanced industrial heterogeneous catalyst. In this thesis few of the questions related to the effects heteroatoms can make are answered and new realizations have been given. However, more questions are raised. Such questions are how would an increase in this heteroatom doping influence the characteristics of the catalyst? Would a mixture of the heteroatoms be better or worse for the catalyst? What is the suitable ratio of heteroatoms functionalized to support? Would the ratio make much difference? All these questions and more are important to look into, to be able to provide an optimization to the effect of these incorporated functionalities. The more information given regarding this topic can open wide range of applications not only in catalysis, but in other approaches as well.

A. References

A. References

1. *World Health Statistics 2015*; WHO: 2015.
2. Komoda, T.; Matsunaga, T., Chapter 3 - Constituents of the Human Body. In *Biochemistry for Medical Professionals*, Academic Press: Boston, 2015; pp 7-24.
3. Westfall, C. S.; Muehler, A. M.; Jez, J. M., Enzyme Action in the Regulation of Plant Hormone Responses. *The Journal of Biological Chemistry* **2013,** *288* (27), 19304-19311.
4. Anuj Kumar Chandel, G. C., Konakalla Radhika, Rudravaram Ravinder and Pogaku Ravindra, Bioconversion of pentose sugars into ethanol: A review and future directions. *Biotechnology and Molecular Biology Reviews 6* **2011,** *1*, 8-20.
5. Vijayaraghavan, P.; Raj, S. R. F.; Vincent, S. G. P., Chapter 4 - Industrial Enzymes: Recovery and Purification Challenges A2 - Dhillon, Gurpreet Singh. In *Agro-Industrial Wastes as Feedstock for Enzyme Production*, Kaur, S., Ed. Academic Press: San Diego, 2016; pp 95-110.
6. Hagen, J., *Industrial Catalysis: A Practical Approach*. 2 ed.; Wiley-VCH Verlag GmbH & Co. KGaA: Germany, 2006.
7. Life expectancy at birth (years), 2000-2015. http://gamapserver.who.int/gho/interactive_charts/mbd/life_expectancy/atlas.html.
8. International Energy Outlook. https://www.eia.gov/outlooks/ieo/exec_summm.php.
9. Lindström, B.; Pettersson, L. J., A Brief History of Catalysis. *CATTECH* **2003,** *7* (4), 130-138.
10. Wisniak, J., The History of Catalysis: From the Beginning to Nobel Prizes. *Educación química* **2010,** *21*, 60-69.
11. Gates, B. C., *Catalytic chemistry*. Wiley: New York, 1992; Vol. 38, p 458.
12. Skinner, G. B., *Introduction to Chemical Kinetics*. Academic Press: 1974.
13. The rate of a reaction. http://www.chem.uiuc.edu/rogers/text13/tx133/tx133fr.html.
14. Boudart, M., Turnover Rates in Heterogeneous Catalysis. *Chemical Reviews* **1995,** *95* (3), 661-666.
15. Beller, M. R., Albert & Santen, R. A. van (Rutger A.), *Catalysis : from principles to applications* Weinheim Wiley-VCH: 2012.
16. Schmal, M., *Heterogeneous Catalysis and its Industrial Applications*. 1 ed.; Springer International Publishing: 2016.
17. *Handbook of Heterogeneous Catalysis*. Wiley VCH: 1997; Vol. 1.
18. N. N. Greenwood , A. E., 2 ed.; Butterworth-Heinemann 1997; p 1600.
19. *Carbon Materials for Catalysis*. John Wiley & Sons: 2009.
20. Lam, E.; Luong, J. H. T., Carbon Materials as Catalyst Supports and Catalysts in the Transformation of Biomass to Fuels and Chemicals. *ACS Catalysis* **2014,** *4* (10), 3393-3410.
21. CHAPTER 1. Carbon (Nano)materials for Catalysis. In *Nanostructured Carbon Materials for Catalysis*, 2015; pp 1-45.
22. Anna, D., King of the elements? *Nanotechnology* **2010,** *21* (30), 300201.
23. Boucher, E. A., Porous materials: structure, properties and capillary phenomena. *Journal of Materials Science* **1976,** *11* (9), 1734-1750.
24. *Handbook of Porous solids*. Wiley VCH: Weinheim, 2002.
25. Thommes, M.; Kaneko, K.; Neimark, A. V.; Olivier, J. P.; Rodriguez-Reinoso, F.; Rouquerol, J.; Sing, K. S. W., Physisorption of gases, with special reference to the evaluation of surface area and pore size distribution (IUPAC Technical Report). *Pure and Applied Chemistry* **2015,** *87* (9-10).
26. Wang, D. W.; Li, F.; Liu, M.; Lu, G. Q.; Cheng, H. M., 3D Aperiodic Hierarchical Porous Graphitic Carbon Material for High‐Rate Electrochemical

Capacitive Energy Storage. *Angewandte Chemie International Edition* **2008,** *47* (2), 373-376.

27. Ding, K.; Corma, A.; Maciá-Agulló, J. A.; Hu, J. G.; Krämer, S.; Stair, P. C.; Stucky, G. D., Constructing Hierarchical Porous Zeolites via Kinetic Regulation. *Journal of the American Chemical Society* **2015,** *137* (35), 11238-11241.

28. Gamby, J.; Taberna, P. L.; Simon, P.; Fauvarque, J. F.; Chesneau, M., Studies and characterisations of various activated carbons used for carbon/carbon supercapacitors. *Journal of Power Sources* **2001,** *101* (1), 109-116.

29. Liu, P. S.; Chen, G. F., Chapter One - General Introduction to Porous Materials. In *Porous Materials*, Butterworth-Heinemann: Boston, 2014; pp 1-20.

30. Liang, C.; Li, Z.; Dai, S., Mesoporous Carbon Materials: Synthesis and Modification. *Angewandte Chemie International Edition* **2008,** *47* (20), 3696-3717.

31. Molina-Sabio, M.; Rodríguez-Reinoso, F., Role of chemical activation in the development of carbon porosity. *Colloids and Surfaces A: Physicochemical and Engineering Aspects* **2004,** *241* (1), 15-25.

32. Ahmadpour, A.; Do, D. D., The preparation of active carbons from coal by chemical and physical activation. *Carbon* **1996,** *34* (4), 471-479.

33. Kaneko, K., Determination of pore size and pore size distribution: 1. Adsorbents and catalysts. *Journal of Membrane Science* **1994,** *96* (1), 59-89.

34. Kyotani, T., Control of pore structure in carbon. *Carbon* **2000,** *38* (2), 269-286.

35. Schüth, F., Endo‐ and Exotemplating to Create High‐Surface‐Area Inorganic Materials. *Angewandte Chemie International Edition* **2003,** *42* (31), 3604-3622.

36. Xie, Y.; Kocaefe, D.; Chen, C.; Kocaefe, Y., Review of Research on Template Methods in Preparation of Nanomaterials. *Journal of Nanomaterials* **2016,** *2016*, 10.

37. Fechler, N.; Fellinger, T. P.; Antonietti, M., "Salt Templating": A Simple and Sustainable Pathway toward Highly Porous Functional Carbons from Ionic Liquids. *Advanced Materials* **2013,** *25* (1), 75-79.

38. Liu, X.; Fechler, N.; Antonietti, M., Salt melt synthesis of ceramics, semiconductors and carbon nanostructures. *Chemical Society Reviews* **2013,** *42* (21), 8237-8265.

39. Liu, X.; Giordano, C.; Antonietti, M., A Facile Molten‐Salt Route to Graphene Synthesis. *Small* **2014,** *10* (1), 193-200.

40. Wisniak, J., The History of Catalysis. From the Beginning to Nobel Prizes. *Educ. quím, Universidad Nacional Autónoma de México* **2010,** *21* (1), 60-69.

41. Yuan, J.; Giordano, C.; Antonietti, M., Ionic Liquid Monomers and Polymers as Precursors of Highly Conductive, Mesoporous, Graphitic Carbon Nanostructures. *Chemistry of Materials* **2010,** *22* (17), 5003-5012.

42. Sakaushi, K.; Fellinger, T. P.; Antonietti, M., Bifunctional Metal‐Free Catalysis of Mesoporous Noble Carbons for Oxygen Reduction and Evolution Reactions. *ChemSusChem* **2015,** *8* (7), 1156-1160.

43. Li, X.-H.; Antonietti, M., Metal nanoparticles at mesoporous N-doped carbons and carbon nitrides: functional Mott-Schottky heterojunctions for catalysis. *Chemical Society Reviews* **2013,** *42* (16), 6593-6604.

44. Cornish-Bowden, A., *Fundamentals of Enzyme Kinetics*. 4 ed.; Wiley-VCH Verlag GmbH & Co.: 2012.

45. The Basics of Catalysis. In *Catalysis*.

46. Xia, Q.; Chen, Z.; Shao, Y.; Gong, X.; Wang, H.; Liu, X.; Parker, S. F.; Han, X.; Yang, S.; Wang, Y., Direct hydrodeoxygenation of raw woody biomass into liquid alkanes. *Nature Communications* **2016,** *7*, 11162.

47.   Zakzeski, J.; Jongerius, A. L.; Bruijnincx, P. C.; Weckhuysen, B. M., Catalytic lignin valorization process for the production of aromatic chemicals and hydrogen. *ChemSusChem* **2012,** *5* (8), 1602-9.

48.   Zakzeski, J. B., P.; Jongerius, A.; Weckhuysen, B., The Catalytic Valorisation of Lignin for the production of Renewable Chemicals. *Chem. Rev.* **2010,** *110*, 3552-3599.

49.   Biella, S.; Prati, L.; Rossi, M., Selective Oxidation of D-Glucose on Gold Catalyst. *Journal of Catalysis* **2002,** *206* (2), 242-247.

50.   Okatsu, H.; Kinoshita, N.; Akita, T.; Ishida, T.; Haruta, M., Deposition of gold nanoparticles on carbons for aerobic glucose oxidation. *Applied Catalysis A: General* **2009,** *369* (1-2), 8-14.

51.   Anastassiadis, S.; Morgunov, I. G., Gluconic acid production. *Recent patents on biotechnology* **2007,** *1* (2), 167-80.

52.   Alshammari, A.; Kalevaru, V. N., Supported Gold Nanoparticles as Promising Catalysts. In *Catalytic Application of Nano-Gold Catalysts*, 2016.

53.   Colmenares, J. C.; Luque, R., Heterogeneous photocatalytic nanomaterials: prospects and challenges in selective transformations of biomass-derived compounds. *Chemical Society Reviews* **2014,** *43* (3), 765-778.

54.   Jahangiri, H.; Bennett, J.; Mahjoubi, P.; Wilson, K.; Gu, S., A review of advanced catalyst development for Fischer–Tropsch synthesis of hydrocarbons from biomass derived syn-gas. *Catal. Sci. Technol.* **2014,** *4* (8), 2210-2229.

55.   Chen, W.; Lin, T.; Dai, Y.; An, Y.; Yu, F.; Zhong, L.; Li, S.; Sun, Y., Recent advances in the investigation of nanoeffects of Fischer-Tropsch catalysts. *Catalysis Today* **2017**.

56.   Xie, J.; Yang, J.; Dugulan, A. I.; Holmen, A.; Chen, D.; de Jong, K. P.; Louwerse, M. J., Size and Promoter Effects in Supported Iron Fischer–Tropsch Catalysts: Insights from Experiment and Theory. *ACS Catalysis* **2016,** *6* (5), 3147-3157.

57.   Xie, J.; Torres Galvis, H. M.; Koeken, A. C. J.; Kirilin, A.; Dugulan, A. I.; Ruitenbeek, M.; de Jong, K. P., Size and Promoter Effects on Stability of Carbon-Nanofiber-Supported Iron-Based Fischer–Tropsch Catalysts. *ACS Catalysis* **2016,** *6* (6), 4017-4024.

58.   deLlano-Paz, F.; Calvo-Silvosa, A.; Iglesias Antelo, S.; Soares, I., The European low-carbon mix for 2030: The role of renewable energy sources in an environmentally and socially efficient approach. *Renewable and Sustainable Energy Reviews* **2015,** *48*, 49-61.

59.   Anastas, P.; Eghbali, N., Green chemistry: principles and practice. *Chem Soc Rev* **2010,** *39* (1), 301-12.

60.   Wang, X.; Rinaldi, R., Solvent effects on the hydrogenolysis of diphenyl ether with Raney nickel and their implications for the conversion of lignin. *ChemSusChem* **2012,** *5* (8), 1455-66.

61.   Zhao, C.; Kou, Y.; Lemonidou, A. A.; Li, X.; Lercher, J. A., Highly selective catalytic conversion of phenolic bio-oil to alkanes. *Angew Chem Int Ed Engl* **2009,** *48* (22), 3987-90.

62.   Ohta, H.; Kobayashi, H.; Hara, K.; Fukuoka, A., Hydrodeoxygenation of phenols as lignin models under acid-free conditions with carbon-supported platinum catalysts. *Chem Commun (Camb)* **2011,** *47* (44), 12209-11.

63.   Cui, X.; Surkus, A. E.; Junge, K.; Topf, C.; Radnik, J.; Kreyenschulte, C.; Beller, M., Highly selective hydrogenation of arenes using nanostructured ruthenium catalysts modified with a carbon-nitrogen matrix. *Nat Commun* **2016,** *7*, 11326.

64.   Christopher, L. P., CHAPTER 1. Integrated Forest Biorefineries: Current State and Development Potential. **2012**, 1-66.

65. Rodríguez-reinoso, F., The role of carbon materials in heterogeneous catalysis. *Carbon* **1998,** *36* (3), 159-175.

66. Torres Galvis, H. M.; Bitter, J. H.; Khare, C. B.; Ruitenbeek, M.; Dugulan, A. I.; de Jong, K. P., Supported Iron Nanoparticles as Catalysts for Sustainable Production of Lower Olefins. *Science* **2012,** *335* (6070), 835-838.

67. Vainio, U.; Maximova, N.; Hortling, B.; Laine, J.; Stenius, P.; Simola, L. K.; Gravitis, J.; Serimaa, R., Morphology of Dry Lignins and Size and Shape of Dissolved Kraft Lignin Particles by X-ray Scattering. *Langmuir* **2004,** *20* (22), 9736-9744.

68. Lama, S. M. G.; Pampel, J.; Fellinger, T.-P.; Beškoski, V. P.; Slavković-Beškoski, L.; Antonietti, M.; Molinari, V., Efficiency of Ni Nanoparticles Supported on Hierarchical Porous Nitrogen-Doped Carbon for Hydrogenolysis of Kraft Lignin in Flow and Batch Systems. *ACS Sustainable Chemistry & Engineering* **2017**.

69. Li, M.; Xu, F.; Li, H.; Wang, Y., Nitrogen-doped porous carbon materials: promising catalysts or catalyst supports for heterogeneous hydrogenation and oxidation. *Catalysis Science & Technology* **2016,** *6* (11), 3670-3693.

70. Zhang, P.; Zhu, H.; Dai, S., Porous Carbon Supports: Recent Advances with Various Morphologies and Compositions. *ChemCatChem* **2015,** *7* (18), 2788-2805.

71. Okatsu, H.; Kinoshita, N.; Akita, T.; Ishida, T.; Haruta, M., Deposition of gold nanoparticles on carbons for aerobic glucose oxidation. *Applied Catalysis A: General* **2009,** *369* (1), 8-14.

72. Önal, Y.; Schimpf, S.; Claus, P., Structure sensitivity and kinetics of d-glucose oxidation to d-gluconic acid over carbon-supported gold catalysts. *Journal of Catalysis* **2004,** *223* (1), 122-133.

73. Fischer, C.; Adam, M.; Mueller, A. C.; Sperling, E.; Wustmann, M.; van Pée, K.-H.; Kaskel, S.; Brunner, E., Gold Nanoparticle-Decorated Diatom Biosilica: A Favorable Catalyst for the Oxidation of d-Glucose. *ACS Omega* **2016,** *1* (6), 1253-1261.

74. Ishida, T.; Kinoshita, N.; Okatsu, H.; Akita, T.; Takei, T.; Haruta, M., Influence of the Support and the Size of Gold Clusters on Catalytic Activity for Glucose Oxidation. *Angewandte Chemie International Edition* **2008,** *47* (48), 9265-9268.

75. Cañete-Rodríguez, A. M.; Santos-Dueñas, I. M.; Jiménez-Hornero, J. E.; Ehrenreich, A.; Liebl, W.; García-García, I., Gluconic acid: Properties, production methods and applications—An excellent opportunity for agro-industrial by-products and waste bio-valorization. *Process Biochemistry* **2016,** *51* (12), 1891-1903.

76. Singh, O. V.; Kumar, R., Biotechnological production of gluconic acid: future implications. *Applied Microbiology and Biotechnology* **2007,** *75* (4), 713-722.

77. Beltrame, P.; Comotti, M.; Pina, C. D.; Rossi, M., Aerobic oxidation of glucose I. Enzymatic catalysis. *Journal of Catalysis* **2004,** *228* (2), 282-287.

78. Beltrame, P.; Comotti, M.; Della Pina, C.; Rossi, M., Aerobic oxidation of glucose: II. Catalysis by colloidal gold. *Applied Catalysis A: General* **2006,** *297* (1), 1-7.

79. Wojcieszak, R.; Ferraz, C.; Sha, J.; Houda, S.; Rossi, L.; Paul, S., Advances in Base-Free Oxidation of Bio-Based Compounds on Supported Gold Catalysts. *Catalysts* **2017,** *7* (11), 352.

80. Della Pina, C.; Falletta, E.; Prati, L.; Rossi, M., Selective oxidation using gold. *Chem Soc Rev* **2008,** *37* (9), 2077-95.

81. Sir David King, C. G. *Energy Harnessing: New Solutions for Sustainability and Growing Demand*; the University of Cambridge, United Kingdom, 2013.

82. Nathalie Girouard, E. K., Cecilia Tam and Peter; Taylor, B. B., Debra Justus, William Blyth *OECD Green Growth Studies: Energy*; 2011.

83. Owusu, P. A.; Asumadu-Sarkodie, S.; Dubey, S., A review of renewable energy sources, sustainability issues and climate change mitigation. *Cogent Engineering* **2016,** *3* (1).

84. Abas, N.; Kalair, A.; Khan, N., Review of fossil fuels and future energy technologies. *Futures* **2015,** *69*, 31-49.

85. Nelder, B. H. a. C., *Profit from the Peak*. John Wiley & Sons: Canada, 2008.

86. Schulz, H., Short history and present trends of Fischer‑Tropsch synthesis. *Applied Catalysis A: General* **1999,** *186* (1), 3-12.

87. Dalai, A. K.; Davis, B. H., Fischer‑Tropsch synthesis: A review of water effects on the performances of unsupported and supported Co catalysts. *Applied Catalysis A: General* **2008,** *348* (1), 1-15.

88. Lozano, F. J.; Lozano, R., Assessing the potential sustainability benefits of agricultural residues: Biomass conversion to syngas for energy generation or to chemicals production. *Journal of Cleaner Production* **2018,** *172*, 4162-4169.

89. Chen, Z.; Dun, Q.; Shi, Y.; Lai, D.; Zhou, Y.; Gao, S.; Xu, G., High quality syngas production from catalytic coal gasification using disposable Ca(OH)2 catalyst. *Chemical Engineering Journal* **2017,** *316*, 842-849.

90. Kathe, M.; Empfield, A.; Sandvik, P.; Fryer, C.; Zhang, Y.; Blair, E.; Fan, L.-S., Utilization of CO2 as a partial substitute for methane feedstock in chemical looping methane‑steam redox processes for syngas production. *Energy & Environmental Science* **2017,** *10* (6), 1345-1349.

91. Zhang, Q.; Kang, J.; Wang, Y., Development of Novel Catalysts for Fischer-Tropsch Synthesis: Tuning the Product Selectivity. *ChemCatChem* **2010,** *2* (9), 1030-1058.

92. Corma, A.; Corresa, E.; Mathieu, Y.; Sauvanaud, L.; Al-Bogami, S.; Al-Ghrami, M. S.; Bourane, A., Crude oil to chemicals: light olefins from crude oil. *Catalysis Science & Technology* **2017,** *7* (1), 12-46.

93. Torres Galvis, H. M.; de Jong, K. P., Catalysts for Production of Lower Olefins from Synthesis Gas: A Review. *ACS Catalysis* **2013,** *3* (9), 2130-2149.

94. Wang, D.; Chen, B.; Duan, X.; Chen, D.; Zhou, X., Iron-based Fischer‑Tropsch synthesis of lower olefins: The nature of x-Fe5C2 catalyst and why and how to introduce promoters. *Journal of Energy Chemistry* **2016,** *25* (6), 911-916.

95. Lu, Y.; Yan, Q.; Han, J.; Cao, B.; Street, J.; Yu, F., Fischer‑Tropsch synthesis of olefin-rich liquid hydrocarbons from biomass-derived syngas over carbon-encapsulated iron carbide/iron nanoparticles catalyst. *Fuel* **2017,** *193*, 369-384.

96. Sun, B.; Xu, K.; Nguyen, L.; Qiao, M.; Tao, F., Preparation and Catalysis of Carbon‑Supported Iron Catalysts for Fischer‑Tropsch Synthesis. *ChemCatChem* **2012,** *4* (10), 1498-1511.

97. Oschatz, M.; Krans, N.; Xie, J.; de Jong, K. P., Systematic variation of the sodium/sulfur promoter content on carbon-supported iron catalysts for the Fischer‑Tropsch to olefins reaction. *Journal of Energy Chemistry* **2016,** *25* (6), 985-993.

98. Oschatz, M.; Krause, S.; Krans, N. A.; Hernandez Mejia, C.; Kaskel, S.; de Jong, K. P., Influence of precursor porosity on sodium and sulfur promoted iron/carbon Fischer-Tropsch catalysts derived from metal-organic frameworks. *Chemical Communications* **2017,** *53* (73), 10204-10207.

99. Santos, V. P.; Wezendonk, T. A.; Jaén, J. J. D.; Dugulan, A. I.; Nasalevich, M. A.; Islam, H.-U.; Chojecki, A.; Sartipi, S.; Sun, X.; Hakeem, A. A.; Koeken, A. C. J.; Ruitenbeek, M.; Davidian, T.; Meima, G. R.; Sankar, G.; Kapteijn, F.; Makkee,

M.; Gascon, J., Metal organic framework-mediated synthesis of highly active and stable Fischer-Tropsch catalysts. *Nature Communications* **2015,** *6*, 6451.

100. Zhai, P.; Xu, C.; Gao, R.; Liu, X.; Li, M.; Li, W.; Fu, X.; Jia, C.; Xie, J.; Zhao, M.; Wang, X.; Li, Y. W.; Zhang, Q.; Wen, X. D.; Ma, D., Highly Tunable Selectivity for Syngas‐Derived Alkenes over Zinc and Sodium‐Modulated Fe5C2 Catalyst. *Angewandte Chemie International Edition* **2016,** *55* (34), 9902-9907.

101. An, X.; Wu, B.-s.; Wan, H.-J.; Li, T.-Z.; Tao, Z.-C.; Xiang, H.-W.; Li, Y.-W., Comparative study of iron-based Fischer‐Tropsch synthesis catalyst promoted with potassium or sodium. *Catalysis Communications* **2007,** *8* (12), 1957-1962.

102. Cheng, K.; Virginie, M.; Ordomsky, V. V.; Cordier, C.; Chernavskii, P. A.; Ivantsov, M. I.; Paul, S.; Wang, Y.; Khodakov, A. Y., Pore size effects in high-temperature Fischer‐Tropsch synthesis over supported iron catalysts. *Journal of Catalysis* **2015,** *328*, 139-150.

103. Torres Galvis, H. M.; Koeken, A. C. J.; Bitter, J. H.; Davidian, T.; Ruitenbeek, M.; Dugulan, A. I.; de Jong, K. P., Effects of sodium and sulfur on catalytic performance of supported iron catalysts for the Fischer‐Tropsch synthesis of lower olefins. *Journal of Catalysis* **2013,** *303*, 22-30.

104. Chen, W.; Pan, X.; Bao, X., Tuning of Redox Properties of Iron and Iron Oxides via Encapsulation within Carbon Nanotubes. *Journal of the American Chemical Society* **2007,** *129* (23), 7421-7426.

105. Chew, L. M.; Xia, W.; Düdder, H.; Weide, P.; Ruland, H.; Muhler, M., On the role of the stability of functional groups in multi-walled carbon nanotubes applied as support in iron-based high-temperature Fischer‐Tropsch synthesis. *Catalysis Today* **2016,** *270*, 85-92.

106. Oschatz, M.; Hofmann, J. P.; Deelen, T. W. v.; Lamme, W. S.; Krans, N. A.; Hensen, E. J. M.; Jong, K. P. d., Effects of the Functionalization of the Ordered Mesoporous Carbon Support Surface on Iron Catalysts for the Fischer‐Tropsch Synthesis of Lower Olefins. *ChemCatChem* **2017,** *9* (4), 620-628.

107. Schulte, H. J.; Graf, B.; Xia, W.; Muhler, M., Nitrogen‐ and Oxygen‐Functionalized Multiwalled Carbon Nanotubes Used as Support in Iron‐Catalyzed, High‐Temperature Fischer‐Tropsch Synthesis. *ChemCatChem* **2012,** *4* (3), 350-355.

108. Duan, X.; Wang, D.; Qian, G.; Walmsley, J. C.; Holmen, A.; Chen, D.; Zhou, X., Fabrication of K-promoted iron/carbon nanotubes composite catalysts for the Fischer‐Tropsch synthesis of lower olefins. *Journal of Energy Chemistry* **2016,** *25* (2), 311-317.

109. Lu, J.; Yang, L.; Xu, B.; Wu, Q.; Zhang, D.; Yuan, S.; Zhai, Y.; Wang, X.; Fan, Y.; Hu, Z., Promotion Effects of Nitrogen Doping into Carbon Nanotubes on Supported Iron Fischer‐Tropsch Catalysts for Lower Olefins. *ACS Catalysis* **2014,** *4* (2), 613-621.

110. Abbaslou, R. M. M.; Tavassoli, A.; Soltan, J.; Dalai, A. K., Iron catalysts supported on carbon nanotubes for Fischer‐Tropsch synthesis: Effect of catalytic site position. *Applied Catalysis A: General* **2009,** *367* (1-2), 47-52.

111. Bahome, M. C.; Jewell, L. L.; Hildebrandt, D.; Glasser, D.; Coville, N. J., Fischer‐Tropsch synthesis over iron catalysts supported on carbon nanotubes. *Applied Catalysis A: General* **2005,** *287* (1), 60-67.

112. Xue, Z. H.; Han, J. T.; Feng, W. J.; Yu, Q. Y.; Li, X. H.; Antonietti, M.; Chen, J. S., Tuning the Adsorption Energy of Methanol Molecules Along Ni‐N‐Doped Carbon Phase Boundaries by the Mott‐Schottky Effect for Gas‐Phase

Methanol Dehydrogenation. *Angewandte Chemie International Edition* **2018,** *57* (10), 2697-2701.

113. Su, H.; Zhang, K.-X.; Zhang, B.; Wang, H.-H.; Yu, Q.-Y.; Li, X.-H.; Antonietti, M.; Chen, J.-S., Activating Cobalt Nanoparticles via the Mott‐Schottky Effect in Nitrogen-Rich Carbon Shells for Base-Free Aerobic Oxidation of Alcohols to Esters. *Journal of the American Chemical Society* **2017,** *139* (2), 811-818.

114. Fu, D.; Dai, W.; Xu, X.; Mao, W.; Su, J.; Zhang, Z.; Shi, B.; Smith, J.; Li, P.; Xu, J.; Han, Y. F., Probing The Structure Evolution of Iron‐Based Fischer‐Tropsch to Produce Olefins by Operando Raman Spectroscopy. *ChemCatChem* **2015,** *7* (5), 752-756.

115. Morant, C.; Andrey, J.; Prieto, P.; Mendiola, D.; Sanz, J. M.; Elizalde, E., XPS characterization of nitrogen‐doped carbon nanotubes. *physica status solidi (a)* **2006,** *203* (6), 1069-1075.

116. Higgins, D. C.; Wu, J.; Li, W.; Chen, Z., Cyanamide derived thin film on carbon nanotubes as metal free oxygen reduction reaction electrocatalyst. *Electrochimica Acta* **2012,** *59*, 8-13.

117. J., S. H.; Barbara, G.; Wei, X.; Martin, M., Nitrogen- and Oxygen-Functionalized Multiwalled Carbon Nanotubes Used as Support in Iron-Catalyzed, High-Temperature Fischer‐Tropsch Synthesis. *ChemCatChem* **2012,** *4* (3), 350-355.

118. Antonietti, M.; Oschatz, M., The Concept of "Noble, Heteroatom‐Doped Carbons," Their Directed Synthesis by Electronic Band Control of Carbonization, and Applications in Catalysis and Energy Materials. *Advanced Materials 0* (0), 1706836.

B. Appendix

B. Appendix

a. List of abbreviations

Symbol	Description
MOF	Metal organic frameworks
SiO_2	Silica
TiO_2	Titania
WHO	World Health Organization
IUPAC	International Union of Pure and Applied Chemistry
d	Diameter
LiCl	Lithium Chloride
KCl	Potassium Chloride
CO_2	Carbon dioxide
H_2O	water
KOH	Potassium hydroxide
$ZnCl_4$	Zinc Chloride
SSA	Specific Surface Area
IL	Ionic Liquids
NaCL	Sodium Chloride
CVD	Chemical Vapour Deposition
NDC	Nitrogen Doped carbon
Pt	Platinum
Pd	Palladium
AuNPs	Gold Nanoparticles
CO	Carbon Monoxide, CO and H2 make a synthetic gas
H_2	Hydrogen
FTS	Fischer Tropsch Synthesis
FTO	Fischer Tropsch Synthesis of Olefins
-H/ -O/ -N	A material functionalized with Hydrogen, Oxygen, or Nitrogen heteroatoms
$C_{Glucose}$ (-H/-O)	Carbon synthesized from glucose precursor and functionalized with Hydrogen or Oxygen.
$C_{Glucoseamine}$	Carbon synthesized from glucoseamine precursor to functionalize it with Nitrogen.

C ref.	Carbon reference (purchased carbon Vulcan)
e.V	Electron volt
v/v or Vol%	Volume percentage
IWI	Inciepient wet impregnation
Ni	Nickel
FeO	Iron oxide
XRD	Powder X-ray diffraction
HCl	Hydrogen chloride
(FeCl$_2$)$_{aq.}$	Iron chloride aqueous
SEM-EDX	Scanning electron microscopy-energy dispersive X-ray analysis
(HR)-TEM	(High resolution) Transmission electron microscopy
TGA	Thermal gravimetric Analysis
Ni-NDC	Nickel metal deposited on nitrogen doped carbon support
Ni-C	Nickel metal deposited on carbon from glucose pecursor support
Ni-C ref.	Nickel metal deposited on carbon reference support
E.A.	Elemental Analysis
FWHM	Full width at half maxima
I$_D$/I$_G$	Intensity of D-band vs. Intensity of G-band
TPV	Total pore volume
D-/G-band	Diamond or graphite band
2D-(^{13}C/^{1}H) NMR	Two dimensional carbon hydrogen Nuclear magnetic resonance
ICP-OES	Inductively coupled plasma optical emission spectrometry
2D-GCxGC-MS	Two dimensional gas chromatography mass spectroscopy
GC-FID	Gas chromatography flame ionization detector
GPC/SEC	Gas permeable chromatography/ size exclusion chromatography
β-O-4	Ether linkage
XPS	X ray photon spectroscopy
LPR	Liquid phase reaction
Au-C$_{Glucose}$ (-H/-O)	Gold reduced deposited on carbon support derived from glucose and modified with hydrogen or oxygen
Au-C$_{Glucoseamine}$	Gold reduced deposited on carbon support derived from glucoseamine to modify with N
H$_2$O$_2$	Hydrogen peroxide

O 1s/C 1s/ Fe 2p	S and p molecular orbits
B.E.	Binding energy
D.W.	Distilled water
QSDFT	Quenched solid state density functional theory
H$_2$O physisorption	Water physisorption
pH	Degree of protonation / acidity
T	temperature
rpm	Round per minute
HPLC	High pressure liquid chromatography
NaOH	Sodium hydroxide
Fe	iron
Na	sodium
S	sulfur
Al$_2$O$_3$	alumina
CNT -CN/ -NH$_3$/- H/-O	Multi walled carbon nanotube functionalized under cyanamide treatment, or ammonia treatment, or hydrogen and oxygen treatments
CN$_2$H$_2$	Cyanamide
Fe-CNT-CN/ - NH$_3$/-H/-O	Iron deposited on Multi walled carbon nanotube support functionalized under cyanamide treatment, or ammonia treatment, or hydrogen and oxygen treatments
Fe^P-CNT-CN/ - NH$_3$/-H/-O	Iron with promoters (sodium and sulfur) deposited on Multi walled carbon nanotube support functionalized under cyanamide treatment, or ammonia treatment, or hydrogen and oxygen treatments
sFe$^{(P)}$-CNT-CN/ - NH$_3$/-H/-O	Spent catalyst of iron (promoted) deposited on multi walled carbon nanotube support functionalized under cyanamide treatment, or ammonia treatment, or hydrogen and oxygen treatments
PSD	Pore size distribution
TCD	Thermal conductivity detector
Wt.%	Weight percentage
TOS	Time on stream
FTY	Iron time yield
MTY	Metal time yield

b. List of Materials

Material	Supplier and description
Batch reactor	Parr Instrument company
Filter paper	Whatman® Prepleated Qualitative Filter Paper, Grade 1V, pore size 11 μm
Flow reactor	Thalesnano, continuous fixed-bed reactor set-up H-CUBE Pro™
Cartridge	Thalesnano, Medium sized empty cartridge
Zinc Chloride	Sigma-Aldrich, $ZnCl_2$
D(+)-Glucose	Roth, $\geq$ 99.5 %, $C_6H_{12}O_6$
D-Gluconic acid	Sigma-Aldrich, 49-53 wt.% in H_2O, $C_6H_{12}O_7$
Tetrachloroauric (III) acid trihydrate	Alfa-Aesar, 99.99%, $HAuCl_4.3H_2O$
Sodium borohydride	Sigma-Aldrich, $\geq$98.0% , $NaBH_4$
Sodium citrate tribasic dihydrate	Sigma-Aldrich, $\geq$99.0%, $HOC (COONa)(CH_2COONa)_2 \cdot 2H_2O$
Sodium hydroxide	Roth, $\geq$99.0%, NaOH
Hydrochloric acid	Roth, 37%, HCl
Multiwalled carbon nanotube	Sigma-Aldrich, MWCNT
Potassium chloride	Roth, 99.5%, KCl
D-Glucoseamine hydrochloride	Alfa-Aesar, 98%, $C_6H_{13}NO_5$•HCl
Kraft lignin	UPM BioPiva™
Vulcan® Carbon	Cabot corporation
Nickel Nitrate hexahydrate	Sigma-Aldrich, 99.99%, $NiNO_3.6H_2O$
Ethanol	Sigma-Aldrich, 99.5%, C_2H_5OH
D.W.	Distilled water
Cyanamide	Sigma-Aldrich, 100% , CN_2H_2
Ammonium iron (III) citrate	Fluka, 14.5- 16 % iron
Iron (II) sulfate heptahydrate	Sigma-Aldrich, $FeO_4S \cdot 7H_2O$

c. List of Gases

Gas	Supplier and description
Oxygen 5.0	Air Liquide, 99,999%, O_2
Hydrogen 3.0	Air Liquide, 99,999%,, H_2
Nitrogen 5.0	Air Liquide, 99,999%, N_2
Helium 5.0	Air Liquide, 99,999%, He
Argon 5.0	Air Liquide, 99,999%, Ar

d. Characterization methods

In order to investigate the influence of the heteroatoms on the support properties, on the active metal properties, and on the catalyst system performance, it is necessary to maintain a comparable structure and characteristics of the catalysts prepared so as any detected differences would be concluded as a result of the heteroatom functionalization. In that consequence, several characterization methods have been applied to ensure comparability and understand/ control the differences in the prepared systems. Hereby, this supporting chapter provides the procedures applied for each analysis performed within the discussed research.

i. Characterization of nickel carbon modified catalysts for kraft lignin hydrogenolysis in liquid phase reaction

Two dimensional – gas chromatography mass spectrometry *(2D - GC $\times$ GC-MS)* has been applied by dissolving degraded lignin samples in dichloromethane and sonicating for 15 minutes. The suspensions were filtered (membrane filter 0.45 µm, Agilent) and sample solutions were analyzed using GC$\times$GC-MS gas chromatograph-quadrupole mass spectrometer GCMS-QP2010 Ultra (Shimadzu, Kyoto, Japan) and ZX2 thermal modulation system (Zoex Corp.) as Total Ion Chromatograms (TIC). A Rtx®-1 (first column: RESTEK, Crossbond® 100% dimethyl polysiloxane, 30 m, 0.25 mm ID, df=0.25 µm) and a BPX50 (SGE Analytical Science, 1 m, 0.1 mm ID, df=0.1 µm) column were connected through the GC$\times$GC modulator as the first and second capillary columns, respectively. The temperature started with an isothermal step at 40 °C for 5 min then it was increased from to 300 °C by 5.2 °C min^{-1} to finish with an isothermal step at 300 °C for 5 min. The modulation applied for the comprehensive GC$\times$GC analysis was a hot jet pulse (400 ms) every 9000 ms. The MS data was collected with Shimadzu GC/MS Real Time Analysis. The GC$\times$GC-MS data were analyzed

using ChromeSquare 2.1 software, which is capable of directly reading GC×GC data obtained with GC-MS solution, converting it to a 2-dimensional image. The degradation products were identified by a search of the MS spectrum with the MS libraries NIST 11, NIST 11s, and Wiley 8.

The X-ray diffraction measurements *(XRD)* are equipped with a Bruker D8 diffractometer with Cu-K$^{\alpha}$ source (λ = 0.154 nm) and a scintillation counter. The reference patterns are found in the ICDD PDF-4+ database (2014 edition).

The transmission electron microscopy (*TEM*) has a Zeiss EM 912 Ω microscope used at an acceleration voltage of 120 kV.

The scanning electron microscopy *(SEM)* device used has a LEO 1550 Gemini microscope.

The Nitrogen gas sorption (*N$_2$-physisorption*) applied used a Quantachrome Quadrasorb apparatus. The analysis starts with degassing of each sample at 150 °C for 20 hours, and then the results are shown via QuadraWin software (version 5.05). Pore size distributions (PSDs), specific surface areas (SSAs), total pore volumes (TPVs) up to 50 nm, and micropore volumes (MPVs) were calculated from isotherm analysis with the quenched solid density functional theory (QSDFT) method for nitrogen adsorbed on carbon with slit/cylindrical/spherical pores at -196 °C (adsorption branch kernel).

The Elemental analysis (**E.A**) used a combustion analysis of a Vario Micro device.

The two dimensional nuclear magnetic resonance *(2D-NMR ^{1}H-^{13}C HSQC)* spectra were obtained through an agilent 400 MHz spectrometer in deuterated solvents.

The Size exclusion chromatography *(GPC/ SEC)* with UV/RI detection performed via N-methyl-2-pyrrolidone as eluent at 70° C using two PSS-GRAM columns (300 mm, 8 mm^2). The average particle size used was of 7 μm and the porosity measured between 100–1000 Å. The Standard for the calibration was Polystyrene. Conversions and yields for lignin reaction were calculated by mass difference after liquid chromatographic separation.

The gas chromatography flame ionization detector (*GC-FID*) was performed using Agilent technologies 5975 gas chromatograph equipped with an FID detector combined

with a second HP-5MS capillary column. The temperature program for degraded lignin was set with an isothermal step to start at 50 °C for 2 min then it increases to 300 °C at a rate of 10 °C min⁻¹ for 20 min, where the temperature of the detector is kept at 280 °C. The evaluation of small molecular weight molecules concentration, yielded after lignin degradation was achieved with GC-FID measurements. The integration of the signals derived from lignin derived products was compared to an internal standard (Heptane).

The **Raman** spectra was obtained using a Renishaw inVia Raman Microscope operating with an objective (Nikon, 10x/0.25, ∞/− WD 6.1) and an excitation wavelength of 532 nm with a power of 4.0 mW. From the obtained Raman spectra the D and G bands were fitted with a Lorentz function.

ii. Characterization of gold carbon modified catalysts for glucose oxidation in aqueous phase reaction

Transmission electron microscopy (**TEM**) images were obtained by using a Zeiss EM 912 Ω TEM microscope at an acceleration voltage of 120 kV. The samples were dropwise immobilized on the carbon-coated copper TEM grid after dispersing in ethanol. The Particle size distributions were calculated manually using the Image J software (v. 1.47).

The Nitrogen gas sorption (**N₂-physisorption**) experiments were carried out at -196 °C at a Quantachrome Quadrasorb apparatus. Before starting the analysis samples were degassed at 150 ° C for 20 h. Results were analyzed with the QuadraWin software (version 5.05). Pore size distributions (PSDs), specific surface areas (SSAs), total pore volumes (TPVs) up to 50 nm, and micropore volumes (MPVs) were calculated from isotherm analysis with the quenched solid density functional theory (QSDFT) method for nitrogen adsorbed on carbon with slit/cylindrical/spherical pores at -196 °C (adsorption branch kernel).

Water vapor physisorption (**H₂O-physisorption**) isotherms were measured with a Quantachrome Autosorb IQ instrument at 25 °C.

The Elemental analysis *(E.A)* was carried out by combustion analysis in a Vario Micro device.

X-ray photoelectron spectroscopy *(XPS)* measurements were performed using a Thermo Scientific K-Alpha+ X-ray Photoelectron Spectrometer. All samples were analyzed

using a microfocused, monochromated Al K^α X-ray source (1486.68 eV; 400 μm spot size). The K-Alpha+ charge compensation system was employed during analysis to prevent any localized charge buildup. The samples were mounted on conductive carbon tape and each sample was measured at 10 different spots. The spectra of the 10 spots were averaged and the resulting spectra analyzed using the Avantage software from Thermo Scientific.

Thermogravimetric analyses *(TGA)* were performed using a thermo microbalance TG 209 F1 Libra from Netzsch. A platinum crucible was used for the measurement of 10 ± 1 mg of samples in a nitrogen flow of 20 ml min^{-1} and a purge flow of 20 ml min^{-1}. The samples were heated with to 800 °C with 2.5 K min^{-1}.

X-ray diffraction *(XRD)* experiments were carried out with a Bruker D8 diffractometer and with a CuK$^\alpha$ source (λ = 0.154 nm) and a scintillation counter. The reference patterns were found in the ICDD PDF-4+ database (2014 edition).

Inductively coupled plasma-optical emission spectrometry *(ICP-OES)* was conducted using a Horiba Ultra 2 instrument equipped with photomultiplier tube detection. Prior to the measurements the carbon supports were burned off at 800 °C under air atmosphere in a muffle furnace and the residual material was dissolved in aqua regia prior to the measurements.

The *Raman* spectra was obtained using a Renishaw inVia Raman Microscope operating with an objective (Nikon, 10x/0.25, ∞/− WD 6.1) and an excitation wavelength of 532 nm with a power of 4.0 mW. From the obtained Raman spectra the D and G bands were fitted with a Lorentz function.

Dynamic light scattering **(DLS)** utilized using an ALV-7004 Multiple Tau Digital Correlator in combination with a CGS-3 Compact Goniometer and a HeNe laser (Polytec, 34 mW, λ = 633 nm at θ = 90° setup for DLS). Temperature applied isset to 25 °C. Toluene was used as immersion liquid. The hydrodynamic radii (Rapp) is determined by fitting autocorrelation functions using REPES algorithms.

iii. *Characterization of iron carbon functionalized catalysts for synthetic gas conversion to hydrocarbons*

High resolution transmission electron microscopy (*HR-TEM*) images were obtained on a double-corrected Jeol ARM200F microscope equipped with a cold field emission gun utilizing a Gatan GIF Quantum. The acceleration voltage was set to 200kV. The particle size distribution (PSD) was calculated manually using Image J software.

A Zeiss Gemini Leo 1550 with oxford energy dispersive X-ray (*EDX*) detector of 80 mm² with 15 kV was used for scanning electron microscopy (*SEM*) investigations and determination of elemental compositions, respectively.

Nitrogen physisorption (*N_2-physisorption)* experiments were carried out at -196 °C on a Quantachrome Quadrasorb apparatus. Before starting the analysis samples were degassed at 150 °C for 20 h. Results were analyzed with the Quadra Win software (version 5.05). Pore size distributions (PSDs), specific surface areas (SSAs), total pore volumes (TPVs) up to 50 nm, and micropore volumes (MPVs) were calculated from isotherm analysis with the quenched solid density functional theory (QSDFT) method for nitrogen adsorbed on carbon with slit/cylindrical pores at -196 °C (adsorption branch kernel).

The Elemental analysis (*E.A.*) was carried out by combustion analysis in a Vario Micro device.

X- ray Photoelectron Spectroscopy (*XPS*) was performed by using a Thermo Scientific K-Alpha spectrometer equipped with a monochromatic small-spot X-ray source and a 180° double focusing hemispherical analyzer with a 128-channel delay line detector. An aluminum anode (AlK$^{\alpha}$ =1486.6 eV) operated at 72 W and a spot size of 400 μm is used to obtain the spectra. The measurement of the survey scans was at constant pass energy of 200 eV, and the measurement of high-resolution scans of the separate regions was done at 50 eV. The background pressure of the ultra-high vacuum (UHV) chamber was $2 \times 10{-8}$ mbar. No special precautions were considered to keep the sample under an inert atmosphere during catalyst transfer and handling. Sample charging was compensated for by the use of an electron flood gun, and binding energy calibration was done by setting the peak of graphitic sp^2 carbon to B.E.=284.0 eV.

Thermogravimetric analyses (**TGA**) were performed using a thermo microbalance TG 209 F1 Libra from Netzsch. The catalysts were measured using a platinum crucible of 10 ± 1 mg under synthetic air flow of 10 mL/min up to 1000 ° C with a heating rate of 5 K/min.

X-ray diffraction (**XRD**) experiments were carried out with a Bruker D8 diffractometer and with a CuK$^\alpha$ source (λ = 0.154 nm) and a Scintillation counter. The reference patterns were found in the ICDD PDF-4+ database (2014 edition).

Inductively coupled plasma-optical emission spectrometry (**ICP-OES**) was performed by using a SPECTRO ARCOS ICP-OES instrument after aqua regia extraction of the samples.

Raman spectra was obtained using a Renishaw inVia Raman Microscope operating with an objective (Nikon, 10x/0.25, ∞/− WD 6.1) and an excitation wavelength of 532 nm with a power of 4.0 mW. From the obtained Raman spectra the D and G bands were fitted with a Lorentz function.

e. Supporting information for chapter 4: research and outcomes

[S.I]   *Functionalized carbons as supports in liquid phase reaction: Nickel Nanoparticles Catalyst for Kraft Lignin Hydrogenolysis in Batch and Flow Reactions*
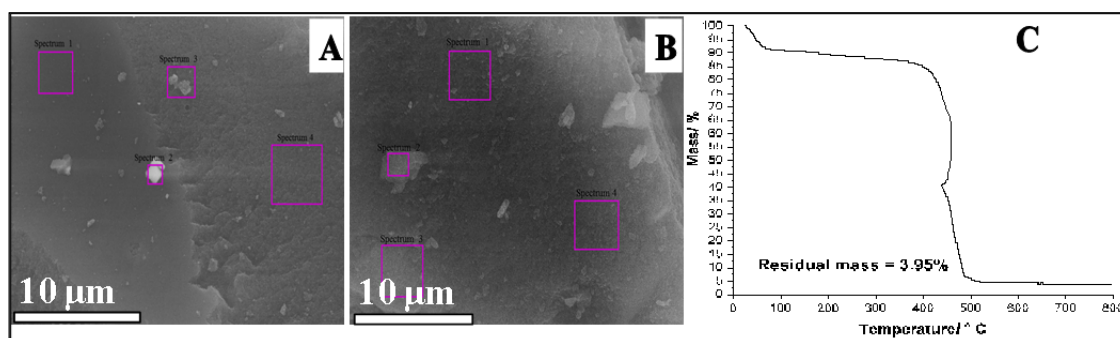
Figure S. 1: SEM-EDX images of NDC support unwashed (A) and washed (B) from the iron impurities and TGA for washed NDC (C)

Table S. 1: Elemental content in wt. % of Fe detected by SEM-EDX

Spectrum	Fe in unwashed NDC (wt. %)	Fe in washed NDC (wt. %)
1	15	0.8
2	51	0.6
3	12	0.9
4	10	0.6
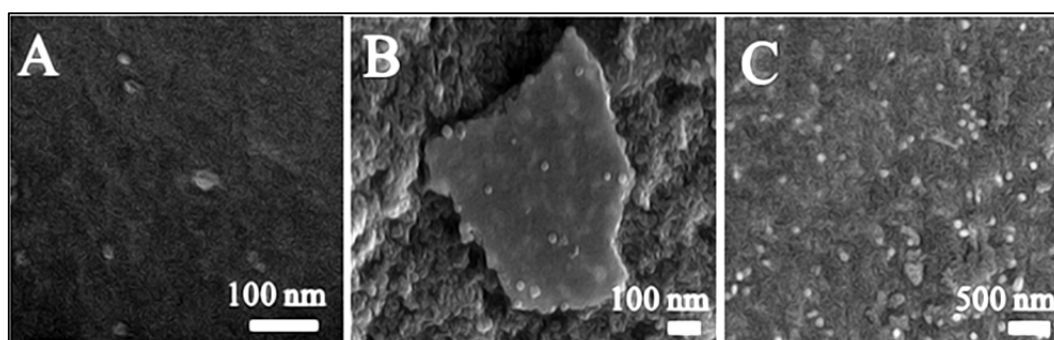
Figure S. 2: SEM images for 10 wt. % (A), 19 wt. % (B), and 32 wt. % (C) of pristine Ni-NDC catalyst
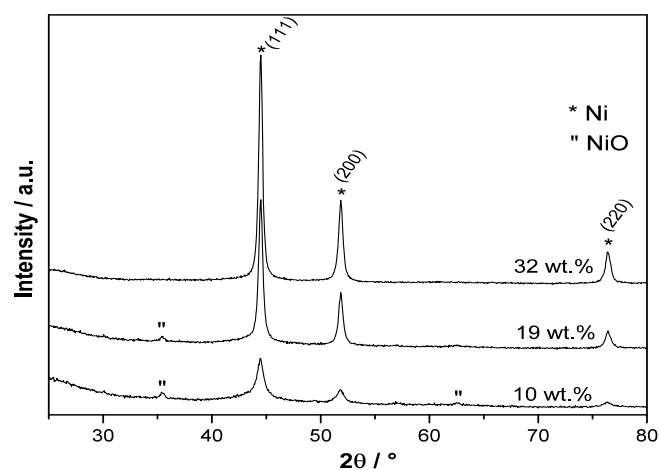
Figure S. 3: XRD analysis for 10 wt. %, 19 wt. %, and 32 wt. % of pristine Ni-NDC catalyst

Table S. 2: The ICDD # as given by Match software for detected compounds

Element	ICDD #
NiO	96-432-9324
Fe_2O_3	96-101-1241
Ni	00-004-0850
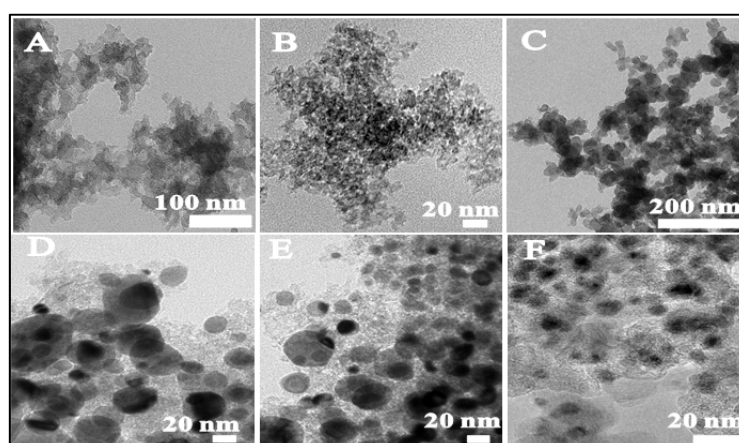
Figure S. 4: TEM images of carbon glucose support before (A) and after Ni deposition (D), carbon glucoseamine support before (B) and after Ni deposition (E), and carbon reference support before (C) and after Ni deposition (F)
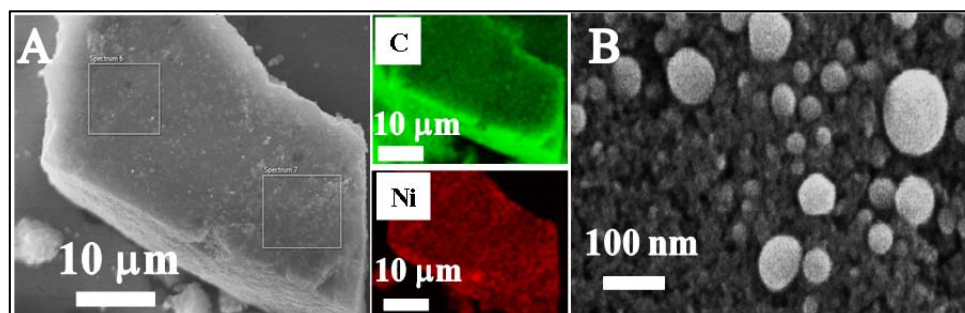
Figure S. 5: SEM-EDX (A) and SEM image (B) of pristine Ni-NDC
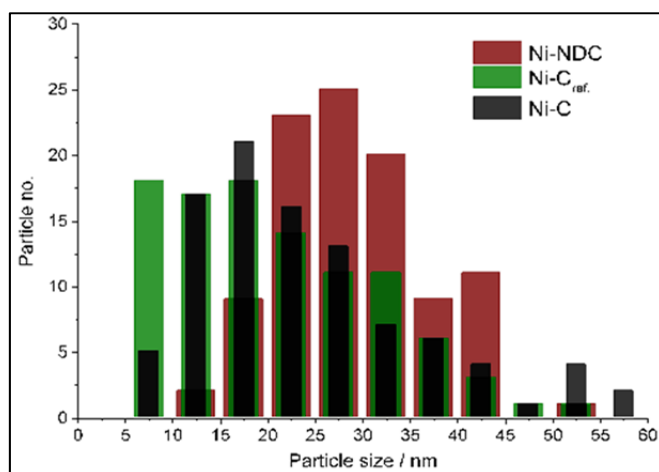
Figure S. 6: Average particle size distribution of pristine Ni-C catalysts
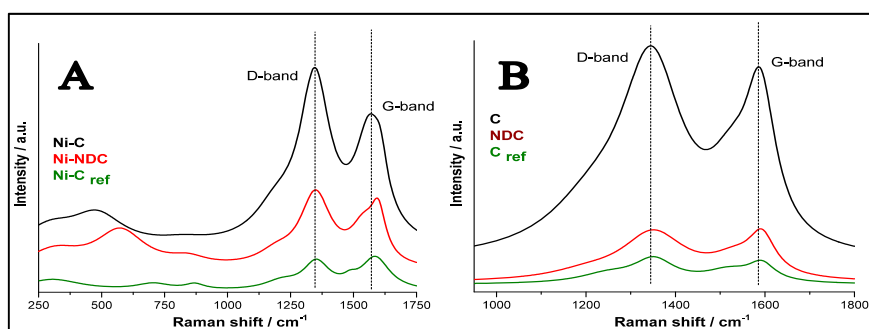
Figure S. 7: Sum of deconvoluted Raman results of the carbon supports before (A) and after (B) Ni deposition

Table S. 3: Raman data summary of carbon supports and Ni-C catalysts

	Ni-NDC	Ni-C	Ni-C $_{ref}$	NDC	C	C $_{ref}$
D-Band (cm^{-1})	1348	1348	1352	1351	1344	1351
G-Band (cm^{-1})	1593	1570	1586	1589	1591	1591
I_D:I_G	1.02	1.10	0.99	0.99	1.07	1.04
FWHM $_{D-band}$	151	162	139	178	183	123
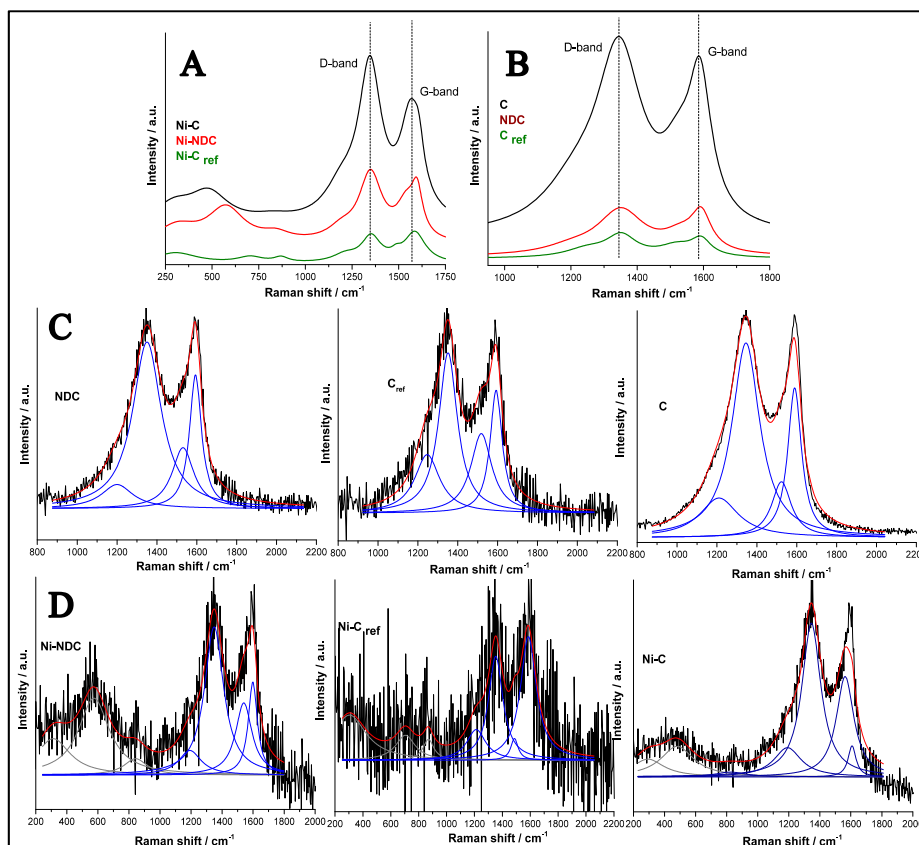
Figure S. 8: Deconvolution results of Raman spectra for carbon supports (B and C) and for Ni-C composites (A and D)
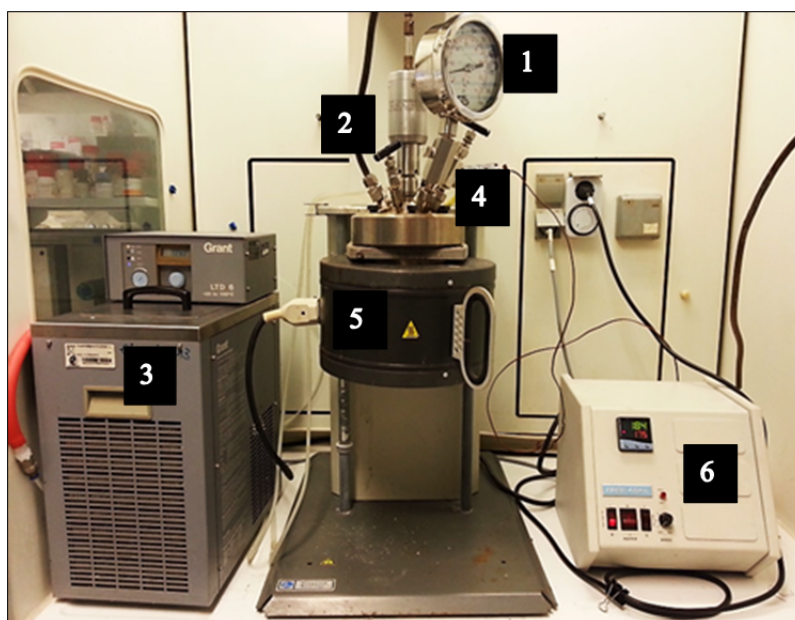
Figure S. 9: Representation of the batch system used for kraft lignin hydrogenolysis

Table S. 4: Parts of the batch system used for hydrogenolysis of kraft lignin

#	Parts
1	Pressure gauge
2	Metal stirrer
3	Cooling system
4	Autoclave
5	Heating mantel
6	Temperature system

The batch reactor is purchased from Parr instrument company series 4523 Bench top reactors, 1 L autoclave size, maximum pressure of 130 bar, and temperature up to 350 °C. To start a reaction, the autoclave is filled with the 2.5 g kraft lignin in 500 mL ethanol solution and 1 g catalyst. Then it is tightly closed and purged then filled with 8 bar hydrogen gas and heated with the heating mantel. The temperature system controls the degree of temperature and stirring speed where 150 ° C was the temperature applied and 500 rpm was the stirring speed. As the system heats up the pressure inside the reactor builds up and this is recorded by the pressure gauge which would normally reach ~ 22 bar. Finally, to maintain the stability of the reaction's temperature, the autoclave is connected to a cooling system. After 24 h the reaction is put off manually, left to cool, then the content of the autoclave is filtered and the liquid part is further treated with rotary vaporization system to obtain a concentrated product to analyze with GC-FID and GCxGC-MS. The solid phase collected from filtration is washed with excess of the solvent then dried and analyzed.
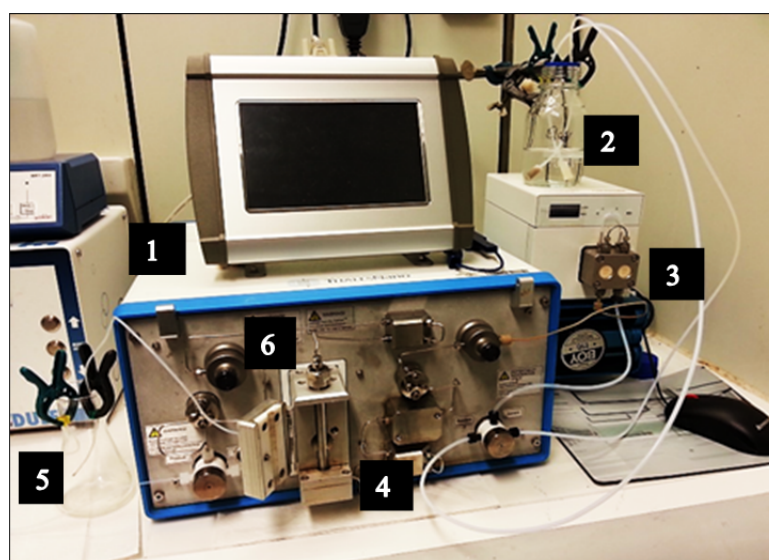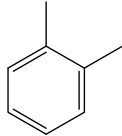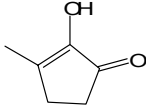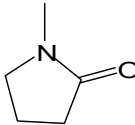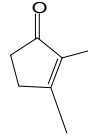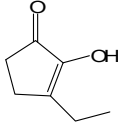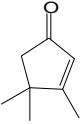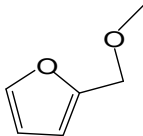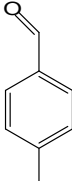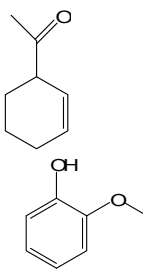
Figure S. 10: Representation of the flow system used for hydrogenolysis of kraft lignin
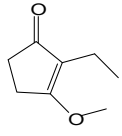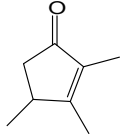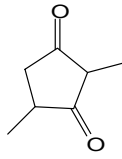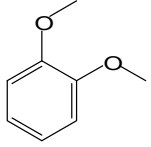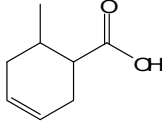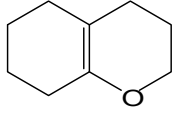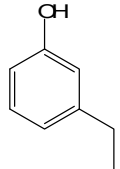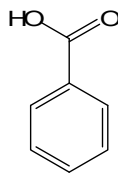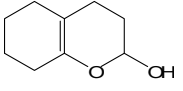
Table S. 5: Parts of the flow system used for hydrogenolysis of kraft lignin

#	Parts
1	Hydrogen cells
2	Educt vessel
3	HPLC pump
4	Fixed bed cartridge
5	Product vessel
6	Heating system

Specifications of the flow reactor: A commercial continuous fixed-bed set-up H-CUBE Pro[TM]. It can withstand a temperature up to 150 °C and a pressure up to 100 bar with flow rates ranging between 0.3 mL min^{-1} to 3 mL min^{-1}. The cartridge containing the catalyst is of 70 mm height and a diameter of 4 mm with one end sealed with 8 μm filter. The flow reactor is composed of an educt vessel, in which 2.5 g of lignin dissolved in 500 mL ethanol was added, and then with an HPLC pump the solution is impelled with 0.3 mL min^{-1} flow towards the 350 mg catalyst fixed bed cartridge. The catalyst chamber is heated to 150 °C through an inner heating system equipped in the device which is set via the screen. Also, the hydrogen pressure was set to ~ 25 bars and was provided by the hydrogen cells in the system. Afterwards, the product is collected in another vessel and later on being rotary vaporized and analyzed. Before the reaction, the catalyst would be purged with the solvent until the set conditions of the reaction are reached and the temperature and pressure are stabilized. As well as after the reaction the catalyst would be purged till system is cooled down.

Table S. 6: Compounds detected by GCxGC-MS in degraded kraft lignin samples

No.	Retention time	Molar mass	Compound
1.	13.085	106	
2.	18.197	112	
3.	18.209	99	
4.	18.646	110	
5.	19.393	126	
6.	19.543	124	
7.	19.995	112	
8.	20.112	120	
9.	20.444	124	
10.	20.446	124	

11.	20.891	140	
12.	21.190	138	
13.	21.345	126	
14.	22.097	138	
15.	22.392	140	
16.	22.541	138	
17.	22.993	122	
18.	22.996	122	
19.	23.593	154	
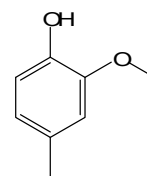
20.	23.745	138	
21.	24.296	134	
22.	24.496	120	
23.	25.091	168	
24.	25.694	136	
25.	26.295	152	
26.	27.049	168	
27.	27.197	150	
28.	27.345	166	
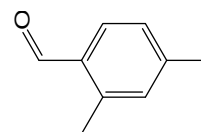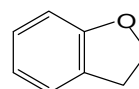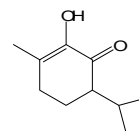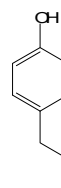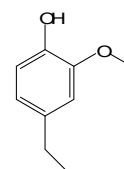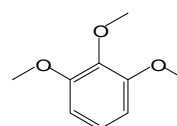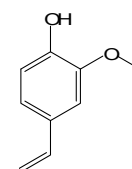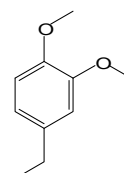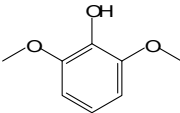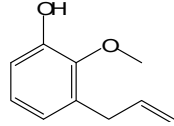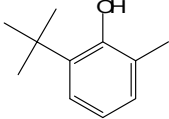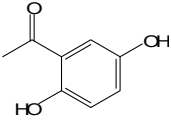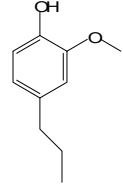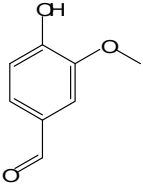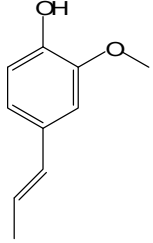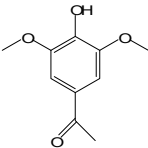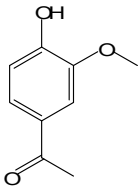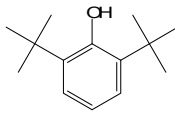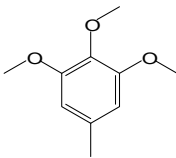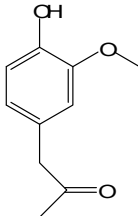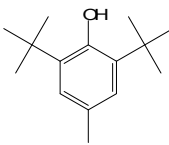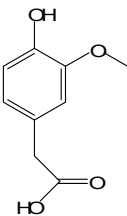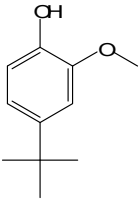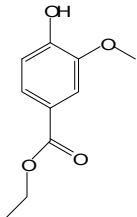
29.	27.953	154	
30.	28.545	164	
31.	28.692	164	
32.	28.697	152	
33.	28.844	166	
34.	29.158	152	
35.	30.797	164	
36.	31.397	196	

37.	31.555	166	
38.	32.591	206	
39.	32.599	182	
40.	32.605	180	
41.	32.740	220	
42.	33.051	182	
43.	33.498	180	
44.	33.952	196	
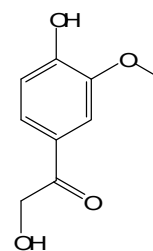
45.	33.954	182	
46.	34.408	186	
47.	35.153	210	
48.	35.305	182	
49.	35.455	182	
50.	35.910	196	
51.	36.961	196	
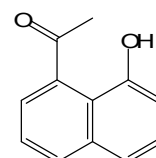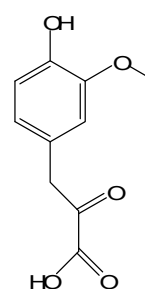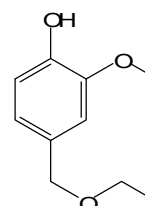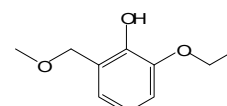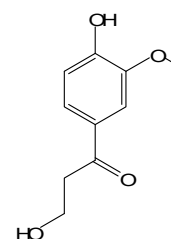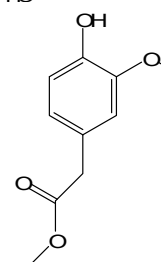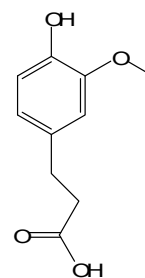
52.	37.257	196	
53.	39.506	198	
52.	39.660	212	
54.	41.324	210	
55.	41.471	234	
56.	41.762	216	
57.	41.900	278	
58.	43.126	210	
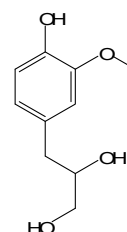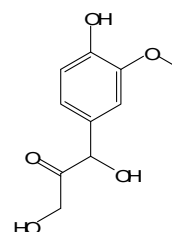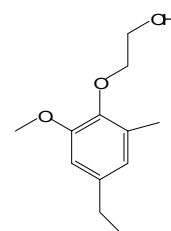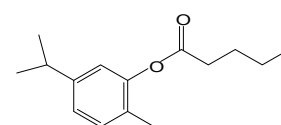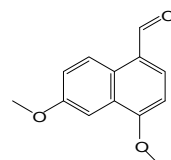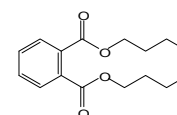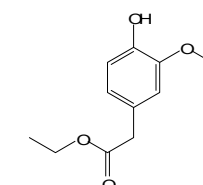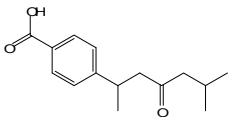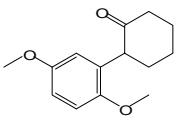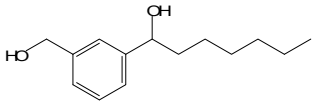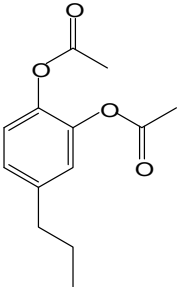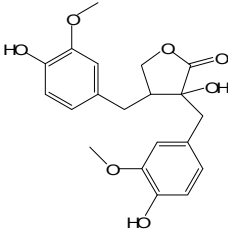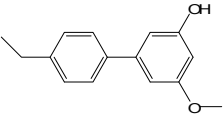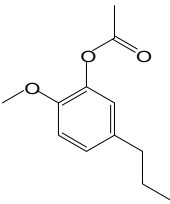
59.	43.701	248	
60.	43.714	234	
61.	44.021	222	
62.	44.777	236	
63.	46.412	374	
64.	46.720	228	
65.	47.917	208	

Table S. 7: Content of Ni in pristine and spent catalysts, and in the degraded lignin product

	Sample	Ni (ppm) ICP
Degraded lignin-product of a reaction with:	Ni-C ref Batch	798
	Ni-C Batch	625
	Ni-C Flow	12
	Ni-NDC Batch	865
	Ni-NDC Flow	8.3
Catalyst	Fresh Catalyst	327750
	Ni-NDC Flow	273393
	Ni-NDC Batch	110263
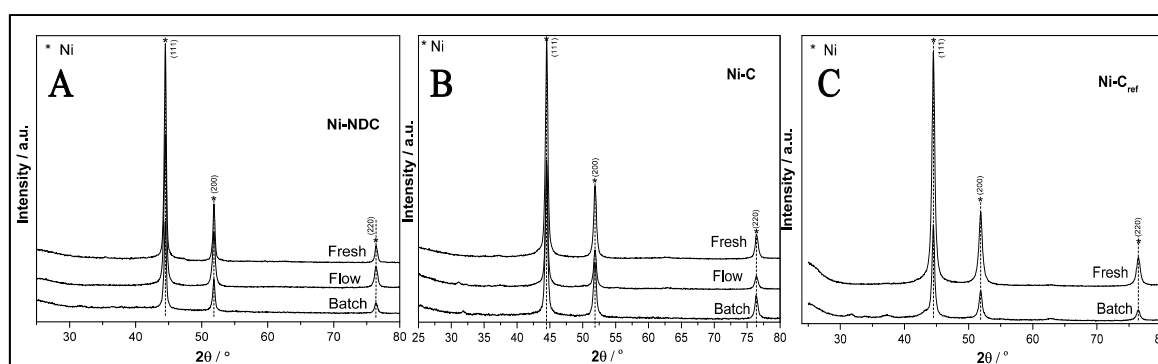
Figure S. 11: XRD measurement for pristine catalyst, after flow reaction, and after batch reaction for Ni-NDC (A), Ni-C (B), and Ni-C ref (C)

Table S. 8: Elemental analysis of Ni-NDC before and after degradation reaction

Sample Ni-NDC	N/C (Wt. %)$_{E.A.}$	N:C
NDC	3/80	0.04
After flow	2/51	0.04
After batch	1/50	0.02
Fresh Ni-NDC	2/50	0.04
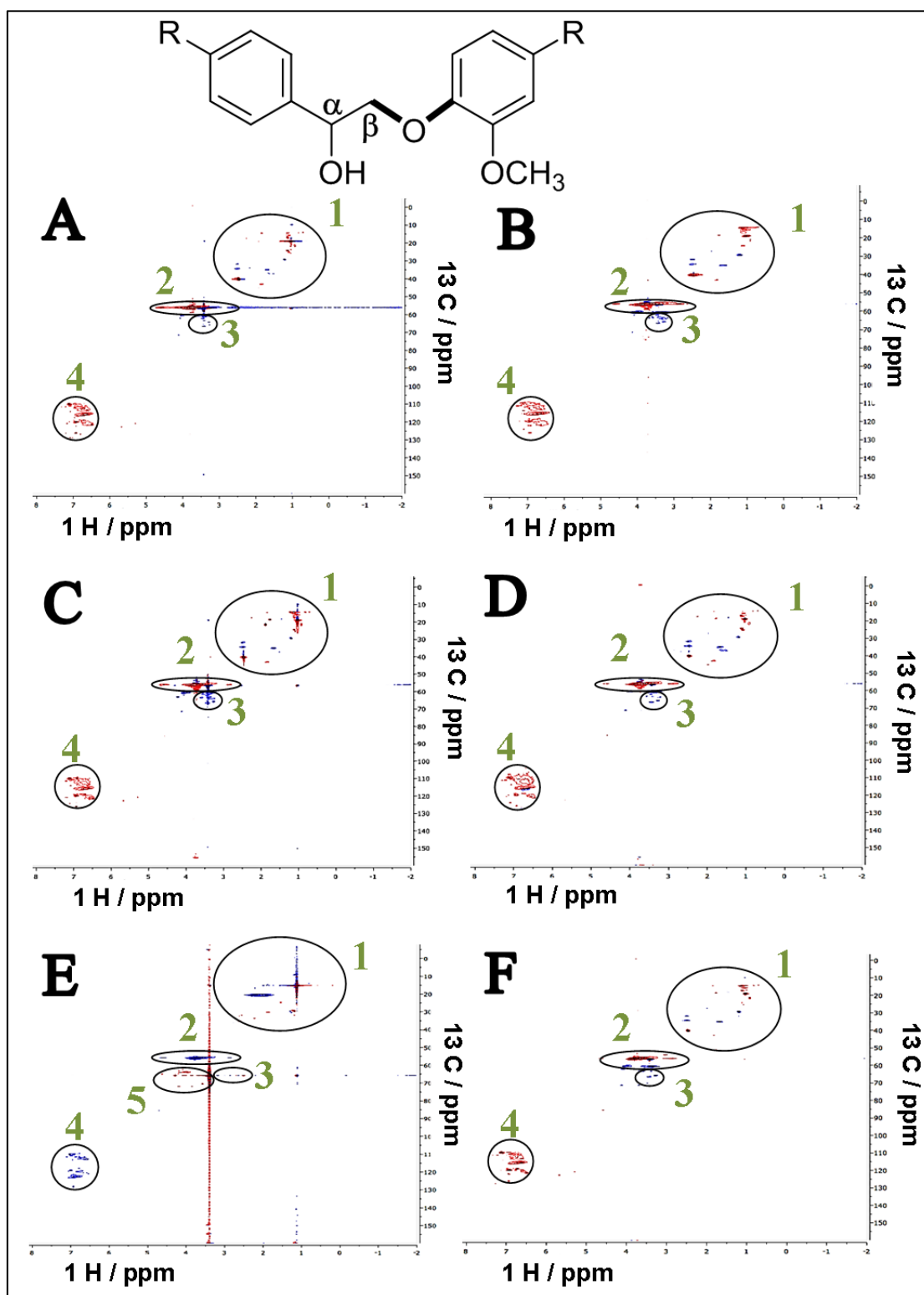
Figure S. 12: ^{13}C vs. ^{1}H 2D-NMR of kraft lignin pristine (E) and the flow and batch degradation of lignin of Ni-NDC (A and B), Ni-C (C and D) respectively, and the batch reaction of Ni-C ref (F)

Table S. 9: Detected functional groups by 2D-NMR (13C vs. 1H)

#	1	2	3	4	5
Functional groups	Aliphatics	Methoxy	γ-CH$_2$	Aromatics	β-aryl ether (β-O-4)

Table S. 10: Summary of characteristics of Ni-C composites after flow and batch reactions

	SSA (m^2/g)	TPV (mL/g)	N/C (wt.%) $_{E.A.}$	Ni particle size (nm)$_{TEM}$	Kraft lignin mass balance (%)
Ni -NDC flow (50hrs)	225	0.42	2/51	20	99
NDC-Ni batch	13	0.05	1/54	24	57
Ni-C$_{ref}$ flow	The porosity of this catalyst caused a high pressure and blockage when a flow of lignin solution was treated for degradation via catalytic hydrogenation system; therefore no flow reaction took place				
Ni-C$_{ref}$ batch	27	0.06	0.3/59	15	73
Ni-C flow (25hrs)	236	0.46	0.6/57	38	99
Ni-C batch	62	0.17	1/56	50	54

Table S. 11: Size exclusion chromatography/ Gel permeation chromatography data (SEC/GPC) for pristine and degraded kraft lignin via the different Ni-C composites

	DETECTOR					
	UV-1000-270nm			Shodex RI-71		
	Mn (g mol^{-1})	Mw (g mol^{-1})	Mz (g mol^{-1})	Mn (g mol^{-1})	Mw (g mol^{-1})	Mz (g mol^{-1})
Kraft lignin	716	3307	10123	1023	3684	11275
Ni-NDC Flow	672	1299	2018	830	1423	2307
Ni-NDC Batch	773	1537	2555	927	1703	2857
Ni-C Flow	623	1149	1846	783	1265	1997
Ni-C Batch	776	1082	1578	883	1568	2657
Ni-C$_{ref.}$ Batch	596	1918	3756	1118	2290	4176
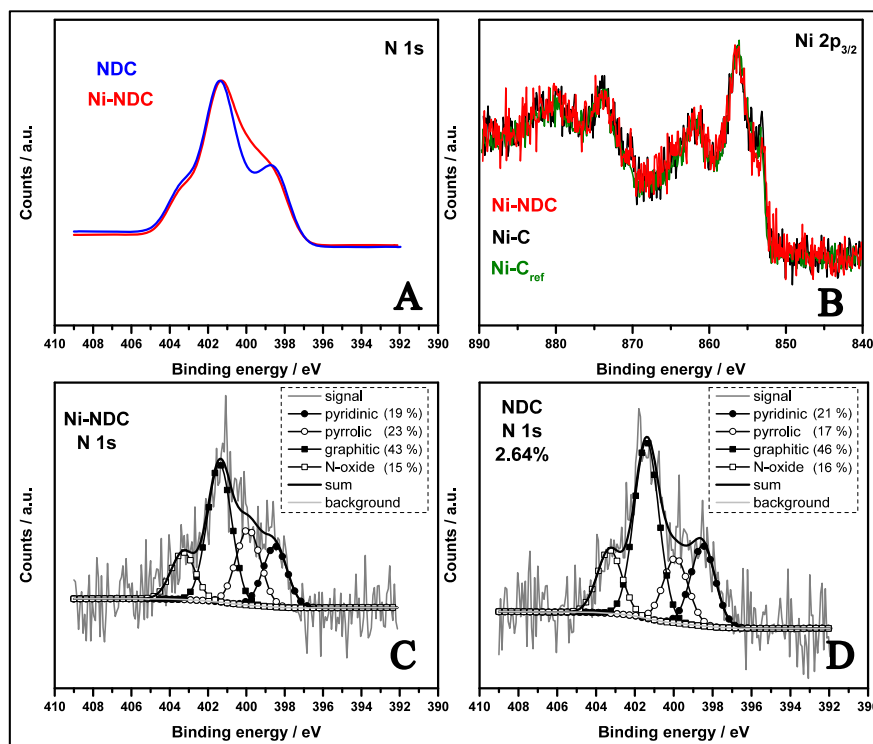
Figure S. 13: X-ray photoemission spectroscopy for Ni-NDC and NDC (A), detection of Ni 2p$_{3/2}$ for Ni-C composites (B), N 1s in Ni-NDC (C) and NDC (D)

Table S. 12: Summary of the XPS data for NDC support and the Ni-C composites

Sample	XPS / at.% N/C/O/Ni
NDC	3/89/5/-
Ni-NDC	3/86/8/2
Ni-C	-/88/7/2
Ni-C ref.	-/88/8/3
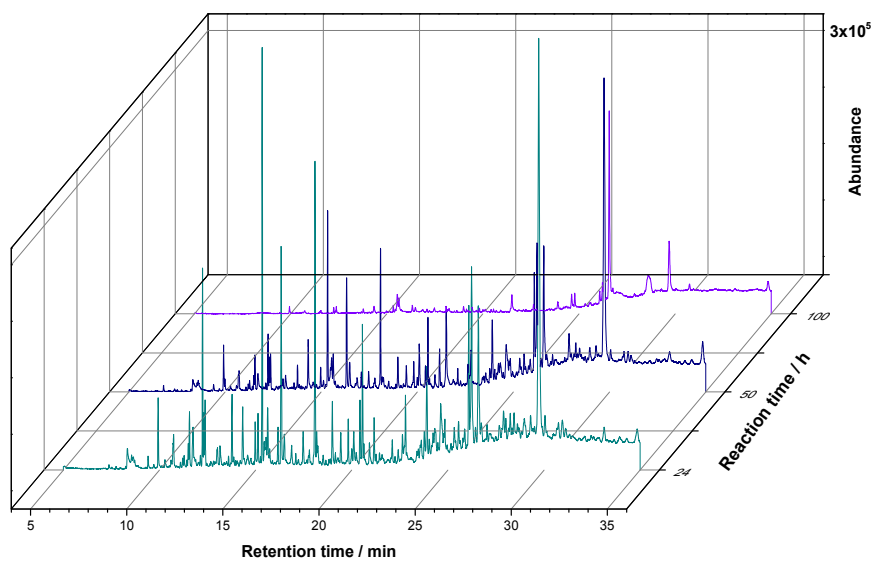
Figure S. 14: Stability test for Ni-NDC in flow system up to 100 h

[S.II] Functionalized carbons as Supports in Aqueous Phase Reaction: Gold Nanoparticles Catalyst for Selective Glucose Oxidation

a. Comparison of Au–C_{Glucoseamine} to different systems under different preparation and reaction conditions

The decision of using 1 wt.% of Au metal deposited on salt-melt carbons via pre-reduced nanoparticles is made after comparing Au metal to commercial noble metal Pd; known to be active for oxidation of glucose. Also after comparing salt-melt carbon to a e commercial SiO_2 support. In addition, a comparison to the deposition method has been tested between a pre-reduced method and IWI method, and looking into the different weight percentage of the deposited metal (1 wt. % vs. 5 wt. %).

First, Pd (using Palladium chloride ($PdCl_2$) as precursor) and Au were deposited in a 5 wt. % on $C_{Glucoseamine}$ via IWI method (according to the pore volume of the carbon support the aqueous solvent D.W. was added to the precursor to dissolve it prior to deposition, in case of Pd precursor ethanol was used as the solvent because $PdCl_2$ is insoluble in D.W). The calcination of the catalysts of course proceeded where Pd-$C_{Glucoseamine}$ was heated up to 450 °C for 3 h at a 3 °C/min rate with 5% Hydrogen/ Argon flow. In the case of Au-$C_{Glucoseamine}$ the calcination was at 200 °C for 2 h at a 3 °C/min rate with 5% Hydrogen/ Argon flow. After the preparation of the catalysts, they have been tested via the titration system described in (*Figure S. 15*). The results showed Au-$C_{Glucoseamine}$ catalyst to have clearly higher activity than Pd-$C_{Glucoseamine}$ towards glucose conversion (Metal time yield of 7.6 x 10^{-4} mole $_{Glucose}$/ mole $_{Au}$/ s) which is in consistence to literature.
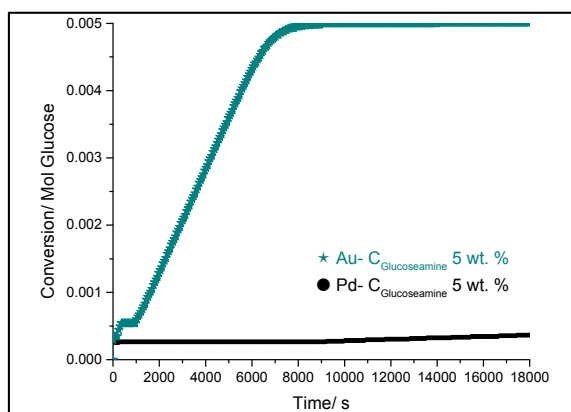
Figure S. 15: Titration results of 0.1 M D-glucose oxidation for 5 wt. % Pd-C_{Glucoseamine} and Au-C_{Glucoseamine}

As a result the Au was considered for this study. Later, different deposition methods were made to check for better Au nano particle size and distribution considering its

economic value as well. Therefore, IWI and pre-reduced Au nanoparticle methods were applied for the preparation of Au-C$_{Glucoseamine}$. At the same time, the synthesis was made in different mass percentage of 1 wt. % and 5 wt. %. The TEM images and the particle size distribution (Figure S. 16) provide that both methods has well distributed Au NPs in an average nanoparticle sizes ~ 6 nm out of 100 particle diameter count. However, the pre-reduced Au nanoparticle method provides an immediate reduction of Au nanoparticles with more controlled size by the stabilizer used, aside from the fact that a large batch can be produced and used for several preparations of catalysts at once which by that reduces the time of work. For these advantages, the pre-reduced Au nanoparticle method was considered. In addition, the less mass percent 1 wt. % has a good distribution of Au nanoparticles (Au NPs) on the carbon surface as that of the 5 wt. %. Moreover, after a titration test for the 0.1M D-glucose conversion to D-gluconic acid, the MTY of the 1 wt. % is higher than that of 5 wt. % when considering a range of glucose conversion between 0.002 mol and 0.004 mol (MTY of 1 wt. % Au: 0.8 mole $_{Glucose}$/ mole $_{Au}$/ s and MTY of 5 wt. % Au: 7.6 x 10^{-4} mole $_{Glucose}$/ mole $_{Au}$/ s) (Figure S. 17). Therefore, for the mentioned reasons besides the fact that 1 wt. % is more economic, the 1 wt. % Au NP-C was considered for the catalysts preparation.
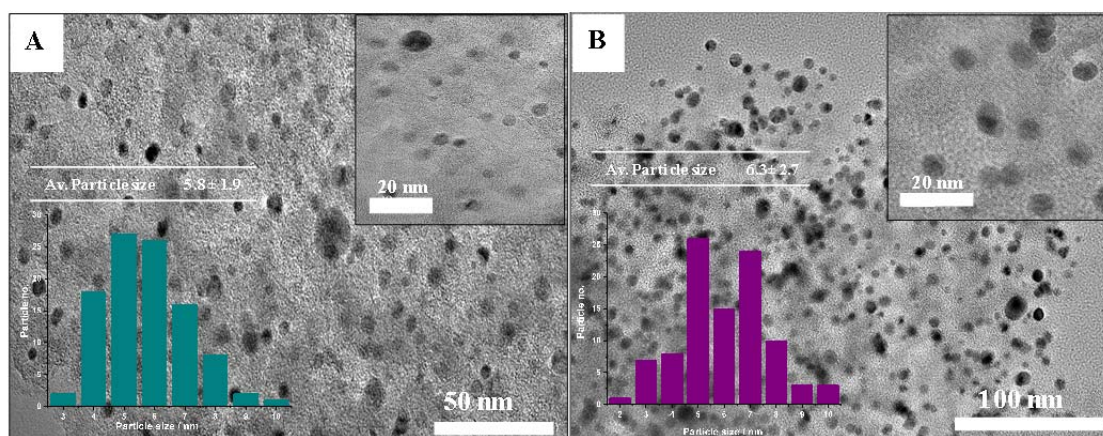
Figure S. 16: TEM imaging of IWI synthesized Au – C $_{Glucoseamine}$ 5 wt.% (A) and pre-reduced synthesized AuNP – C $_{Glucoseamine}$ 1 wt.% (B).
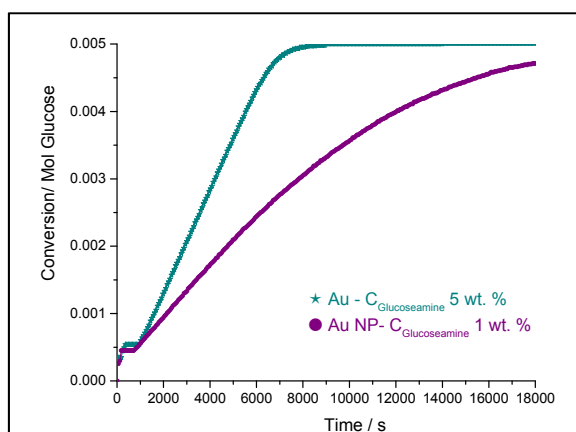
Figure S. 17: Glucose conversion via IWI (5 wt. %) and pre-reduced (1 wt. %) Au -
C Glucoseamine

Furthermore, the 1 wt. % Au NP-$C_{Glucoseamine}$ as a support was compared to commercial silica support (SiO_2) as shown in (Figure S. 18). The investigation of such a comparison was concluded via testing the different supported catalysts performance in converting 0.1 M D-glucose to D-gluconic acid. Knowing that all catalysts were synthesized using the same method of preparation (pre-reduced 1 wt. % Au NPs) the titration result revealed the activity of $C_{Glucoseamine}$ to be higher than SiO_2 support. This slight inspection is further investigated in a master study collaborating to similar research project. The study utilizes several commercial supports (TiO_2, SiO_2, Al_2O_3, and others) and compares them to carbon by depositing 1 wt. % Au NP and tests them for D-glucose conversion to D-gluconic acid. Their conclusion was that carbons have higher surface area that allows better deposition of Au NPs and thus better activity. Hence, the carbon was considered as the support for the heteroatom effect inspection.
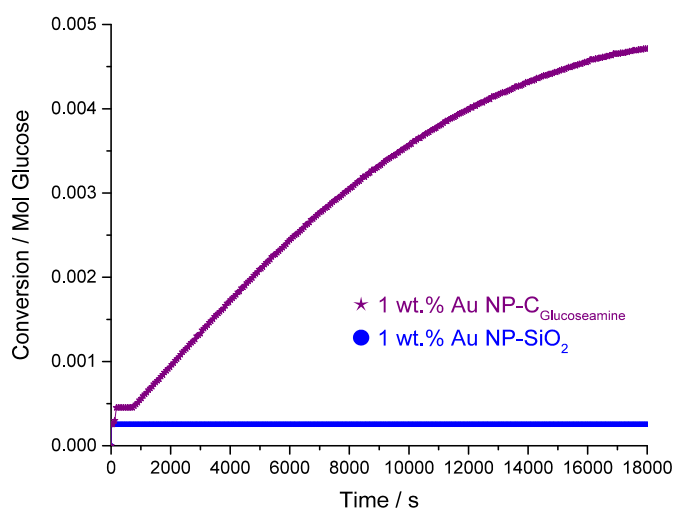
Figure S. 18: comparison between carbon support and SiO_2 support for synthesis of
Au NP catalysts and their activity in glucose conversion

b. *Extra supporting data*
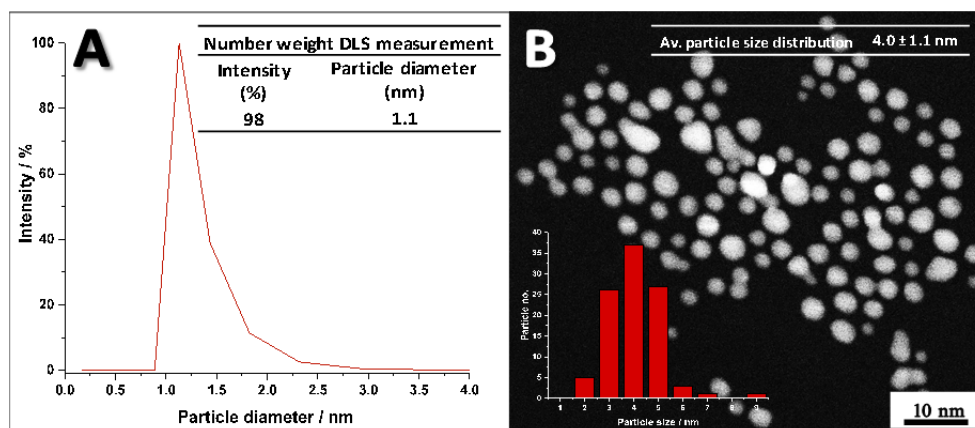
Figure S. 19: DLS measurement of pre-reduced Au NPs in solution (A) and TEM image and particle size distribution of Au NP after air-drying from pre-reduced solution (B) both before deposition on a support
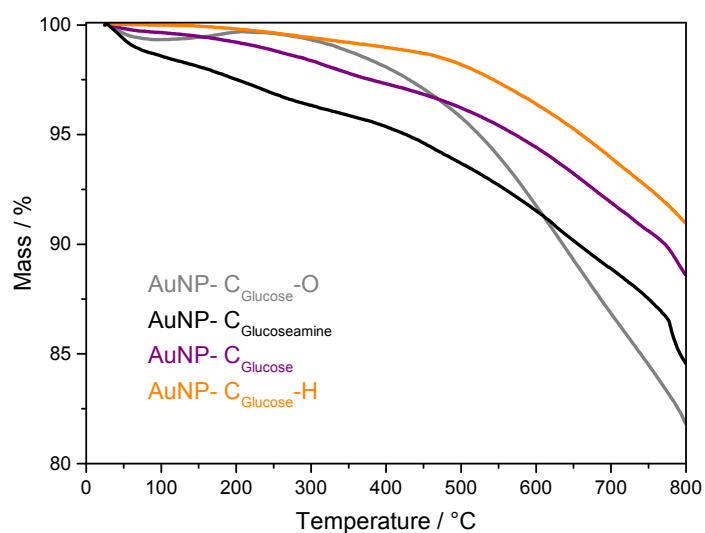
Figure S.20: Thermogravimetric analysis (TGA) of Au-C catalysts under nitrogen flow at a heating rate of 10 K. min^{-1}

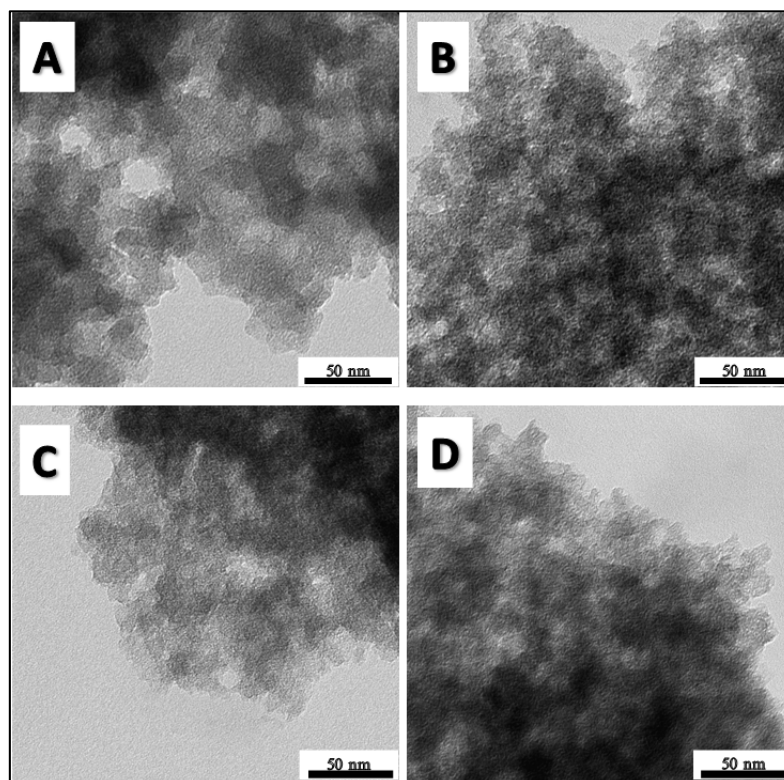*Figure S.21: TEM images of as-made $C_{Glucose}$ (A), $C_{Glucose}$-H (B), $C_{Glucose}$-O (C), and $C_{Glucoseamine}$ (D)*
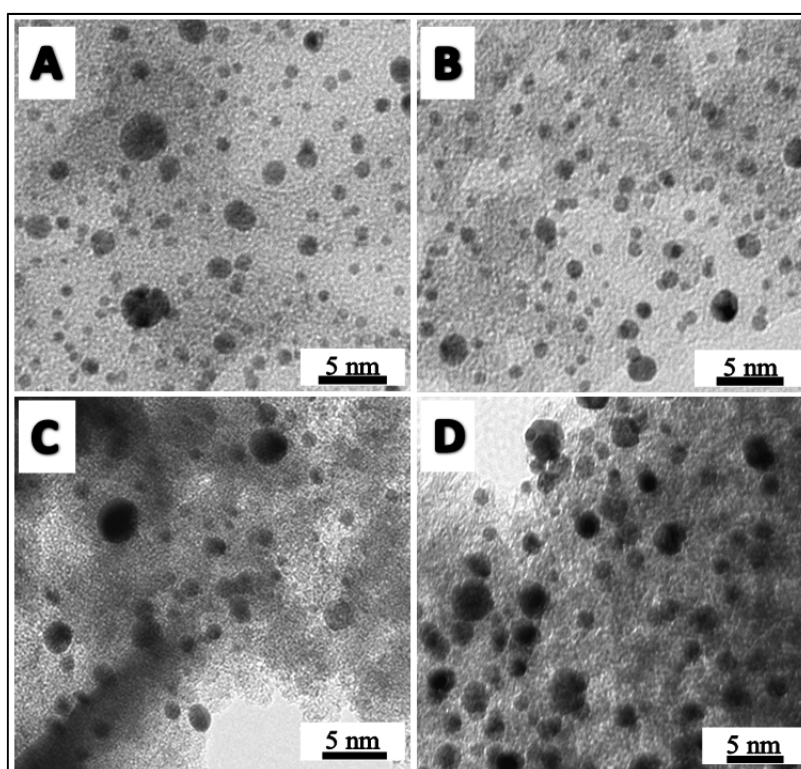
Figure S. 22: extra TEM images of pristine catalysts $Au–C_{glucose}$ – H (A,) $Au–C_{glucose}$ (B), $Au–C_{glucose}$ – O (C) and, $Au–C_{glucoseamine}$ (D)
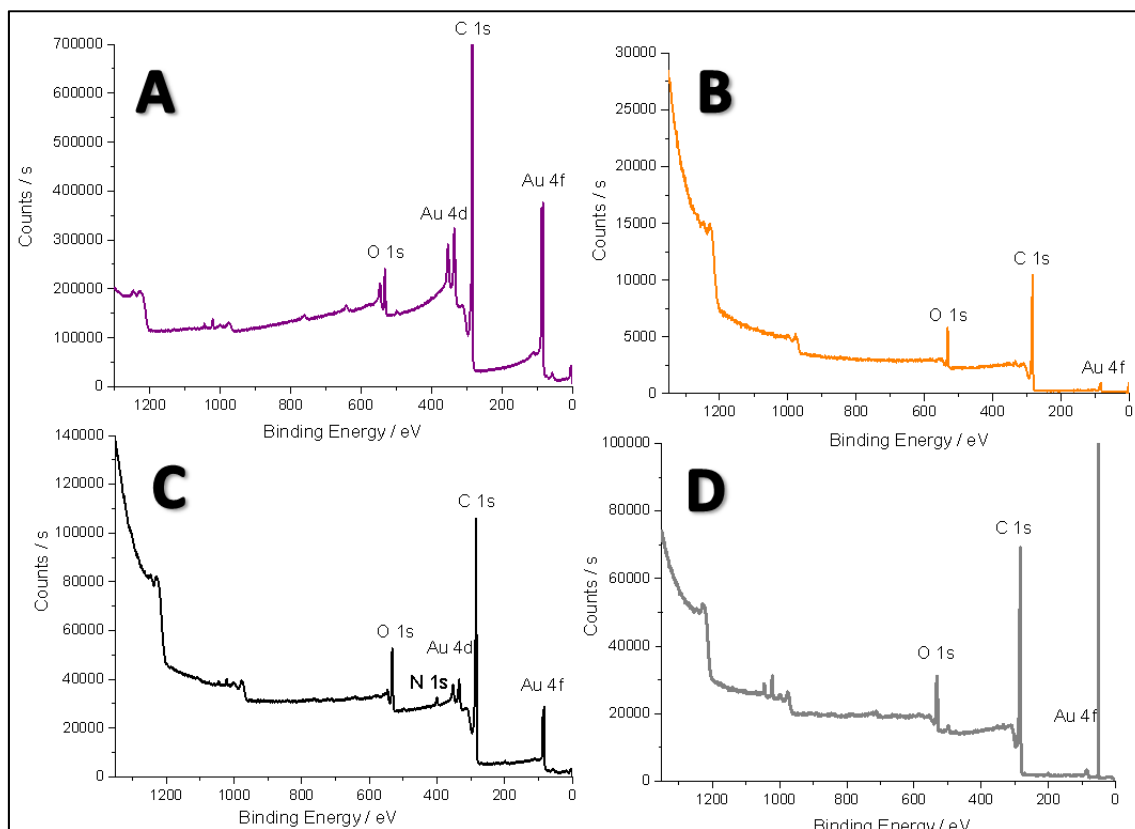
Figure S. 23: X-ray photoelectron spectroscopy survey scans of the surfaces of Au-C$_{Glucose}$ (A), Au-C$_{Glucose}$-H (B), Au- C$_{Glucoseamine}$ (C), and Au- C$_{Glucose}$-O (D)
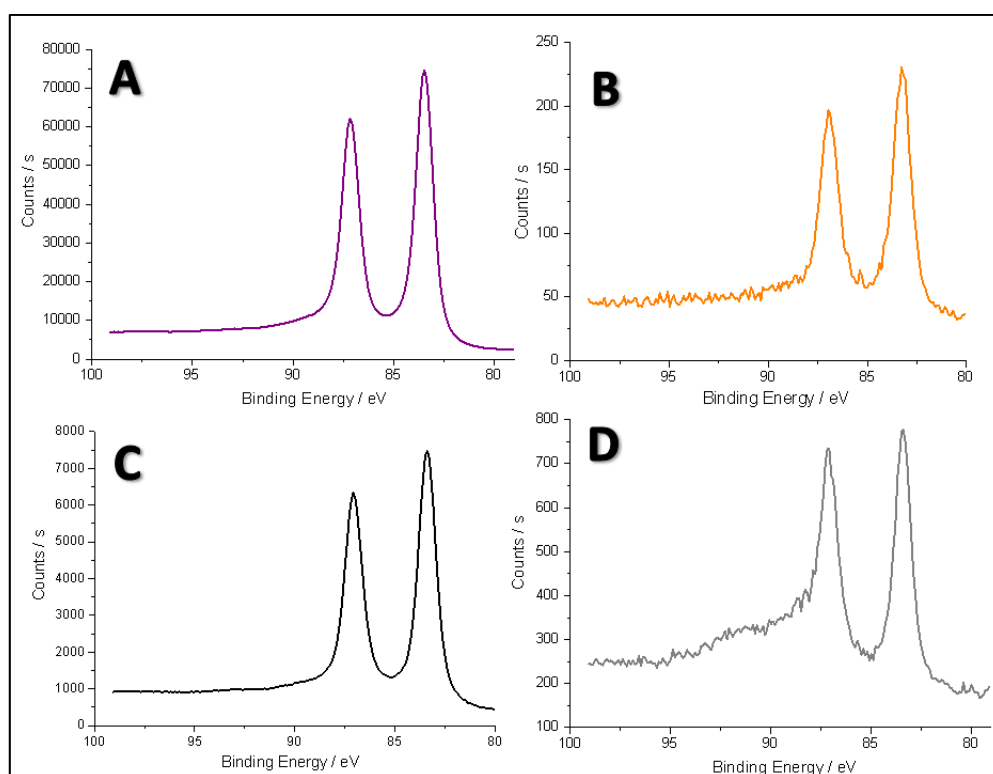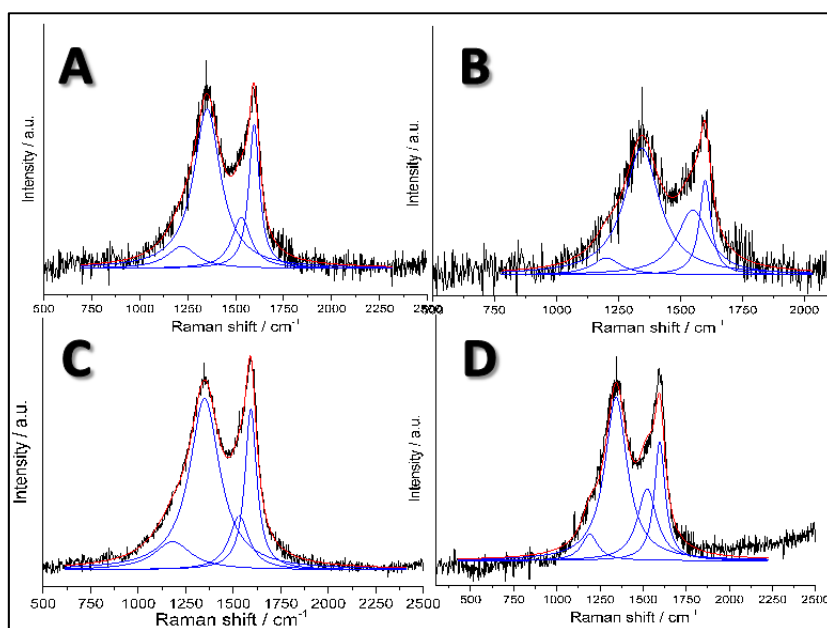

Figure S. 24: X-ray photoelectron spectroscopy (Au4f) line scans of the surfaces of Au-C$_{Glucose}$ (A), Au-C$_{Glucose}$-H (B), Au-C$_{Glucoseamine}$ (C), and Au-C$_{Glucose}$-O (D)

Figure S. 25: Raman spectroscopy of D- and G- bands of te carbon structure of Au-C$_{Glucoseamine}$ (A), Au-C$_{Glucose}$-O (B), Au-C$_{Glucose}$ (C), and Au-C$_{Glucose}$-H (D)

Table S. 13: Summary of the D- and G- bands intensities and the full width at half maxima for Au-C catalysts

Sample	I$_D$/I$_G$	FWHM$_{D\text{-Band}}$
Au-C$_{Glucose}$	1.03	186
Au-C$_{Glucose}$-H	1.13	150
Au-C$_{Glucose}$-O	1.06	168
Au-C$_{Glucoseamine}$	1.04	167
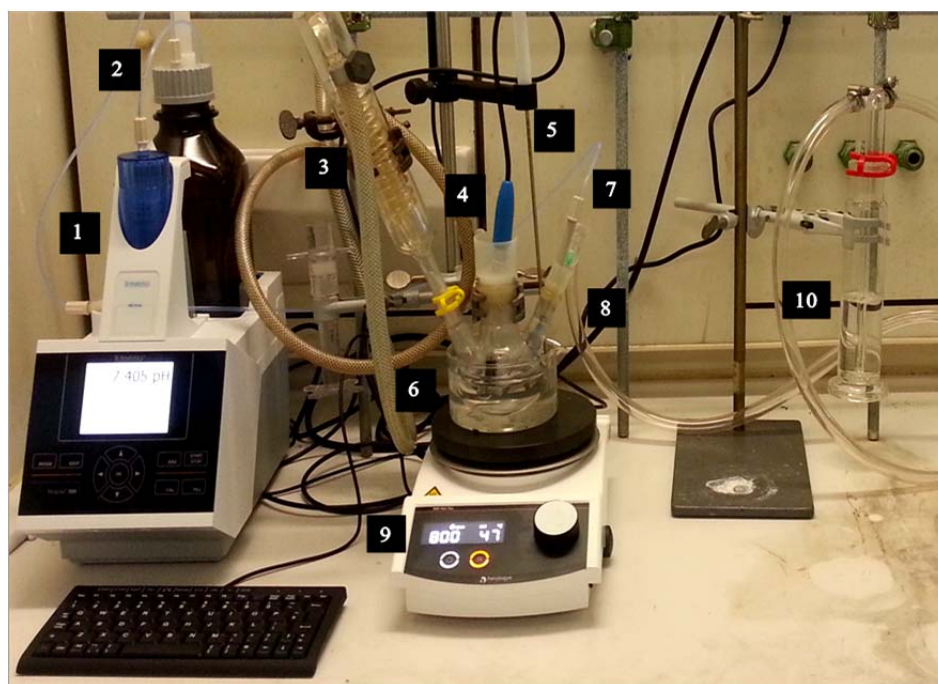
Figure S. 26: Automatic titration system and glucose oxidation setup

Table S. 14: Automatic titration system and oxidation setup parts

#	Parts
1	Automatic titration system
2	NaOH
3	Cooling system
4	pH meter
5	Thermometer
6	Reaction flask
7	Titration syringe
8	Oxygen flow
9	Heating and stirring control
10	Oxygen flow trap

The automatic titration system equipped with the oxidation setup as in (*Figure S. 26*) was used for the conversion of glucose to gluconic acid. The titration system parameters were set to pH = 9, heating temperature of 45 °C, and stirring speed of 800 rpm. The device is equipped with a 1 M standard aqueous sodium hydroxide (NaOH) used in the titration to equilibrate the mixture during the reaction of forming gluconic acid. Then an oxygen flow line is also connected to provide the oxidizing agent to the reaction. An oxygen flow trap is set to observe the flow speed of the oxygen. Two syringes are used: one to provide the oxygen flow and the other to provide the aqueous NaOH to equilibrate the reaction. Of course, a cooling system and a thermometer are added to the reaction setup. Then, the pH meter which measures the pH of the reaction during gluconic acid formation and addition of the base volume. In the three bottle neck flask, 50 mL of 0.1 M Glucose in distilled water solution is added and heated. When the parameters set are reached, 50 mg of 1 wt. % Au – C catalyst is added and the change in the pH is moderated automatically with a certain volume of the standard base solution. The pH and the volume can be recorded up to 5 h. The flask is immersed in an oil bath for better heating and temperature is controlled via the thermometer.
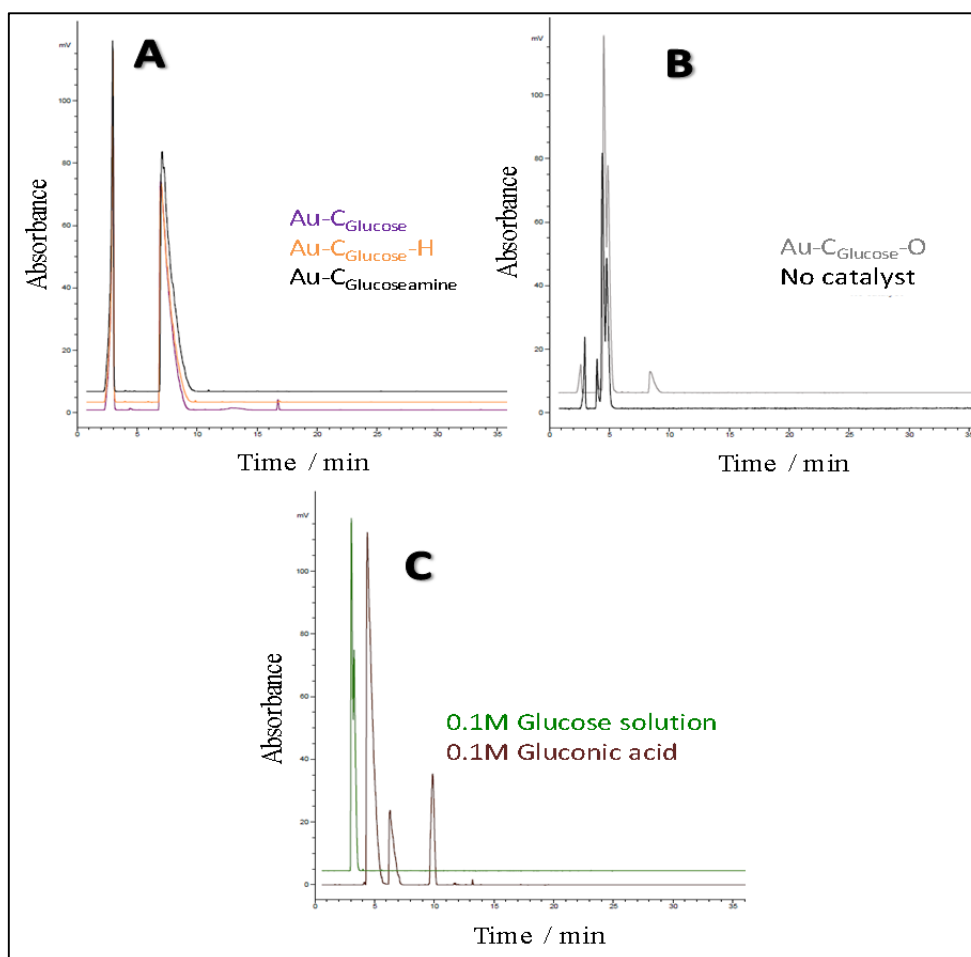
Figure S. 27: HPLC results of the reaction solutions of Au-C$_{Glucose}$, Au-C$_{Glucose}$-H, and Au-C$_{Glucoseamine}$ (A). HPLC results of Au-C$_{Glucose}$-O vs. reaction without catalyst (B). HPLC results of standards in aqueous solution: 0.1 M gluconic acid solution and 0.1 M glucose solution (C)
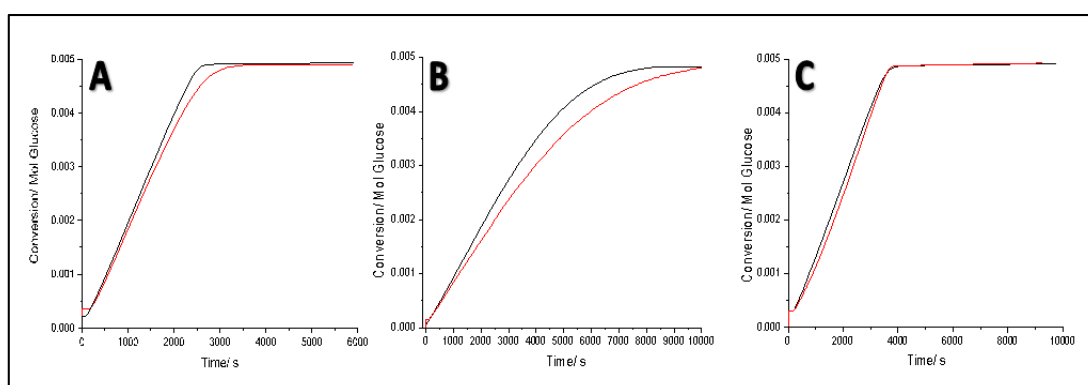

Figure S. 28: Stability test of Au-C$_{Glucose}$ (A), Au-C$_{Glucosamine}$ (B), Au-C$_{Glucose}$-H (C) for glucose conversion in a first (black curve) and a second (red curve) catalytic cycle

[S.III]   ***Functionalized Carbons as Supports in Gas Phase Reaction: Iron Nanoparticle Catalysts for Selective Lower Olefins Production from Syngas via Fischer Tropsch Synthesis***
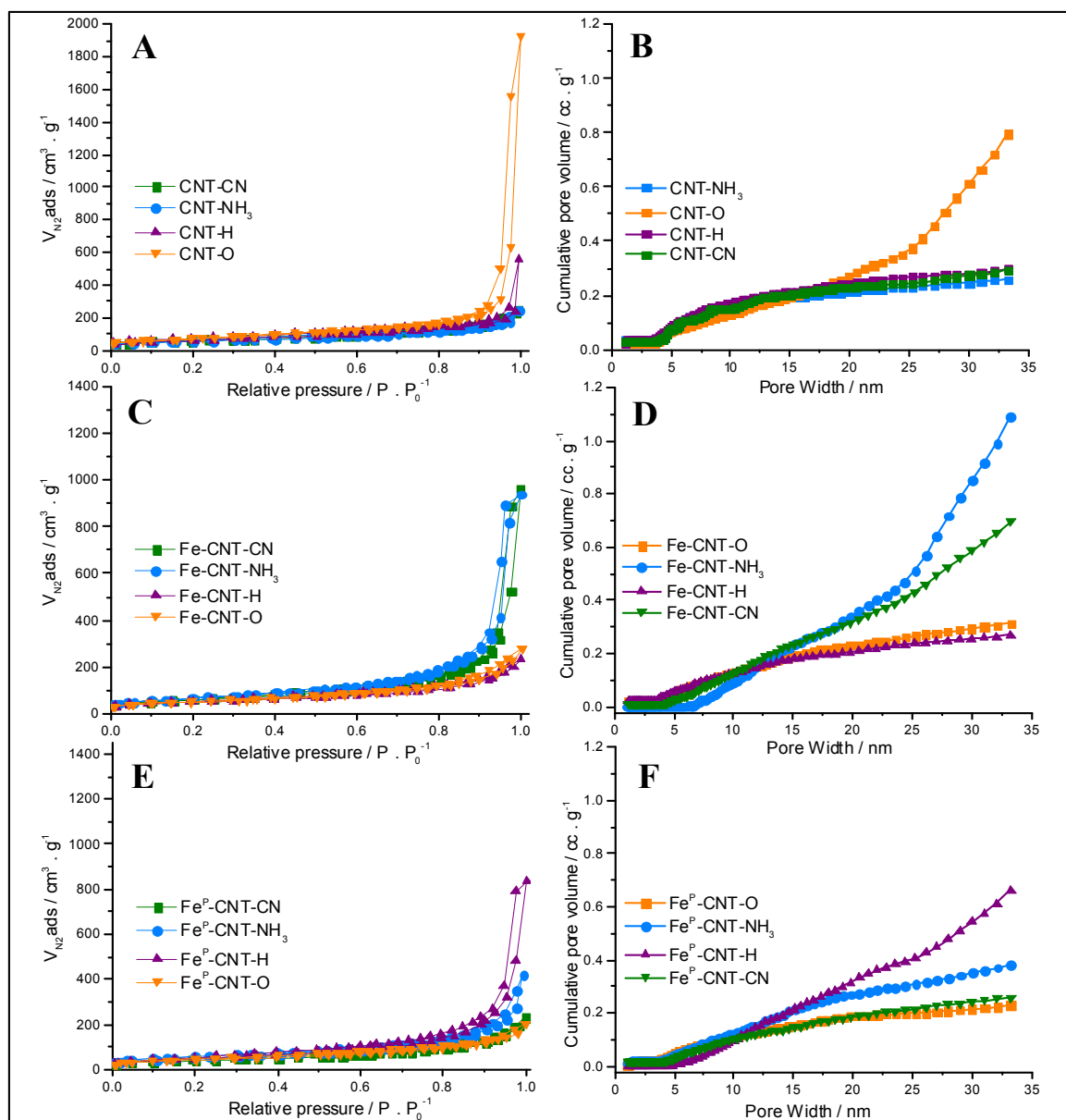
Figure S. 29: N_2- physisorption for specific surface area (SSA) and total pore volume (TPV) in the supports (A, B), pristine unpromoted catalysts (C, D) and pristine promoted catalysts (E, F).

Table S. 15: XRD of detected 2θ peak and, the planes peaks for CNTs-X supports and Fe-CNTs-X catalysts

2Θ (MWCNT)	h, k, l (MWCNT)	2Θ (Fe)	h, k, l (Fe)
25.8	002	24	012
43	101	30.3	104
53.6	100	35.6	110
		51.1	024
		57.2	122
		59.5	018
		63	214
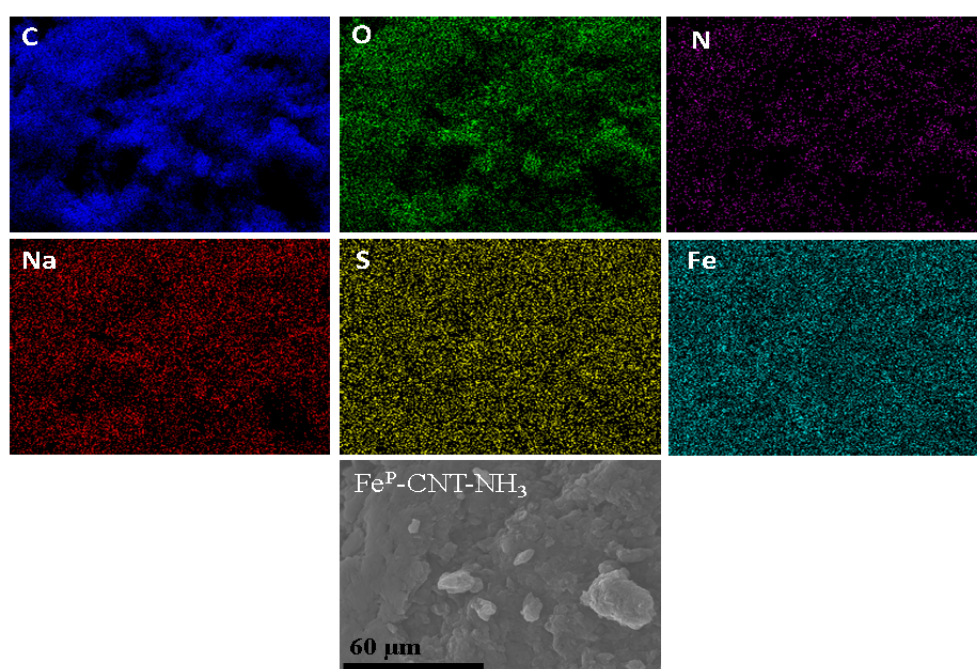
Figure S. 30: SEM-EDX mapping of Fe^P-CNT-NH$_3$
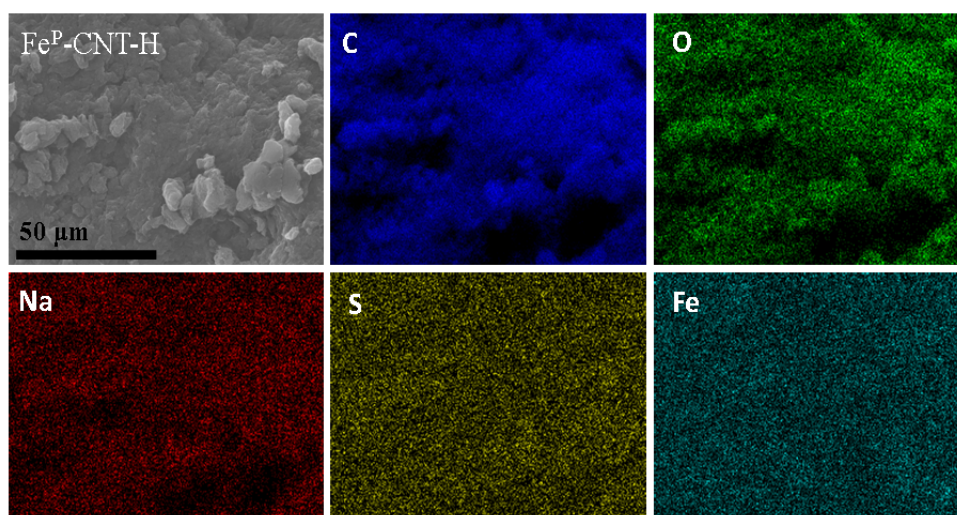
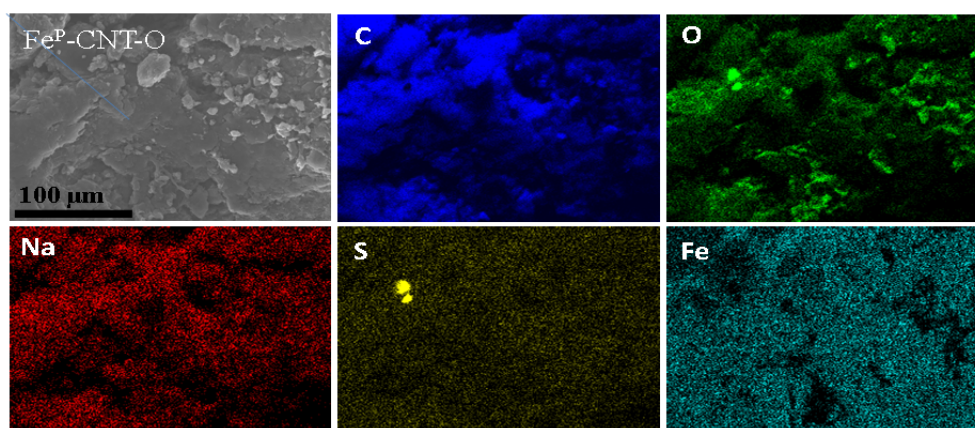*Figure S. 31: SEM-EDX mapping of Fe^P-CNT-H*
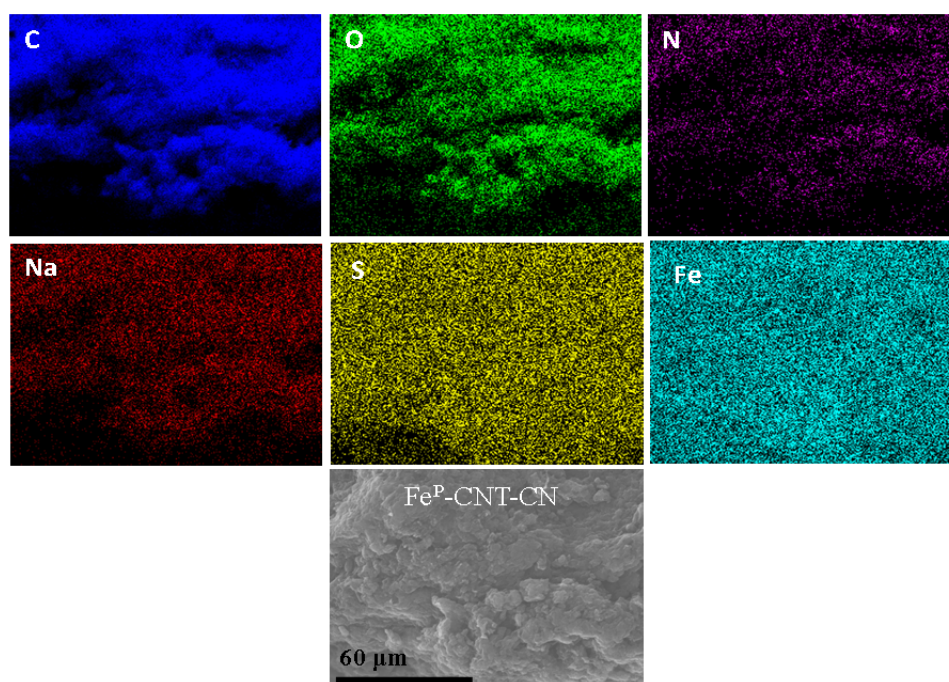
Figure S. 32: SEM-EDX mapping of Fe^P-CNT-CN

Figure S. 33: SEM-EDX mapping of Fe^P-CNT-O

Table S. 16: SEM-EDX mapping quantification of the elements of pristine promoted catalysts

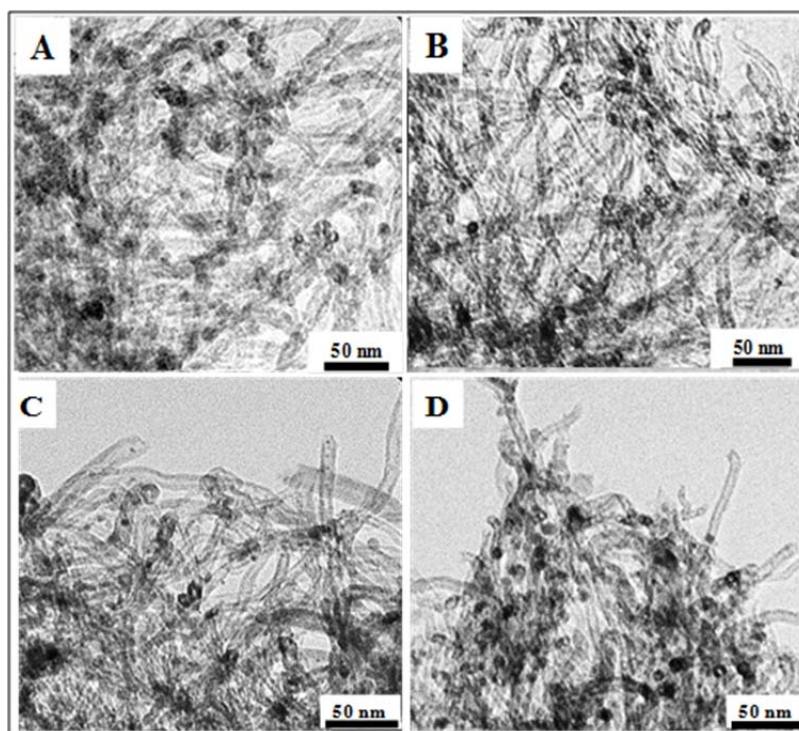| Pristine catalyst	SEM-EDX mapping C/O/Na/S/Fe (wt. %)
Fe^P-CNT-CN	85.5 / 9.5 / 0.14/ 0.3 / 4.1
Fe^P-CNT-H	86.7/ 9.6/ 0.23/ 0.2/ 2.6
Fe^P-CNT-NH_3	86.4/ 9.3/ 0.13/ 0.15 /3.7
Fe^P-CNT-O	78.2/ 12.8/ 0.2/ 0.2/ 6.1

Figure S. 34: TEM imaging of Fe-CNT-NH$_3$(A), Fe-CNT-CN(B), Fe-CNT-O (C), and Fe-CNT-H (D)
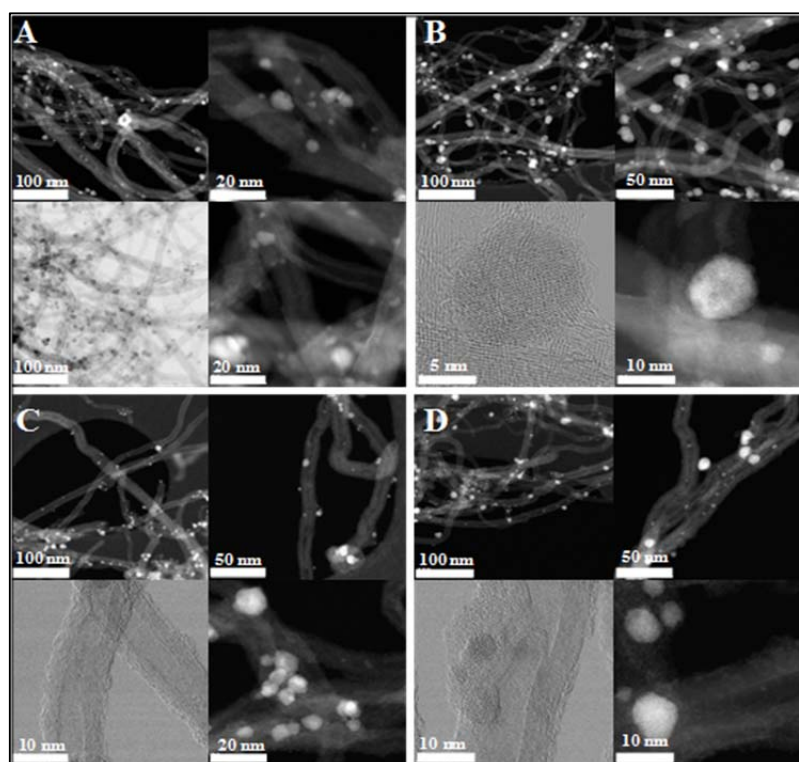

Figure S. 35: TEM images of Fe^P-CNT-NH$_3$ (A), Fe^P-CNT-O (B), Fe^P-CNT-CN (C), and Fe^P-CNT-H (D)
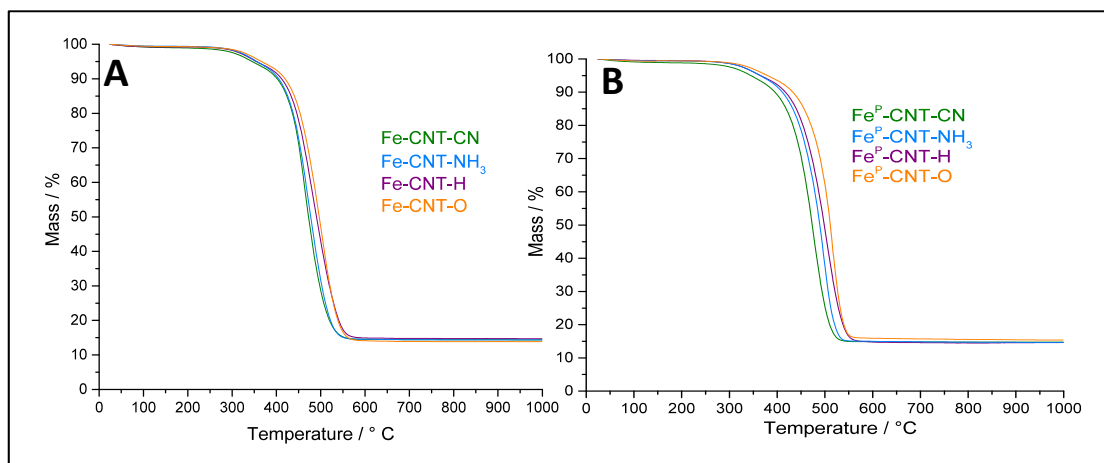
Figure S. 36: Thermogravimetric analysis for unpromoted catalysts (A) and promoted catalysts (B)
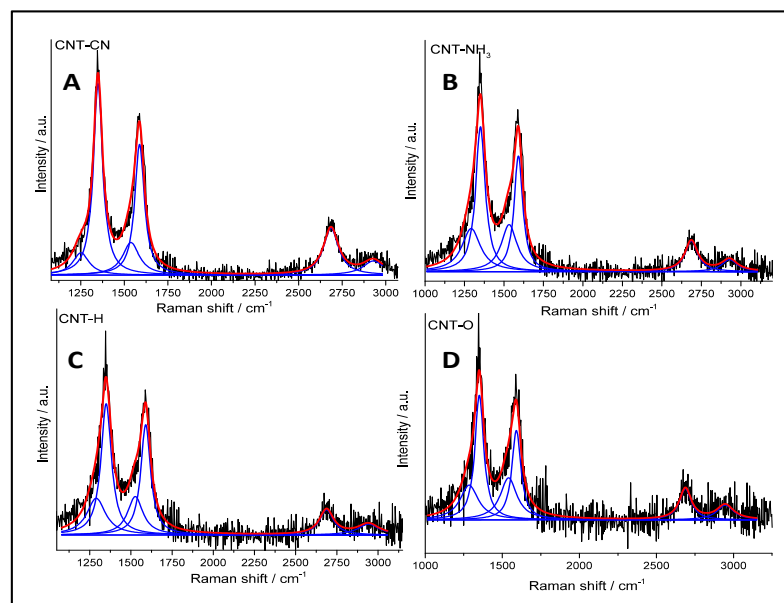

Figure S. 37: Deconvolution of Raman spectra for CNT-CN (A), CNT-NH₃ (B), CNT-H (C), CNT-O (D).
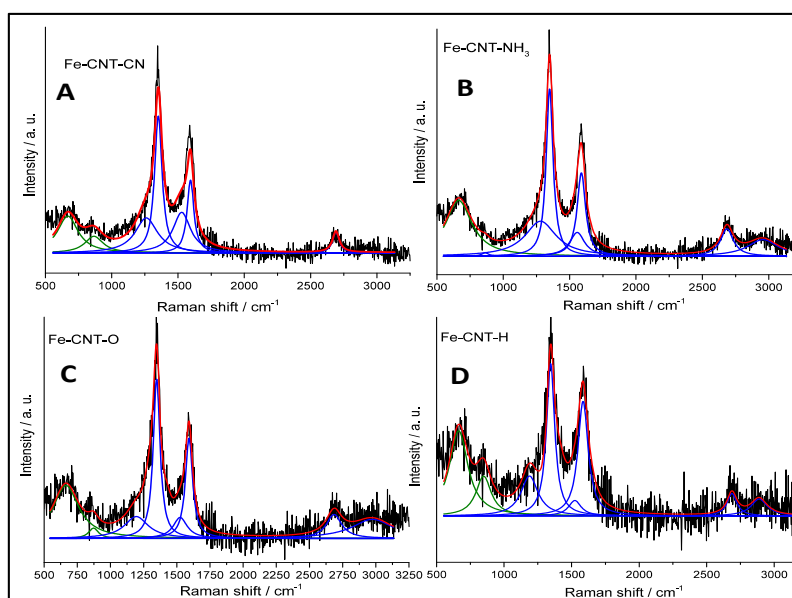
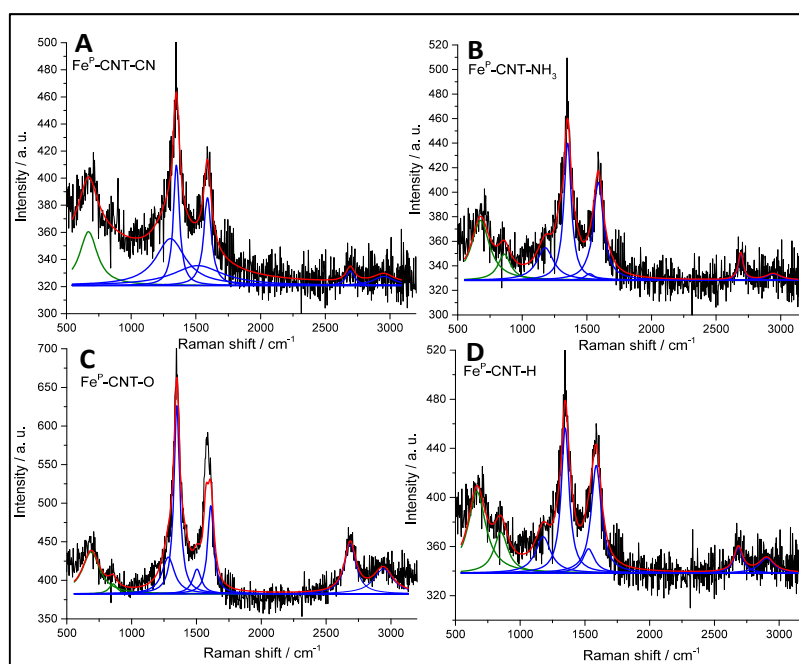*Figure S. 38: Deconvolution of Raman spectra for Fe-CNT-CN (A), Fe-CNT-NH$_3$ (B), Fe-CNT-O (C), Fe-CNT-H (D).*

Figure S. 39: Deconvolution of Raman spectra for Fe^P-CNT-CN (A), Fe^P-CNT-NH$_3$ (B), Fe^P-CNT-O (C), Fe^P-CNT-H (D).

Table S. 17: Intensity of D- and G- bands of Raman spectra for the supports and the catalysts, and the full width at half maxima (FWHM) of the D-band

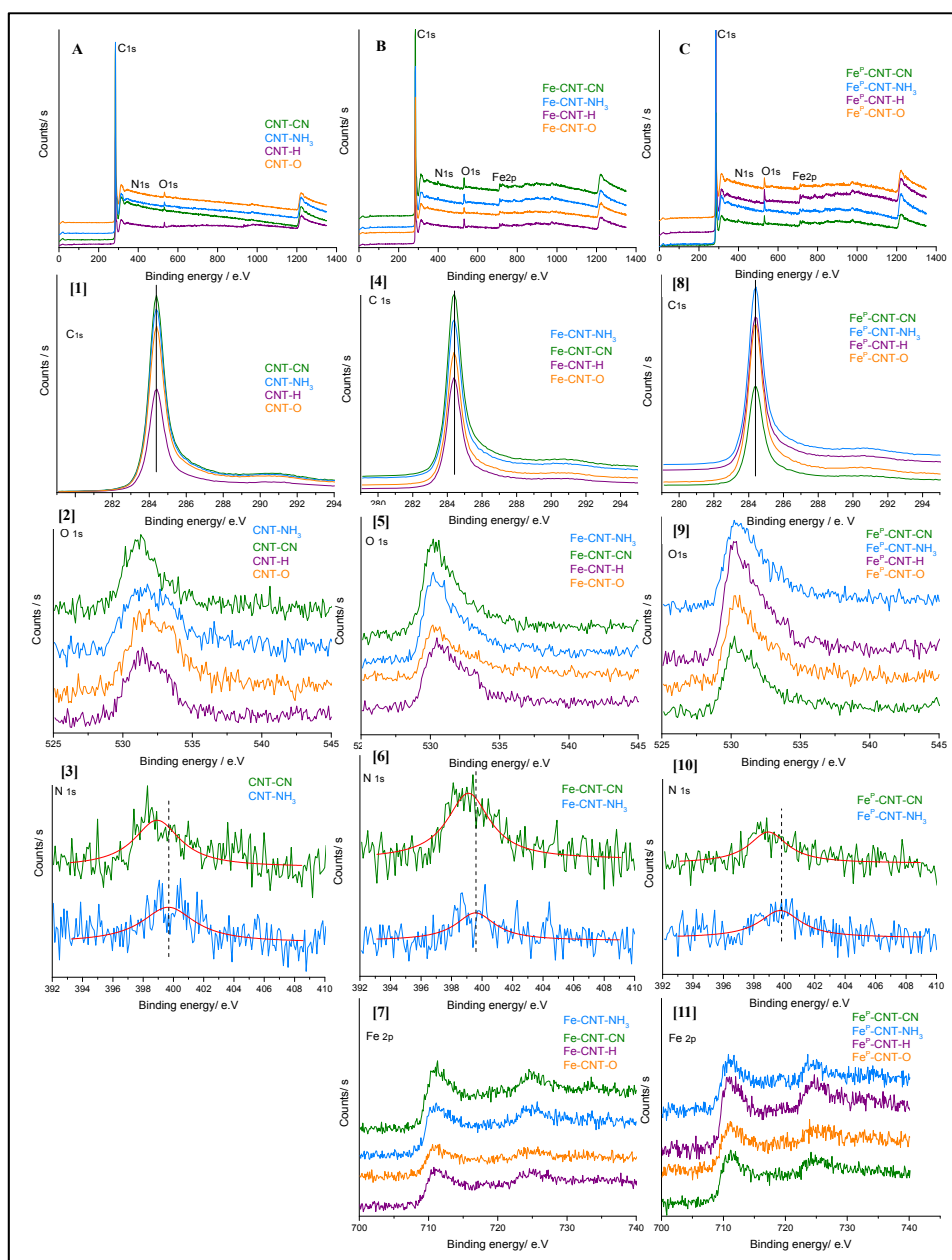| Supports / Catalysts	I_D/I_G	FWHM $_{D\ band}$
CNT-CN	1.2	72
CNT-NH$_3$	1.1	72
CNT-H	1.1	76
CNT-O	1.1	66
Fe-CNT-CN	1.2	76
Fe-CNT-NH$_3$	1.3	70
Fe-CNT-H	1.1	75
Fe-CNT-O	1.1	73
Fe^P-CNT-CN	1.1	68
Fe^P-CNT-NH$_3$	1.1	69
Fe^P-CNT-H	1.1	68
Fe^P-CNT-O	1.2	49

Figure S. 40: XP spectra of supports (A) and its C, O, and N components (1, 2, 3), of Fe-CNT-CN (B) and its C, O, N and Fe (4, 5, 6, 7), of Fe^P-CNT-CN (C) and its C, O, N and Fe (8, 9, 10, 11)

Table S. 18: Summary of the catalytic properties of promoted and unpromoted catalysts during an FTO process at 340°C, 10 bar, and $H_2/CO = 2$

Catalyst	Max. CO conversion (%)/ *TOS (h)*	Max. activity in FTY (10^{-5} mol $_{CO}$/g$_{Fe}$.s) / *TOS (h)*	Hydrocarbon product selectivity (%$_C$) (Measured according to the max. CO conversion)				
			CH$_4$	C$_2$-C$_4$ Olefins	C$_2$-C$_4$ Paraffins	C$_{5+}$	CO$_2$
Fe-CNT-O	49/*182*	47/*182*	34	30	23	13	37
Fe-CNT-H	36/*182*	35/*182*	37	32	18	13	37
Fe-CNT-NH$_3$	57/*182*	51/*182*	34	32	18	17	42
Fe-CNT-CN	77/*37*	85/*37*	32	22	27	18	40
Fe^p-CNT-O	73/*66*	69/*66*	22	30	24	24	41
Fe^p-CNT-H	92/*24*	84/*24*	16	34	20	30	42
Fe^p-CNT-NH$_3$	92/*27*	86/*27*	11	40	13	37	41
Fe^p-CNT-CN	92/*10*	94/*10*	8	47	6	39	41

C. Achievements

C. Achievements

a. List of Publications

[1] S. M. G. Lama, J. Pampel, T.-P. Fellinger, V. P. Beškoski, L. Slavković-Beškoski, M. Antonietti and V. Molinari. Efficiency of Ni Nanoparticles Supported on Hierarchical Porous Nitrogen-Doped Carbon for Hydrogenolysis of Kraft Lignin in Flow and Batch Systems, *ACS Sustainable Chem. Eng.*, **2017**, *5*, 2415-2420

[2] S. M. G. Lama, J. Schmidt, A. Malik, R. Walczak, D. V. Silva, A. Völkel, and M. Oschatz. Modification of salt-templated carbon surface chemistry for efficient oxidation of glucose with supported gold catalysts, *ChemCatChem,* **2018**

[3] S. M. G. Lama, J. Lennard Weber, J. Philipp Hofmann, R. Yan, K.P. de Jong, T. Heil, and M. Oschatz. Tandem Promotion Fischer-Tropsch to Olefins Catalysts by Sodium and Sulfur in Combination with Nitrogen-doped Carbon layers on Carbon Nanotube Supports, **2018** *(submitted)*

b. List of Conferences

List of Presentations

[1] 51. Jahrestreffen Deutscher Katalytiker Conference, **2018**, Weimar *(Accepted presentation)*
[2] Cat Catalytic Center, RWTH Aachen University, **2017**, Aachen *(invited presentation)*
[3] Jung Chemie Forschung–Ph.D Symposium, **2017**, Golm-Potsdam, Germany *(Accepted presentation)*
[4] 2nd Green and Sustainable Chemistry conference, **2017**, Berlin, Germany *(Invited presentation)*

List of Posters

[1] 1st Green and Sustainable Chemistry conference, **2016**, Berlin, Germany *(winning poster prize)*
[2] Max Planck Institute of Colloids and Interfaces Alumni meeting, **2016**, Golm–Potsdam, Germany *(Poster)*
[3] 253rd ACS National Meeting, **2017**, San Francisco-California, USA, *(Poster)*
[4] Max Planck Institute of Colloids and Interfaces Alumni meeting, **2017**, Golm–Potsdam, Germany *(Poster)*
[5] GDCh–Wissenschaftsforum Chemie Conference, **2017**, Berlin, Germany *(Poster)*
[6] Evonik Meets Academia symposium in Max Planck Institute of Colloids and Interfaces, **2017**, Golm-Potsdam, Germany *(Poster)*

D. Declaration of Authorship

Hiermit erkläre ich, dass die vorliegende Arbeit selbstständig angefertigt und keine anderen als die angegebenen Hilfsmittel und Quellen verwendet habe.

Hereby, I declare that the work reported within this thesis was produced independently, and nothing other than the referenced materials and sources was used.

Sandy M. G. Lama, Potsdam 25ᵗʰ April, 2018

Die vorliegende Dissertation entstand in der Zeit von Oktober 2015 bis März 2018 am Max-Planck-Institut für Kolloid- und Grenzflächenforschung in Potsdam-Golm unter der Betreuung von Prof. Dr. Markus Antonietti.

"I have not failed.

I have successfully discovered 10,000 things that won't work."

(Thomas Edison)

"This is not the end, but the key for a brighter beginning"